Studies on GaN Nanostructures grown by Molecular Beam Epitaxy and TiO₂ thin films grown by Atomic Layer Deposition.

A THESIS

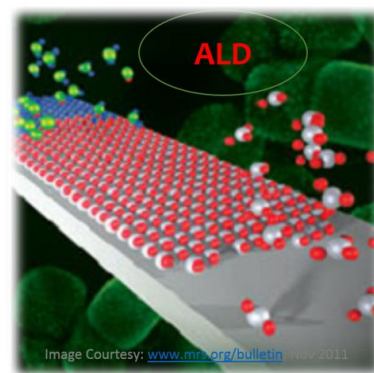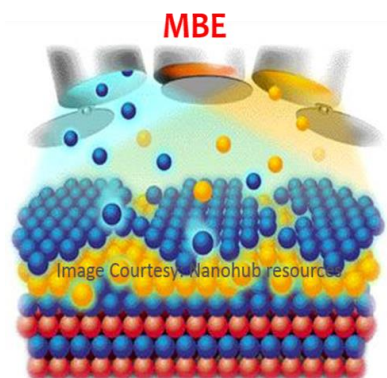*submitted in partial fulfilment for the degree of*

Master of Science

as part of the Int. Ph.D. programme

(Materials Science)

by

Shivakumar D.T.

Chemistry and Physics of Materials Unit

Jawaharlal Nehru Centre for Advanced Scientific Research

(*A Deemed University*)

Bengaluru, INDIA

April 2015

I do not know what I appear to the world; but to myself I seem to have been only like a boy playing on a seashore, and diverting myself in now and then finding a smoother pebble or a prettier shell than ordinary, whilst the great ocean of truth lay all undiscovered before me.

---Sir Isaac Newton---

Dedicated to almighty,

my parents,

and loving sister.

DECLARATION

I hereby declare that this thesis entitled **"Studies on GaN Nanostructures grown by MBE and TiO2 thin films grown by ALD"** is an authentic record of the research work carried out by me under the supervision of **Prof. S.M. Shivaprasad** at the Chemistry and Physics of Materials Unit, Jawaharlal Nehru Centre for Advanced Scientific Research, Bengaluru, India, and it has not been submitted anywhere for the award of any degree or diploma.

In keeping with the general practice of reporting scientific observations, due acknowledgements has been made whenever work described here has been based on the findings of other investigators. Any omission that might have occurred due to oversight or inadvertence in judgement is deeply regretted.

Date:

Place: Bengaluru, INDIA

Shivakumar D.T

(Int. Ph.D. Student)

CERTIFICATE

Certified that the thesis entitled **"Studies on GaN Nanostructures grown by MBE and TiO2 thin films grown by ALD"** has been carried out by **Shivakumar D.T** at the Chemistry and Physics of Materials Unit, Jawaharlal Nehru Centre for Advanced Scientific Research, Bengaluru, India under my supervision and that it has not been submitted elsewhere for the award of any degree or diploma.

Date:

Place: Bengaluru, INDIA

Prof. S.M. Shivaprasad

(Research Supervisor)

Professor S.M Shivaprasad
International Centre for Materials Science &
Chemistry and Physics of Materials Unit
Jawaharlal Nehru Centre for Advanced Scientific Research
Jakkur, Bengaluru- 560064, INDIA
Tel- +91-80-22082947 Fax- +91-80-22082766
URL: www.jncasr.ac.in/smsprasad

Preface

"Ten months ago I started these projects with two collaborations (accepting the challenge to place my legs simultaneously in two boats!!), with a hope to try and add a new dimension to our lab and it is now started yielding fruitful results just before the deadline of the thesis submission!!. This thesis is the report of the initial results out of my work and collaborations. It cannot express the long days spent in the lab, battling shoulder to shoulder (not literally!) with my fellow researchers and friends, the joy for the thin film deposition, the hope for good results and the sadness and tiredness with each failed attempt."

- - Shivakumar - -

Let me a bit professional;

From the 20th century onwards, nanomaterials have exceedingly become interesting topics of research due to their remarkable properties, which arise mainly due to their size. Nano porous (NP) semiconductors are interesting structures in that their mechanical, electrical, and optical properties can be modified significantly from their host materials. It should be noted that the material property can be tuned with porosity, periodicity, and height of the Nano pores, so they may be considered as a new material with variable material parameters. Moreover, their greatly increased surface area makes them promising for an electrode of electrochemical (EC) surface reaction and gas sensing.

The work presented in Part A of this thesis is about, the growth of high quality epitaxial GaN Nanostructures using plasma assisted molecular beam epitaxy (PA-MBE), and an attempt to exploit unique morphology and nanoscale properties of GaN Nanowall network towards efficient Water splitting *(done in collaboration with Prof Sampath, IPC, IISc)* and H_2 Gas sensing applications *(done in collaboration with Prof Navakantha Bhat, Cense, IISc)*. Part B of the thesis deals with the growth and characterization of TiO_2 ultra-thin films on different planes c, a, m, and r- of sapphire using recently installed state-of-the-art Atomic Layer Deposition (ALD).

Little things often harbour a great secret - the **physics of Nanoworld**.

Acknowledgements

I express my deep felt gratitude for my research supervisor **Prof. S.M. Shivaprasad** for his constant guidance, unstinted support, and timely suggestions throughout my M.S research tenure. I am grateful to him for supporting me in propelling my research project in the right direction. I am indebted to him for the acquired skills in several instrumental techniques during my research practice. I thank Mrs **Anupama Shivaprasad** and **Sharvani** for their kind words.

I feel fortunate to be in the JNCASR campus, and to listen to encouraging and inspiring words about research by the legend, **Prof. C.N.R Rao**. His presence and warmth itself is a motivation for performing scientific research. I am grateful to him for being my hero with boundless enthusiasm, spirit and activeness, up-to-date knowledge, and dynamic commitment to science.

I express my sincere thanks to **Prof. K.P Ramesh**, Physics Department, IISc for advising to choose research career and helping me in advancing in the right direction.

I am grateful to our chairman of CPMU, **Prof. S. Balasubramanian** and Int. Ph.D. co-ordinator **Prof. T.K. Maji** for their support at times of distress and extending their help to overcome initial challenges of research endeavour. I express my sincere thanks to **Prof. Aloknath chakrabarthy, Prof. G.U. Kulkarni, Prof. K.S Narayan, Prof. N. Chandrabhas, Dr. Sridhar Rajaram**, for the motivational words and useful discussions during course work and laboratory learning. I also thank all my course work teachers Prof. Shobhana Narasimhan, Prof. A.K. Sood, Prof. Arindam Ghosh, Prof. U.V. Waghmare, Prof. A. Sundaresan, Prof. M. Eswarmoorthy, Dr. Rajesh Ganapathy, Dr. Ranjan dutta, and faculty of NCU.

I would like to thank all the teachers who taught me till now, especially prof. Nanjundappa, whose discipline in practice of physics aroused an indomitable interest in me. I

--- Shivakumar ---

List of Contents

Part A

Part B

Synopsis

This thesis is a combination of two projects which were accomplished using two different advanced thin film deposition techniques, **Molecular Beam Epitaxy (MBE) and Atomic Layer Deposition (ALD**), followed by multi-technique characterization.

PART-A

In PART-A, we have presented the results on GaN nanostructures grown by using plasma-assisted molecular beam epitaxy as a function of Ga flux rate. We have also described some of the initial results on photo-electrochemical water splitting and hydrogen gas sensing characteristics of one of these GaN nanostructures.

Chapter A.1 introduces group-III nitrides with special focus on GaN, its crystal structures followed by issues of lattice mismatch and substrate compatibility in growing epitaxial GaN.

Chapter A.2 gives the description of experimental methods which include the deposition technique MBE and various *in-situ* and *ex-situ* complementary characterization techniques employed in this thesis.

Chapter A.3 presents the growth of GaN nanostructures on c-plane sapphire substrate by varying Ga flux and their characterization results compared with a commercial GaN epilayer.

Chapter A.4 presents the preliminary results of the application of GaN Nanowall network for photo-electrochemical water splitting and H_2 gas sensing.

PART-B

In the second part, PART-B we have presented the results on Titanium dioxide (TiO_2) thin films deposited on c, a, m, and r-plane sapphire substrates thermally, using recently installed state-of-the-art atomic layer deposition system.

Chapter B.1 introduces the interesting field of atomic layer deposition with its brief history, underlying basic concept and its application in microelectronics. It also gives the details about the chemical mechanism involved with an illustrative example. The measured and calibrated specifications and performance capabilities of the Beneq TFS-200 ALD system recently installed in our laboratory is also provided.

Chapter B.2 gives a detailed account, including a flowchart of the growth of TiO_2 using $TiCl_4$ and H_2O as precursors by ALD system in the thermal mode. The variations of morphological, structural and optical properties of TiO_2 films formed on c, a, m, and r,-plane sapphire are studied by employing suitable characterization techniques.

(*References to literature are given at the end of corresponding chapters*)

ACRONYMS

III-N	Group three Nitride
1D/2D/3D	One Dimension/ Two Dimension/ Three Dimension
LED	Light Emitting Diode
UHV	Ultra High Vacuum
PVD	Physical Vapour Deposition
MBE	Molecular Beam Epitaxy
PA-MBE	Plasma Assisted Molecular Beam Epitaxy
CVD	Chemical Vapour Deposition
MOCVD	Metal Organic Chemical Vapour Deposition
MOVPE	Metal Organic Vapour Phase Epitaxy
FM	Frank van-der Merwe (growth mode)
SK	Stranski-Krastonov (growth mode)
VW	Volmer- Weber (growth mode)
ELOG	Epitaxial Lateral Over layer Growth
PBN	Pyrolytic Boron Nitride
PL	Photoluminescence
PES	Photoelectron Spectroscopy
RHEED	Reflection High Energy Electron Diffraction
SEM	Scanning Electron Microscopy
FE-SEM	Field Emission Scanning Electron Microscopy
SEI	Secondary Electron imaging
BSE	Back Scattered Electrons
EDS	Energy Dispersive X-ray Spectroscopy
AFM	Atomic Force Microscopy
CL	Cathodoluminescence
RGA	Residual Gas Analyzer
SCCM	Square Cubic Centimetre

QCM	Quartz Crystal Microbalance
ESCA	Electron Spectroscopy for Chemical Analysis
XPS	X-ray Photoelectron Spectroscopy
HR-XRD	High Resolution X-ray Diffraction
P-XRD	Powder X-ray Diffraction
UV-Vis-NIR	Ultraviolet-Visible-Near Infrared
PEC	Photo-electrochemical
IDC	Interdigitated capacitor
IDE	Interdigitated Electrodes
ALD	Atomic Layer Deposition
PE-ALD	Plasma Enhanced Atomic Layer Deposition
GPC	Growth per cycle
FBR	Fluidized Bed Reactor

Part-A
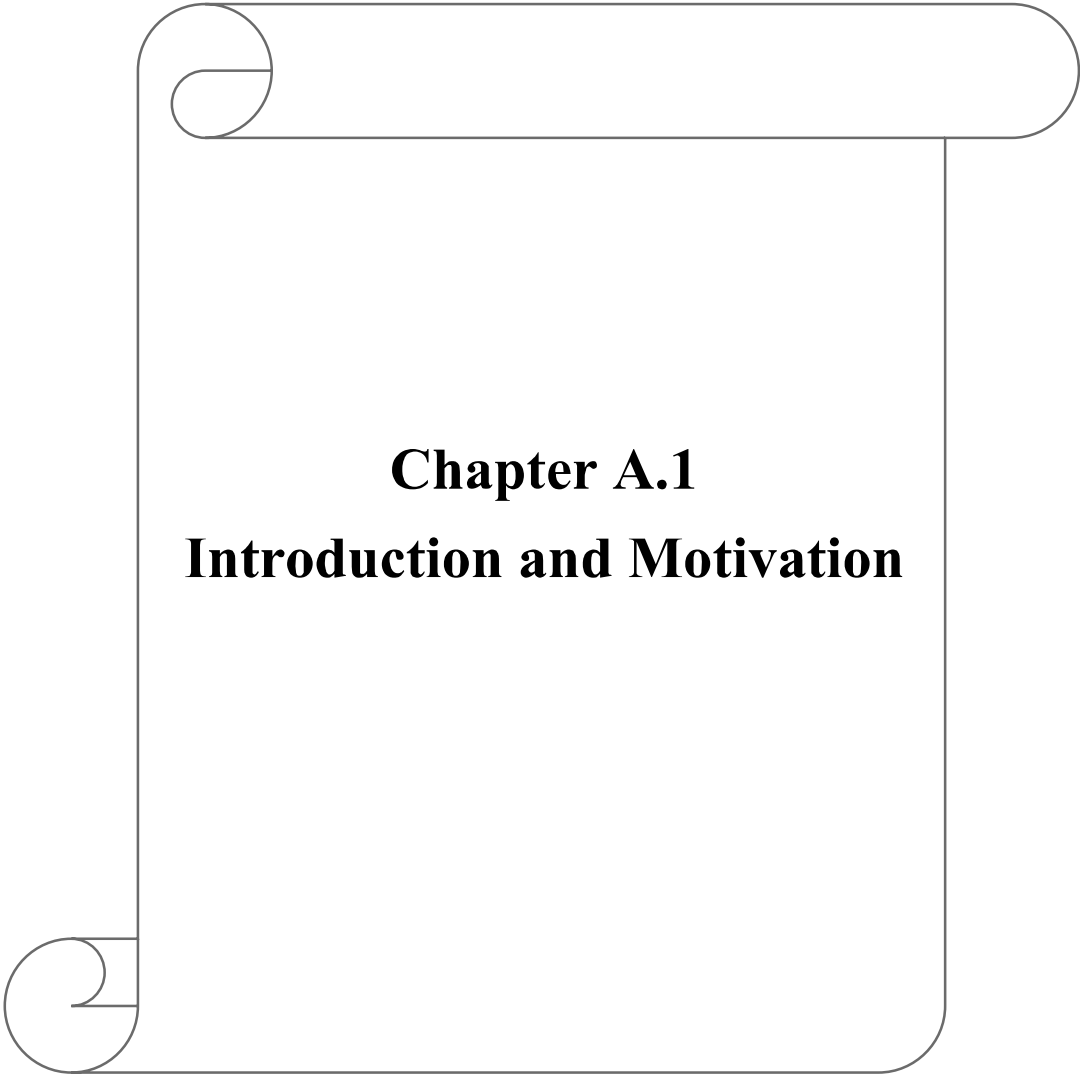
Growth of GaN Nanostructures on C-plane sapphire by Plasma-assisted Molecular Beam Epitaxy.

MBE
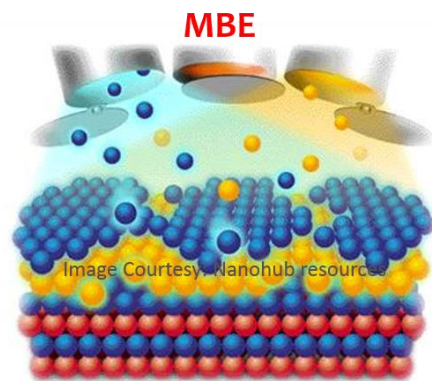
Glory, silicon carbide!
Schottky, switch, and polytype
Cree Research and A-T-T,
F-E-T and S-I-T!

Glory! Gallium nitride.
Nakamura and blue light.
Higher current, higher goal.
Thank you, Yoder, thank you all.

(A poem dedicated to the MRS Panel in the fall of 1998, which summarized SiC and GaN-based research in Japan.)

Chapter A.1
Introduction and Motivation

Chapter A.1
Introduction and Motivation

This chapter gives a detailed account of group III – nitride family, with special focus on Gallium Nitride (GaN) in terms of its fundamental properties and promising applications. Literature background that highlights the challenges in GaN research, limitation to their applications and how these challenges can be addressed through the nanostructure route is discussed. This chapter concludes by presenting the scope and organization of the thesis.

A.1.1 Group III-nitrides

(Al/Ga/In)-N compounds namely AlN, GaN and InN with respective bandgaps of 6.2, 3.4 and 0.6 eV constitute the group III nitride family. These wide-range bandgap materials possess several remarkable properties that make them particularly attractive for reliable solid state optoelectronic device applications. They have low dielectric constants with high thermal conductivity pathways, exhibit high bond strengths and high melting temperatures[1-3]. The large bond strengths inhibit dislocation motion and improve reliability in comparison to other II-VI and III-V materials[1]. In addition, group III-nitrides are resistant to chemical etching and hence should allow GaN-based devices to be reliably operated in harsh environments[4, 5]. With large avalanche breakdown fields, high thermal conductivities, and large high-field electron drift velocities[2, 4, 7-9], various high temperature and high-power microelectronic and optoelectronic devices such as passivation barriers, ohmic contacts in integrated circuits, blue light-emitting diodes, candela-class blue-light emitting diodes, green and yellow light-emitting diodes, UV photodetectors, reflector stacks, high electron mobility transistors, hetero-structure field effect transistor, metal semiconductor field-effect transistors, and surface acoustic wave devices have been fabricated. Stimulated emission has been reported from optically pumped GaN and AlGaInN alloy double hetero-structure films[2-4].

A.1.2 Crystal structure

Group III-nitrides are known to exist in two distinct crystalline polymorphs, namely Wurtzite (space group C46*v*-PC6mc) and Cubic Zinc Blende (space group T2d-F43m) polytypes[9]. For bulk III-Nitrides under ambient conditions, Wurtzite is the thermodynamically stable structure, while the cubic zinc blende phase is metastable and is observed only for hetero-epitaxial layers grown on {011} crystal planes of cubic substrates such as GaAs[13], Si[10], SiC[11] and MgO[12] due to topological compatibility. A third rock salt form for III-nitrides is also possible only under high pressure. Both Wurtzite and zinc blende structures have tetragonal coordination with each atom bonded to four other atoms of opposite species (**Fig.A.1.1**). The nature of the bonding is predominately covalent with some ionic character. Wurtzite structure is a member of the hexagonal close packed system with an ABAB layer structure, and Zinc Blende is cubic close-packed with an ABCABC layer structure. The nearest-neighbour positions are almost identical but the relative positions of the second nearest neighbour differ.
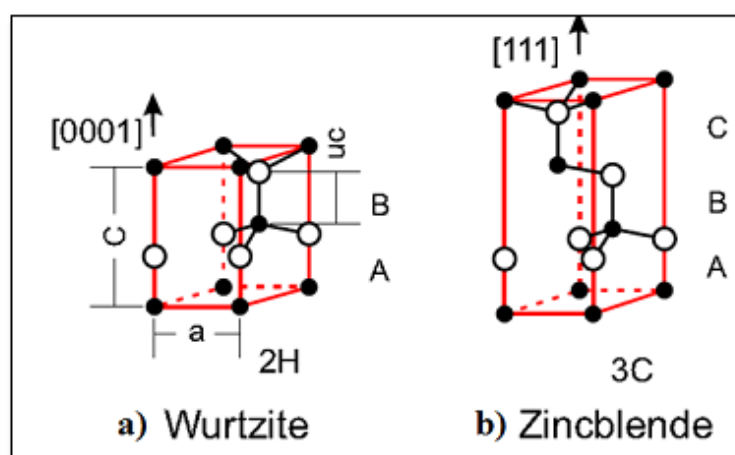
Fig. A.1.1 *Stick and ball stacking model of crystal with a) with Wurtzite structure along the [0001]direction b) Zinc Blende structure along the [111] direction.*

The major difference between the two structures is the stacking order of the tetrahedral atomic sheets along the (111) axis. For an ideal Wurtzite crystal structure c/a and u parameter values are 1.633 and 0.375 respectively, where u parameter is defined as the anion-cation bond length along c axis. Structure parameters for the group III nitride family are listed in **Table A.1.1**.

Material	Wurtzite (Å)				Zincblende (Å)
	a	c	c/a	u	a
AlN	3.111	4.979	1.601	0.382	4.360
GaN	3.189	5.185	1.627	0.377	4.500
InN	3.538	5.703	1.612	0.380	4.980

Table A.1.1: *Structure parameters of Wurtzite and zinc blende structures for group III-nitrides*[9, 10, 15-17].

A.1.3 Substrates and lattice mismatch

The properties of GaN films deposited on foreign substrates depend intricately on the inherent properties of the substrates such as constants of thermal expansion and lattice structure. Process-induced characteristics such as surface preparation and chemical and physical interactions at the surface are also critical. Hence, it is particularly important to employ high quality single crystalline substrates having lattice parameters close to that of group III-nitrides. For this reason, so far, best epitaxial nitrides has been grown on sapphire or SiC substrates[19]. In both cases, problems due to the lattice mismatch between the nitride epi-layer and the substrate (16% for sapphire and 3.5 % for SiC) have to be overcome. Sapphire is one of the most widely used substrate because of its relatively cheap and easy availability, wide bandgap, high thermal stability, and feasibility of *in-situ* and *ex-situ* cleaning. Moreover, it is insulating and transparent for most of the bandgaps of nitride alloys; thus it affords certain benefits in opto-electronic devices, for example, for back illumination and in LEDs. Sapphire also has similar crystal structure to that of Wurtzite group III-nitrides and since it is Al terminated on the surface, it can be easily nitrided to form a thin AlN layer[19].

The lattice mismatch between the substrate and the grown epi-layer is defined as,

$$\frac{a_{III-N} - a_{Sapphire}}{a_{Sapphire}}$$

where a, is the lattice parameter and subscripts represent the substrate and nitride.

There are two possible epitaxial orientations for the group III-nitrides grown on sapphire (0001) surface, which are shown in **Fig.A.1.2.**

$[11\underline{2}0]_{III-N} \parallel [11\underline{2}0]_{sap}$ $[10\underline{1}0]_{III-N} \parallel [11\underline{2}0]_{sap}$
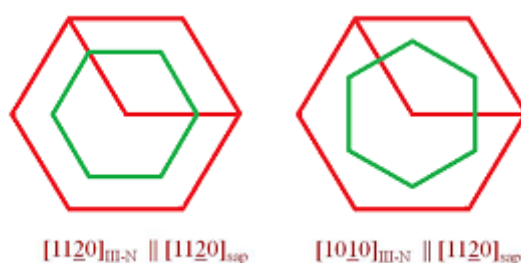
Fig A.1.2: Possible epitaxial relation between III-N and sapphire.

Table A.1.2 in the next page shows the lattice mismatch values in the two orientations for different nitrides with sapphire substrate.

Material	Lattice Mismatch	
	$[11\underline{2}0]_{III-N} \parallel [11\underline{2}0]_{sap}$	$[10\underline{1}0]_{III-N} \parallel [11\underline{2}0]_{sap}$
AlN	-34.6%	+13.3%
GaN	-33.0%	+16.0%
InN	-25.4%	+29.2%

Table A.1.2: Lattice mismatch for various members of III-V nitride family for two different epitaxial relations.

A.1.4 GaN: Band gap engineering

When Johnson et.al first synthesized GaN in 1932, its thermal stability and significant hardness initiated the interest in GaN research. Since then it is the excellent semiconducting features of GaN that have attracted the attention of researchers. Its wide band gap of 3.4 eV [20] allows for numerous applications in optoelectronic and high frequency devices. For example, GaN makes violet (405 nm) laser diodes possible, without use of nonlinear optical frequency-doubling. Its low sensitivity to ionizing radiation makes it a suitable material for solar cell arrays for satellites. The stability and ease of operation of GaN transistors at high voltages and high temperatures as compared to GaAs transistors have opened a wide window of applications in power amplifiers at microwave frequencies[1-3]. GaN can be doped relatively easily as compared to other members of the III-V nitride family to form n-type or p-type films.
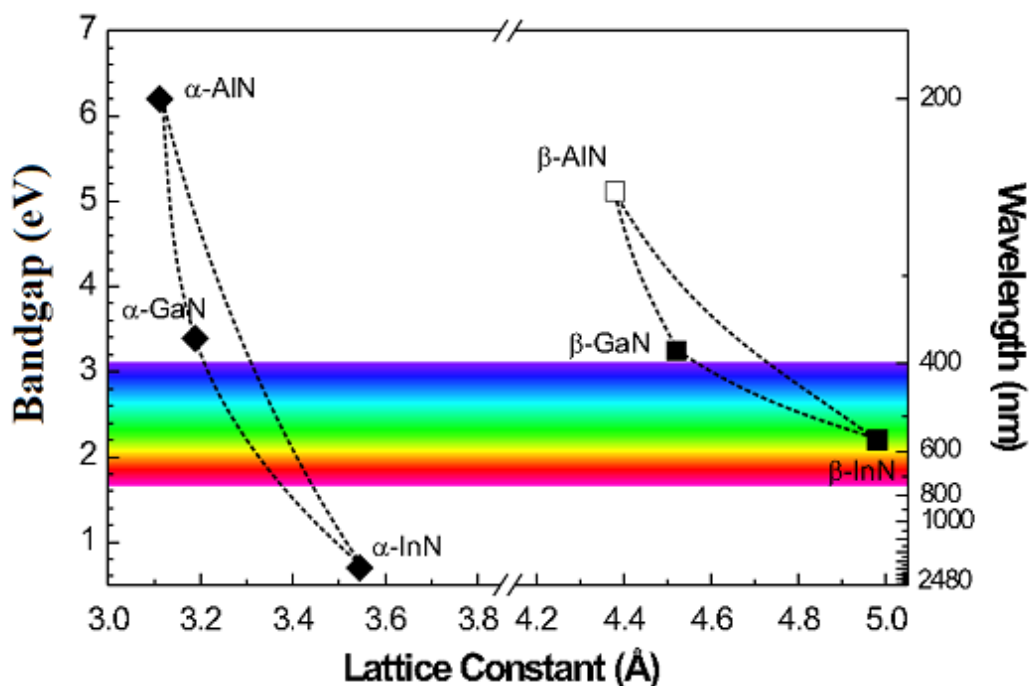
Fig.A.1.4*: Energy gaps and lattice constants for III-N semiconductors with wurtzite (α-phase) and Zinc blende (β-phase) structures.*

The wurtzite polytypes of gallium nitride (GaN), aluminium nitride (AlN), and indium nitride (InN) are excellent materials for bandgap engineering, because they form a continuous range of solid solutions and super lattices with direct room-temperature bandgaps ranging from

0.7 eV (InN)[21, 22] to 3.4 eV (GaN) to 6.2 eV (AlN)[21]. Therefore, as illustrated in Fig.A.1.4, if we alloy GaN with In or Al, depending on the concentration, the full solar spectrum ranging from red, well into the ultraviolet and beyond can be spanned. These direct bandgap materials are especially useful as it allows for high quantum efficiency light emitters and full spectrum solar cells to be fabricated with this family of group III-nitrides, by bandgap engineering.

A.1.5 Limitations and new approaches

Growth of epitaxial device quality group III nitride films with low defect densities and dopant concentrations has been hindered by a lack of suitable lattice matched substrates[19], large n-type background carrier concentrations in the deposited nitride films, and large equilibrium dissociation pressure of N_2 from the nitrides at typical growth temperatures. Regardless of the growth method employed, the major problem in growing group III-nitrides arises from the need to incorporate stoichiometric quantities of nitrogen into the film. Moreover, lack of structural compatibility with the most widely used substrate – sapphire and SiC results in high dislocation density ($\sim 10^{10}$/cm^2), which acts as quenchers for charge carriers and photons. A great deal of effort has been spent in trying to overcome the problems arising from lack of GaN substrates[19]. Some of the best device results have been achieved through the use of buffer layer, epitaxial over layer growth (ELOG) and lattice matching epitaxy. So far the focus has been on devices based on epitaxial flat films with low defect densities, which are extremely difficult to form[22-24].

Recent approach has been to form nanostructures of GaN on sapphire that are defect free due to their small sizes and can act as good transporters of electrical and optical carriers[25-27]. Recent developments in the direction to tailor-made nanostructures especially nanorods and nanowalls have shown promising results[28-30]. In this direction, our group has formed a high density ($\sim 10^8$/cm^2) of oriented GaN nanocolums and a hexagonal nanowall network on bare c-plane sapphire by control of growth parameters, without involving lithography, catalysts, buffer layers or nitridation[31, 32]. This study performed in nitrogen-rich conditions enables a unique mechanism of strain relaxation, forming a network of nanowalls that promotes super saturation conditions at open screw dislocations to initiate highly anisotropic one-dimensional (1D) growth. The mechanism suggests that this approach of sheer parametric control can enable tailor-making self-assembled anisotropic materials with desired properties[32].

A.1.6 Scope of Part A of this thesis

This Part A of the thesis is an attempt to grow high quality single crystalline, epitaxial GaN Nanostructured thin films on c-plane sapphire by plasma-assisted molecular beam epitaxy with different Ga flux and characterise the films for their morphological, structural, and optical characteristics. The large surface to volume ratio, which may enhance light absorption and the straddling band alignment of GaN Nanowall network motivated us to try its water splitting capability. The porous nature also motivated us to try and fabricate a resistive type H_2 gas sensor. The results shown in this thesis (Chapter A.4) are preliminary and we are working on improving the efficiency of GaN Nanostructured films for efficient H_2O splitting and H_2 gas sensing applications.

A.1.7 References

1) Handbook of Nitride Semiconductors and Devices, Hadis Morkoç Volume 1 -4, ISBN: 978-3-527-40838-2.

2) S. C. Jain1, M. Willander2, J. Narayan3, and R. Van Overstraeten, J. Appl. Phys. 87, 965 (2000).

3) S. Nakamura and G. Fasol. The Blue Laser Diode. Springer-Verlag, Berlin, 1997.

4) I. Akasaki and H. Amano. Japanese Journal of Applied Physics, 36:5393, 1997.

5) T. Mikai, M. Yamada and S. Nakamura. Japanese Journal of Applied Physics, 38:3976, 1999.

6) S.T. Strite and H. Morkoç, J. Vacuum Science and Technology B10 (1992) 1237

7) B. K. Ridley, J. Appl. Phys. 84(1998) 4020

8) U.V.Bhapkar and M. S. Shur, ibid. 82 (1997) 1649

9) Ambacher, O., Majewski, J., Miskys, C., Link, A., Hermann, M., Eickhoff, M., Stutzmann, M., Bernardini, F., Fiorentini, V., Tilak, V., Schaff, B. And Eastman, L.F. (2002) Pyroelectric properties of Al(In)GaN/GaN hetero and quantum well structures. Journal of Physics: Condensed Matter, 14, 3399–3434.

10) Patrick Rinke, M. Winkelnkemper, A. Qteish, D. Bimberg, J. Neugebauer, and M. Scheffler Physical review B 77, 075202 (2008).

11) Lei, T., Fanciulli, M., Molnar, R.J., Moustakas, T.D., Graham, R.J. and Scanlon, J. (1991) Applied Physics Letters, 59, 944.

12) Paisley, M.J., Sitar, Z., Posthill, J.B. and Davis, R.F. (1989) Journal of Vacuum Science & Technology, 7, 701.

13) Powell, R.C., Lee, N.E., Kim, Y.W. and Greene, J.E. (1993) Journal of Applied Physics, 73, 189.

14) Mizita, M., Fujieda, S.,Matsumoto, Y. And Kawamura, T. (1986) Japanese Journal of Applied Physics, 25, L945.

15) Leszczynski, M. (1999) Common crystal structure of the group III-nitrides, in Properties, Processing and Applications of Gallium Nitride and Related Semiconductors (eds J.H. Edgar, S. Strite, I. Akasaki, H. Amano and C.Wetzel), EMIS Data Review Series, No. 23, INSPEC, The Institution of Electrical Engineers, Stevenage, UK, pp. 3–5.
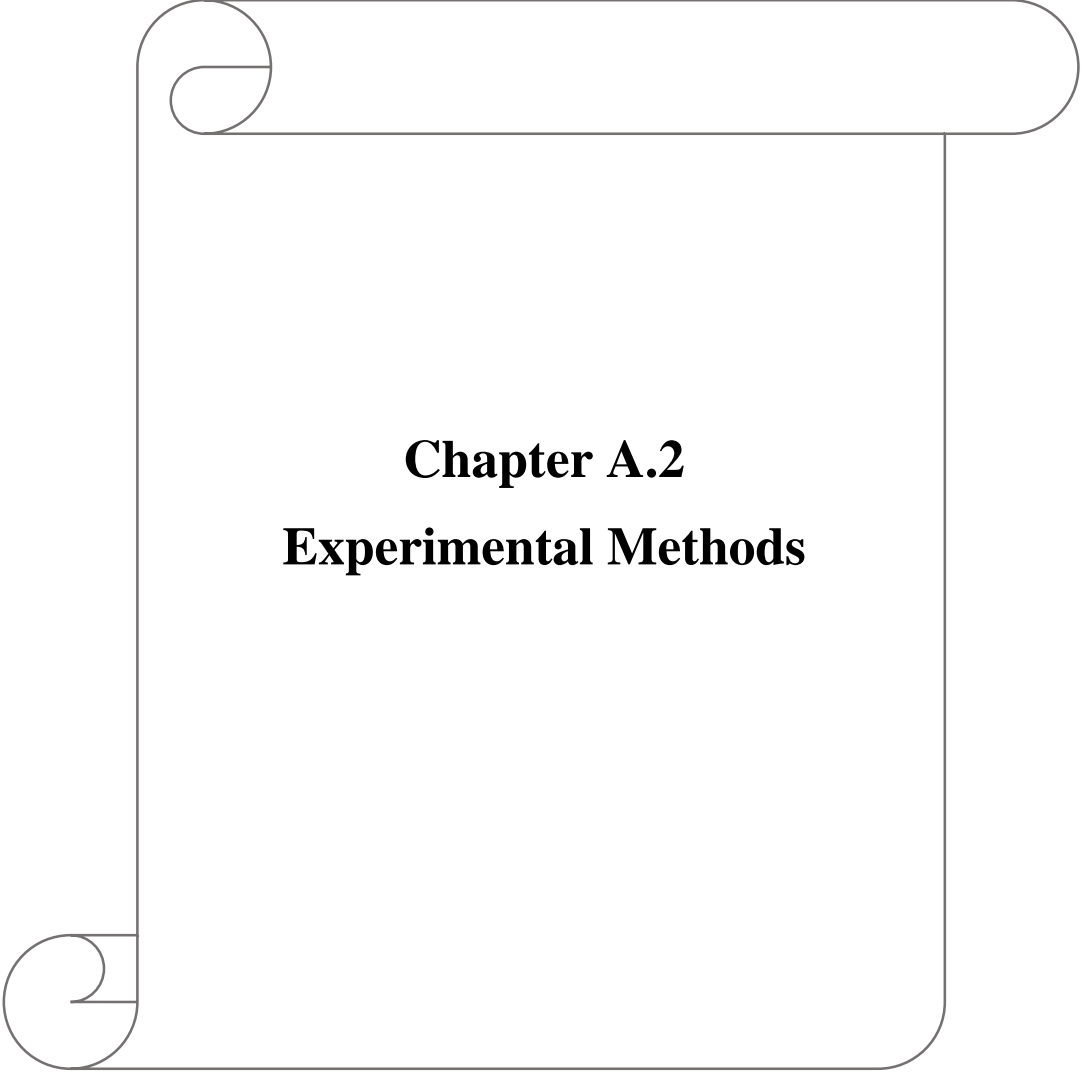
16)   Ambacher, O., Majewski, J., Miskys, C., Link, A., Hermann, M., Eickhoff, M., Stutzmann, M., Bernardini, F., Fiorentini, V., Tilak, V., Schaff, B. And Eastman, L.F. (2002) Pyroelectric properties of Al(In)GaN/GaN heteroand quantum well structures. Journal of Physics: Condensed Matter, 14, 3399–3434.

17)   Leszczynski, M., Suski, T., Perlin, P., Teisseyre, H., Grzegory, I., Bockowski, M., Jun, J., Porowski, S., Pakula, K., Baranowski, J.M., Foxon, C.T. and Cheng, T.S. (1996) Applied Physics Letters, 69, 73.

18)   Jeffery, G.A., Parry, G.S. and Mozzi, R.L. (1956) Journal of Chemical Physics, 25, 1024.

19)   L. Liu, J.H. Edgar , Volume 37, Issue 3, 30 April 2002, Pages 61 –127, Materials Science and Engineering: R: Reports

20)   B. Monemar, Phys. Rev. B 10, 676–681 (1974)

21)   Wu, J., Walukiewicz, W., Yu, K.M., Ager, J.W., III, Haller, E.E., Lu, H., chaff,W.J., Saito, Y. and Nanishi, Y. (2003) Applied Physics Letters, 80, 3967.

22)   Jithesh Kuyyalil, Malleswararao Tangi, and S. M. Shivaprasad, J. Appl. Phys. 109, 093513 (2011)

23)   P. Vennegues, B. Beaumont, and P. Gibart, Phys. Status Solidi 227, 1 (2001).

24)   P. Kumar, J. Kuyyalil, and S. M. Shivaprasad, Appl. Phys. Lett. 97,221913

(2010).

25)   R. Colby, Z. Liang, I. H. Wildeson, D. A. Ewoldt, T. D. Sands, R. E. Garcı`a, and E. A. Stach, Nano Lett. 10(5), 1568 (2010).

26)   M. Elison and W. Claude, J. Phys. D: Appl. Phys. 43, 354005 (2010).

27)   F. Qian, S. Gradecak, Y. Li, C. Y. Wen, and C. M. Lieber, Nano Lett. 5, 2287 (2005).

28)   L. Geelhaar, C. Cheze, W. M. Weber, R. Averbeck, H. Riechert, T. Kehagias, P.Komninou, G. P. Dimitrakopulos, and T. Karakostas, Appl. Phys. Lett. 91,093113 (2007).

29)   R. Songmuang, O. Landre, and B. Daudin, Appl. Phys. Lett. 91, 251902 (2007).

30)   E. Calleja, J. Ristic, S. Fernandez-Garrido, L. Cerutti, M. A. Sanchez- Garcia, J.Grandal, A. Trampert, U. Jahn, G. Sanchez, A. Griol, and B. Sanchez, Phys.Status Solidi B 244, 2816 (2007).

31)   Manoj Kesaria and S. M. Shivaprasad , Appl. Phys. Lett 99, 143105 (2011).

32)   Manoj Kesaria, Satish Shetty, and S. M. Shivaprasad, Cryst. Growth Des. 2011,11, 4900–4903.

Chapter A.2
Experimental Methods

Chapter A.2
Experimental Methods

This chapter describes the growth technique and various characterization techniques used in the present study. First we give a brief description of basic operation principles and fundamental concepts of Molecular Beam Epitaxy (MBE) growth technique, followed by *in-situ* characterization like reflection high energy electron diffraction, (RHEED) and other *ex-situ* characterization techniques such as Field Emission Scanning Electron Microscopy (FE-SEM), Atomic Force Microscopy (AFM), X-ray Diffraction (XRD), Photo-Luminescence (PL) and X-ray Photoelectron microscopy (XPS) employed in this work.

A.2.1 Molecular Beam Epitaxy:

Molecular beam epitaxy (MBE) is a term used to denote the epitaxial growth of compound semiconductor films by a process involving the reaction of one or more thermal molecular beams with a crystalline surface under ultra-high vacuum conditions. It was introduced in the late 1960s by J. R. Arthur and A. Y. Cho for growth of III/V-semiconductors. MBE is related to vacuum evaporation, but much improved control over the incident atomic or molecular fluxes so that sticking coefficient differences may be taken into account, and allows rapid changing of beam species[1]. Underlying growth mechanism in MBE is relatively simple: ultra-pure solid source that are to be grown are heated in a Knudsen cell (or effusion Cell) to produce beams of atoms and clusters. The base pressure of our system is about 5×10^{-11} Torr. This high order of vacuum provides a mean-free-path about 40 kms for the ambient gas molecules, and also a clean substrate surface for longer time to deposit the films. The precise control on the vacuum environment and the quality of the source materials allows the growth of high purity films by this technique as compared to other non-UHV techniques. To achieve such a high vacuum, a cryo, getter-ion and turbo molecular pumps are employed in attaining a base pressure of 5×10^{-11} Torr in the growth chamber. The chamber has a double walled cryo-panel which prevents degassing from the walls and also adsorbs the unwanted gas molecules that emanate by during the heating of substrate. A typical schematic of MBE growth chamber is shown in **Fig.A.2.1.**
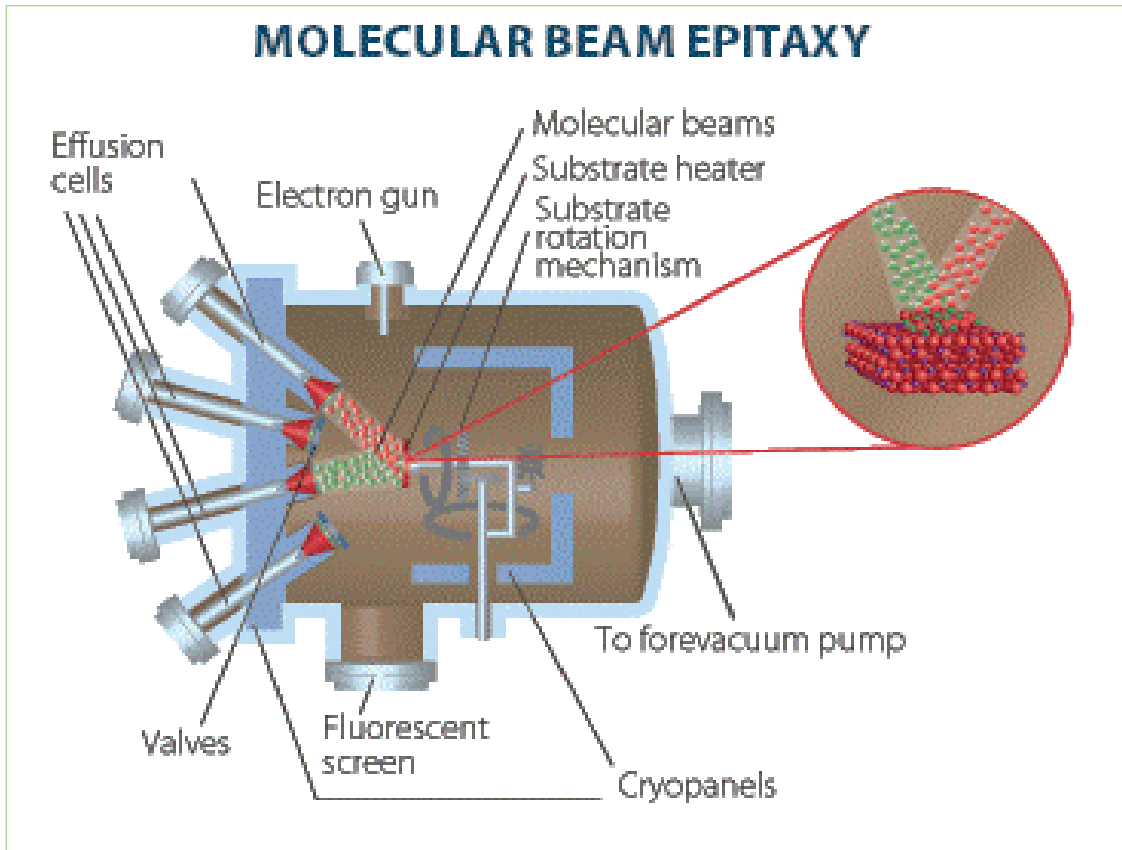
Fig.A.2.1: *Schematic diagram of Molecular Beam Epitaxy System[2].*

The high purity source materials and doping materials are loaded in the effusion cells which contain pyrolytic boron nitride (PBN) crucibles that are heated to high temperatures until the material sublimes or evaporates from effusion cell. Shutters mounted at the K-Cells mouth provide the direct control of the molecular beam (atoms or clusters) during the epitaxial growth. The nitrogen source to react with the metal atoms to yield nitride is nitrogen plasma, that is created by using a radio-frequency inductive coupled plasma source.

In the present work, we used Plasma Assisted Molecular Beam Epitaxy (PA-MBE) system (SVTA Assoc. Inc., USA). Our JNCASR MBE (shown in **Fig A.2.2**) system is configured for growth on 3'' wafer with high uniformity of <1% all round 2.8'' diameter of the wafer. The samples are loaded in the load-lock chamber and followed by initial preparation procedure carried out in the prep chamber by annealing the substrate (degassing) at 600°C for an hour. Our MBE system has 10 K-Cells in total with nitrogen plasma source as one of them. The growth manipulator has a circular heating filament and substrate temperature (T_s) were calibrated with respect to the pyrometer and thermocouple.

Nitrogen gas is introduced into chamber at a typical rate of 4.5sccm, while the growth was carried out at 2.5×10^{-5} Torr of nitrogen with $375W_f$ forward and $7W_r$ reflected power of the RF plasma maintained all along the growth. The purity of the nitrogen gas used is monitored by a quadruple mass spectrometer, which is also used for leak detection.

During growth, the deposition is monitored by *in-situ* reflection high energy electron diffraction (RHEED).

Fig A.2.2: *SVTA MBE System used in the present study for the growth of GaN films.*

A.2.2 Effusion Cells (Knudsen cells):

Effusion cells are one of the most crucial components of MBE systems. Effusion cells are used to generate ultrapure atomic or molecular beams from a large variety of elements and compounds. The charging materials placed in crucibles are made up of pyrolytic boron nitride (PBN). The crucibles are heated radiatively by electrically insulated heater filaments which are wounded in end-to-end fashion in our SVTA MBE system to prevent

magnetic interference, and the thermocouple is positioned in such a way that it has intimate contact with the crucible as shown in **Fig A.2.3.** For our growth, we have calibrated the Ga, flux by using a nude Ion gauge. The K-cell of Ga is designed with a hot lip (heater at the mouth of the K-cell to avoid deposition at these cold parts of the cell). The effusion cell temperature is controlled by Proportional Integrator Differentiator (PID) temperature controller and a heater power supply. Prior to loading the charge (7N purity ingots), the crucibles were outgassed at 1200°C to make sure that they are free from contamination. After loading the charge, the effusion cells were ramped up to the operating temperature at the rate of 200°C for 15mins. The growth element were deposited on the substrate with an the evaporation rate governed by formula (Knudsen effusion equation) at a given temperature is

$$d\Gamma_e = \frac{dN_e}{A_e dt} = P_{eq} \sqrt{\frac{N_A}{2\pi M K_B T}} [m^{-2} s^{-1}]$$

Where N_e the number of molecules evaporating from the surface area A_e, N_A, the Avogadro constant, T the temperature, P_{eq} the equilibrium evaporant pressure, k_B the Boltzmann constant and M is the molecular weight of the evaporant material.
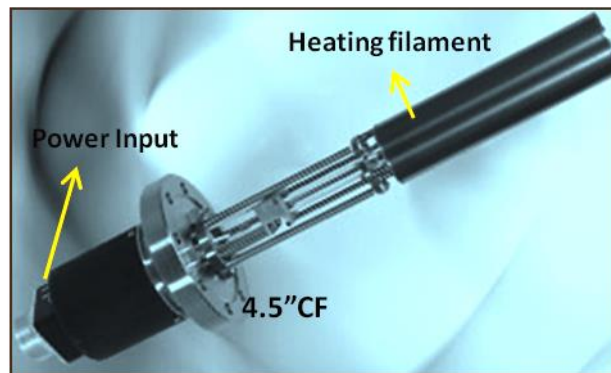
Fig A.2.3: *The snapshot of effusion cell of SVTA MBE system[3].*

A.2.3 Radio-Frequency nitrogen plasma source:

In a molecular beam epitaxy system, the charge materials are usually in the form of solid ingots. To nitride them, N_2 gas molecules or Ammonia are injected into the chamber in a form which is very reactive. In that context, there are different methods to produce active nitrogen species. Ammonia is an effective source of nitrogen, but the substrate temperature is

sufficiently high to break the ammonia molecules so limits parametric control of growth. Other way around is to have reactive nitrogen by exciting N_2 molecules by using radio frequency plasma source. There are different methods of plasma creation; one is electron cyclotron resonance plasma and the other is the radio frequency plasma source. As compared to ammonia based III-nitride growth, nitrogen plasma based films show good quality. In our study, we used SVTA nitrogen plasma source with a power supply operating at 13.5 MHz and consists of an inductively coupled plasma tube at the end of the source via a short coil. The forward power of $375W_f$ and reflection power of $7W_r$ is maintained during the growth. The image of the RF plasma ion source is shown in **Fig A.2.4 (a)**. The plasma alignments are done by using defection plates to have maximum intensity at the centre of the growth manipulator.

We used ultra-high pure nitrogen gas, and this gas is passed at a standard flow rate of 4.5sccm. A typical optical emission spectrum from the SVTA-4.5 plasma source is shown in **Fig A.2.4 (b)**. The coil of plasma source has built in water (16°C) circulation to reduce excess heating. Finally, the benefit of the plasma source is that its nitridation efficiency is independent of the substrate temperature, which allows for growth rates irrespective of substrate temperature.
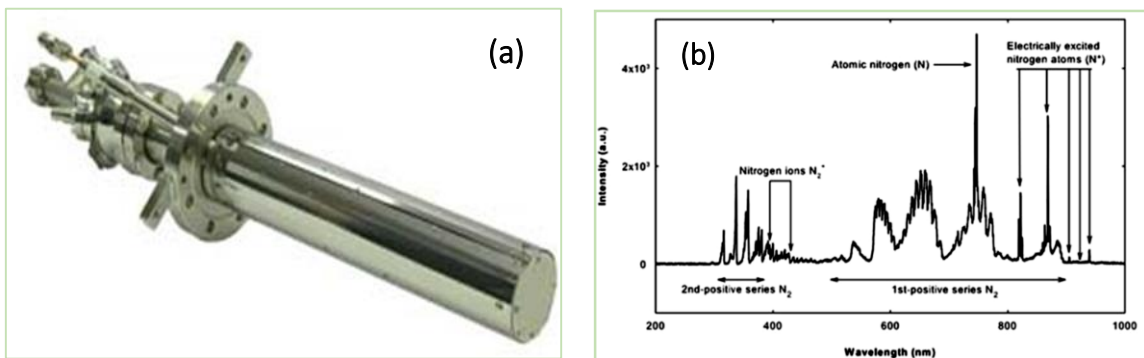
Fig A.2.4: *(a) The schematic geometry of plasma source set up in MBE system of SVTA make and (b) a typical optical emission spectrum taken at a nitrogen pressure of $1x10^{-5}$ Torr[3].*

A.2.4 Reflection High Energy Electron Diffraction (RHEED):

Our MBE system is equipped with *in-situ* RHEED to obtain information about growth modes. The technique involves grazing incidence (1-3°) of high energy electron beam of about 9kV in which the wavelength of the electron satisfies the diffraction condition. The grazing incidence on the sample surface restricts the penetration depth of electron making it

surface sensitive. Thus, the electron gets reflected from different crystal planes with depth of few nanometres of the film. The schematic and a typical image of the RHEED diffraction is as shown in **Fig A.2.5**.

The beams reflected from different atomic planes interfere constructively or destructively and form the diffraction pattern on the florescent screen. The diffraction pattern observed on the screen corresponds to the intersection of the reciprocal lattice of the sample with the Ewald sphere of radius $k = 2\pi/\lambda$ where k is the wave number and λ the wavelength[4]. As the name suggests, the spacing of the reciprocal lattice streaks is inversely proportional to the spacing between atomic planes taking part in diffraction. From this diffraction pattern (or RHEED pattern) spacing of the lines is used to determine the inter-planar spacing for different crystallographic orientations. By using RHEED intensity oscillations one can monitor film thicknesses. The typical RHEED patterns are the combination of reciprocal lattice streaks and Kikuchi lines.
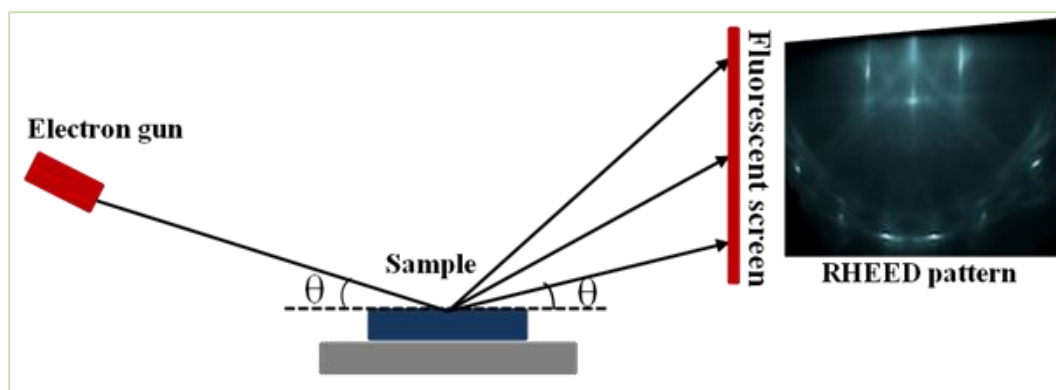

Fig A.2.5: *The schematic of the experimental set-up and a representative RHEED pattern.*

Fig. A.2.6 represents the RHEED evolution with respect to surface morphology[5]. Depending on the surface features the emerging RHEED pattern is made up of long, uniform streaks that mean lattice of rods perpendicular to the surface in real space and hence indicate the surface is growing smoothly, in a 2D fashion as the electrons are exhibiting true reflection diffraction. If however, the reciprocal lattice features are spotty, the surface is more 3D and rough on the nm scale, exhibiting transmission reflection diffraction as shown in **Fig A.2.6**. That means electrons are transmitted through surface features and cause interference pattern in spotty reciprocal features. If the diffraction pattern appears ring-like it is an indication that the film is

polycrystalline. Finally from the RHEED pattern, it is possible to calculate the crystal lattice constant. Indeed, the distance between the streaks provides the lattice parameter in the surface plane. In case of spotty pattern the distance in horizontal and vertical direction between the spots give a-and c-parameter[6]. One can have clear information about surface reconstructions along with the growth modes and crystallinity.
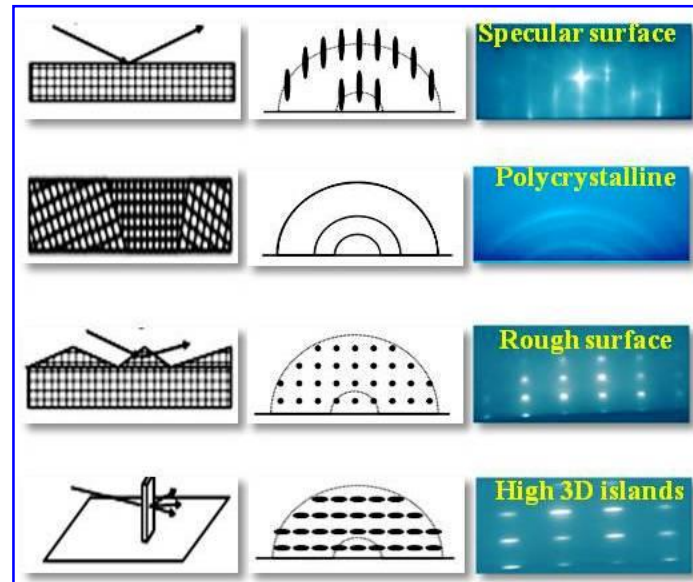

Fig A.2.6: *The representative pattern of RHEED evolution with respect to surface morphology.*

A.2.5 Scanning Electron Microscope:

The scanning electron microscopy (SEM) is used to observe the topography and morphology of the GaN Epilayer and nanostructure surface with high resolution. The typical SEM system as shown in **Fig. A.2.7** consists of an electron gun which is the source of electrons, and the condenser lenses which regulate the intensity of electron beam and direct it onto the specimen. The basic principle behind SEM is scanning of a finely focussed electron beam of 5-30 kV energy over the surface of the specimen. The scanning is carried out point by point in a time sequence with a high energy beam of electrons in a raster scan pattern. When electron interacts with specimen most important emission phenomena observed are (I) Secondary electrons, (II) Back-scattered electrons (BSEs) and (III) X-ray from the specimen, that are widely utilized for imaging and compositional analysis. The emission of secondary electrons from sample at each point on the specimen surface is strongly dependent on its shape[7].

Generally secondary electrons are collected at low angles from the surface of the sample and are utilized for better resolution of imaging rough surfaces of the specimen. The imaging is done in this process by scanning the electron beam across a sample and collecting the secondary electron signal from the beam-sample interaction.
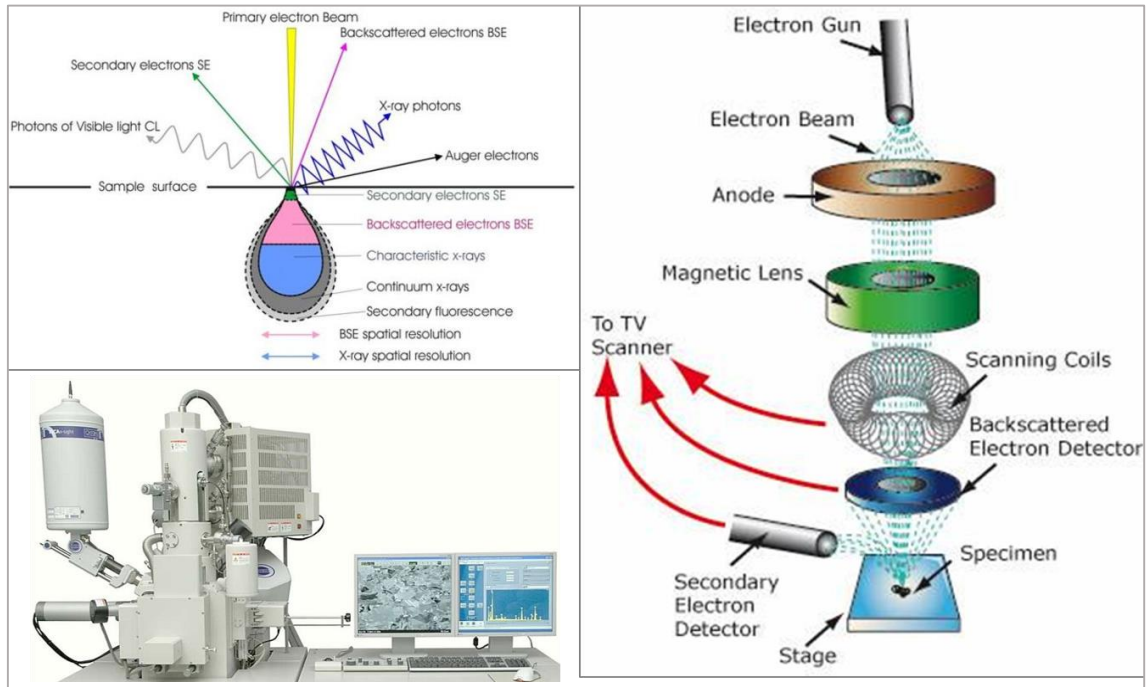
Fig A.2.7: *A typical SEM system and schematic of different type of electron emission upon impinging of primary electron beam.*

On the other hand, BSEs are scattered electrons that emerge from greater depths in the sample and their number density i strongly dependent on atomic number of the specimen, thus providing information about the distribution of different elements and atomic number contrast within the image.

The characteristic X-rays are emitted when the electron beam removes an inner shell electron from the sample which is used to identify the atomic composition, and measure the abundance of elements in the sample by Energy Dispersive Spectroscopy (EDS).

In our case, imaging of our samples were done in standard secondary electron imaging (SEI) mode, used to produce two dimensional topographical imaging of specimen using a Field Emission electron gun.

A.2.6 Atomic Force Microscopy

The atomic force microscopy was invented in 1986 by Binning, Quate and Gerber. This Microscopy is one of the first techniques capable of measuring distances in fractions of a nanometre. The AFM for the first time made it possible to image with such a high precision all types of surfaces including insulating samples.

Fig A.2.8: Principle of AFM- *laser beam is reflected from the back of the cantilever and is detected by a photodetector. The tip is extremely sharp with a single atom at the tip end.*
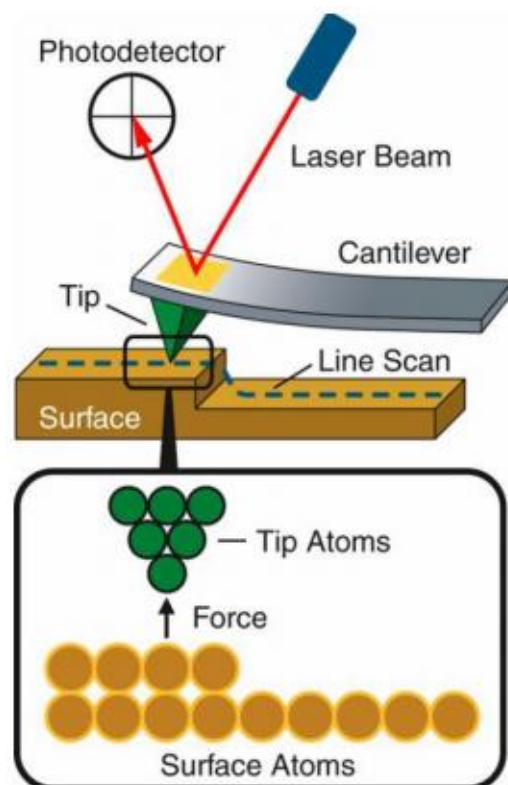
The AFM consists of a cantilever wherein a small tip is attached to a strip. The tip which regulates the precision of the AFM is a SiN/Si_3N_4 or Si tip micro-fabricated to have a radius of curvature of the order of a few nanometres or less. The Tip-Sample interaction causes the bending of the cantilever which is governed by the Hooke's Law. This displacement of the tip is typically measured by the change in the reflection spot of a laser incident on the cantilever. The movement of the reflection spot with the bending cantilever is monitored by a Differential Photo-diode detector array.

Optical interferometry, Piezo-response and capacitive sensing are other alternatives to monitor the cantilever bend. There is a continuous feedback system where the deflection of the cantilever modulates the scanning parameters of the cantilever. The type of feedback is dependent on the mode the AFM is being operated in. The AFM is employed in many imaging modes- typically the Contact mode, Non-Contact mode and the Tapping Mode.
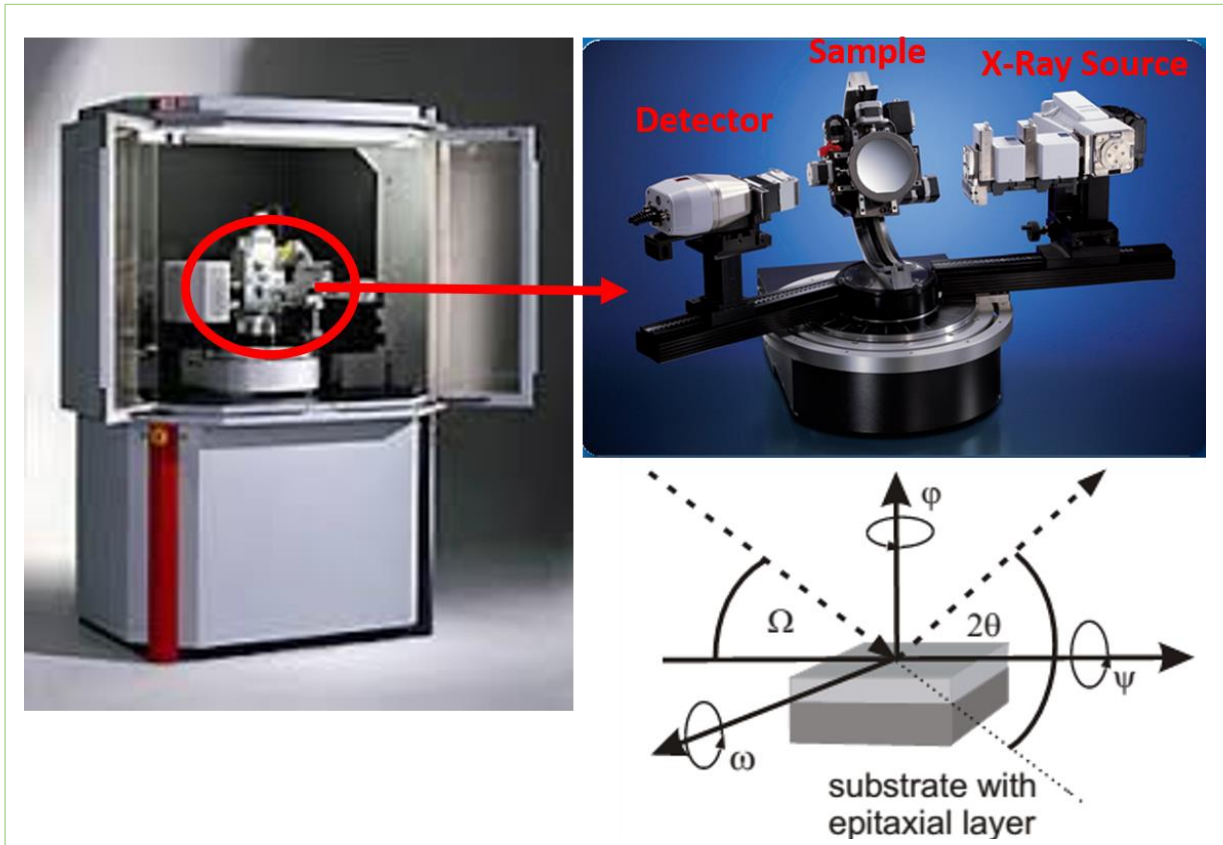
A.2.7 X-ray Diffraction:

X-ray diffraction is a powerful, non-contact method used to understand the crystalline phases in bulk materials, thin films and powder samples. In this process X-rays of wavelength 0.5~2.5 Å, which is close to the spacing of atoms in crystals, penetrate the sample and produce diffraction pattern due to scattering from the electrons clouds of atoms. The diffraction patterns have different peaks that corresponds to the x-rays scattered coherently by the inter-atomic planes and peak intensity depends on atomic density in the planes. The X-rays scattering off of neighbouring parallel planes of atoms either interfere destructively or constructively at a certain angle of incidence. If the waves interfere constructively it leads to large intensity signal at that angle. The constructive interferences occur when the planes satisfy the Bragg condition written as: *2dsinθ=nλ,* Where *n* is an integer, λ is the wavelength of the X-ray, *d* is the lattice spacing, and θ is the Bragg angle[8].

The most important and simple scan is *2θ- ω* scan for both symmetric and asymmetric reflection which gives c-and a-lattice parameter. Rocking curve (ω-scan) is used to analyse dislocation density and twist tilt mosaicity in the epitaxial layers. In this geometry, the detector is kept at a fixed angle with respect to the primary beam (*2θ*) while the sample is rocked around the plane of interest as shown in **Fig. A.2.9**[9].

The phi (φ) scan (sample rotation around φ- axis with constant ω and 2θ), gives the information about epitaxial relation between film and substrate. In case of III-nitride semiconductors, XRD is mainly used to evaluate the quality of the film including threading dislocation density determination. The mole fraction of alloys, and investigate the thickness and fine structure of materials with super-lattice structures. The line width of a rocking curve that is the full width at half maximum (FWHM), determines the crystalline quality and the determination of layer parameters such as alloy composition, uniformity of epitaxial layers, thickness, built-in strain and strain relaxation, and crystalline perfection related to the dislocation density possible. The FWHM broadening is due to the presence of defects such as

dislocations or stacking faults thus the good indicator of the crystalline quality of the materials. **Fig.A.2.9** show the photograph and schematic diagram of the Bruker-D8 DISCOVER X-ray diffractometer with high accuracy goniometer with 0.0001° step resolution for the sample which we have used in our study.

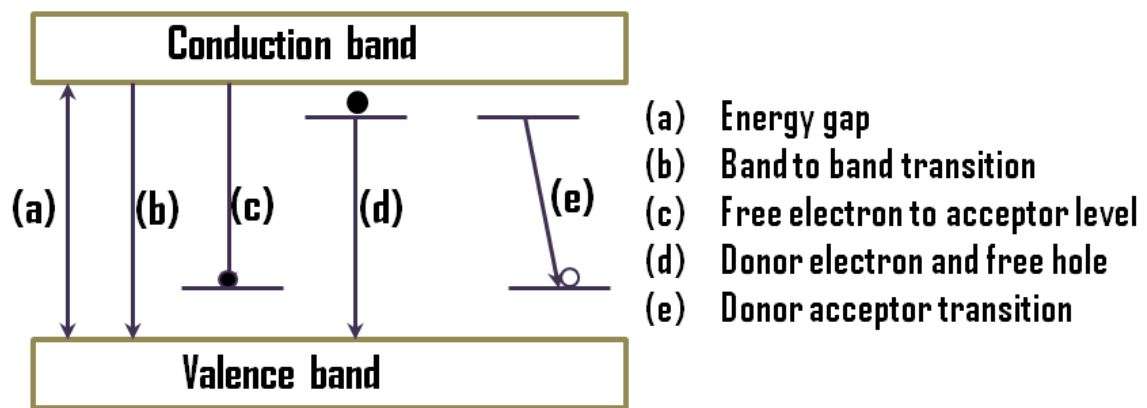**Fig. A.2.9:** *The schematic of axis of rotations in HR-XRD and Bruker-D8 Discover high resolution X-ray diffractometer*[9, 10]*.*

A.2.8 Photoluminescence

Photoluminescence spectroscopy is a non-contact, non-destructive method that provides information regarding electronic band gap and the impurity and defect levels in the electronic structure. Photoluminescence is a process in which a substance absorbs electromagnetic radiation and then re-radiates photons of corresponding energy. Quantum mechanically, described as an excitation to a higher energy electronic state and then it relaxes and returns to a lower energy level accompanied by the emission of a photon. The time domain between absorption and emission process is extremely short, in the order of tens of nanoseconds often called *life time*. If the incident light photon energy is higher than the bandgap of the

semiconductor then the valence electrons move into the conduction band, generating electron-hole pairs.

After certain time, the electron then relaxes to the bottom of the conduction band and electron hole pairs will recombine, often through a radiative transition. The intensity and the spectral contents of the PL is the direct measure of various material properties. The observed recombination pathways provide important information about the sample quality, band gap and band structure, donor and acceptor levels, defect types, impurities, crystalline quality, and defect densities.


Conduction band

(a) (b) (c) (d) (e)

(a) Energy gap
(b) Band to band transition
(c) Free electron to acceptor level
(d) Donor electron and free hole
(e) Donor acceptor transition

Valence band

Fig A.2.10*: The schematic representative electron transition at different energy state.*

In case of most semiconductors there will be optimum magnitude of concentrations of impurities and structural defects. These imperfections cause an improper periodicity of a lattice potential and form trap centres and localization energy states at the band gap. The energy of localized state depends on the nature of the defect. At low temperatures, most of the excitons are trapped due to low thermal energy and they are bound at defect state. As thermal energy rises gradually, the bound exciton gets released to form free exciton. In the case of doped material these defects create new states at the forbidden gap as shown in **Fig. A.2.10** (*d-transition*). In the present study, we used Horiba PL system with mercury lamp and He– Cd laser of 325 nm excitation wavelength with a maximum input power of 30mW and by using optical grating to generate the required excitation wavelength.

A.2.9 X-ray Photo-electron Spectroscopy

X-ray Photoelectron Spectroscopy (XPS), also known as ESCA (*Electron Spectroscopy for Chemical Analysis*) is one of the most widely used surface analysis techniques due to its relative simplicity in use and data interpretation. Developed in mid 1960s by *K. Siegbahn* and his research group, the basic working principle of XPS is the photoelectric effect outlined by *Einstein* in 1905. For XPS, the common photon energies are the ones emitted by Al K_α (1486.6 eV) and Mg K_α (1253.6 eV). Ti K_α (2040 eV) is another X-ray line which is sometimes chosen. The reason why XPS is highly surface sensitive is because the photoelectrons which are excited from the solid are of very short range. The binding energy of these peaks are the characteristic of the element. The composition of the material's surface can then be obtained by calculating the area of the peaks with appropriate sensitivity factors. The shape and the binding energy associated with each peak can be slightly altered by the chemical state of the emitting atom, which helps in finding the chemical bonding information.

Apart from detecting X-rays, the Auger electrons can also be detected, which is an additional advantage of XPS.
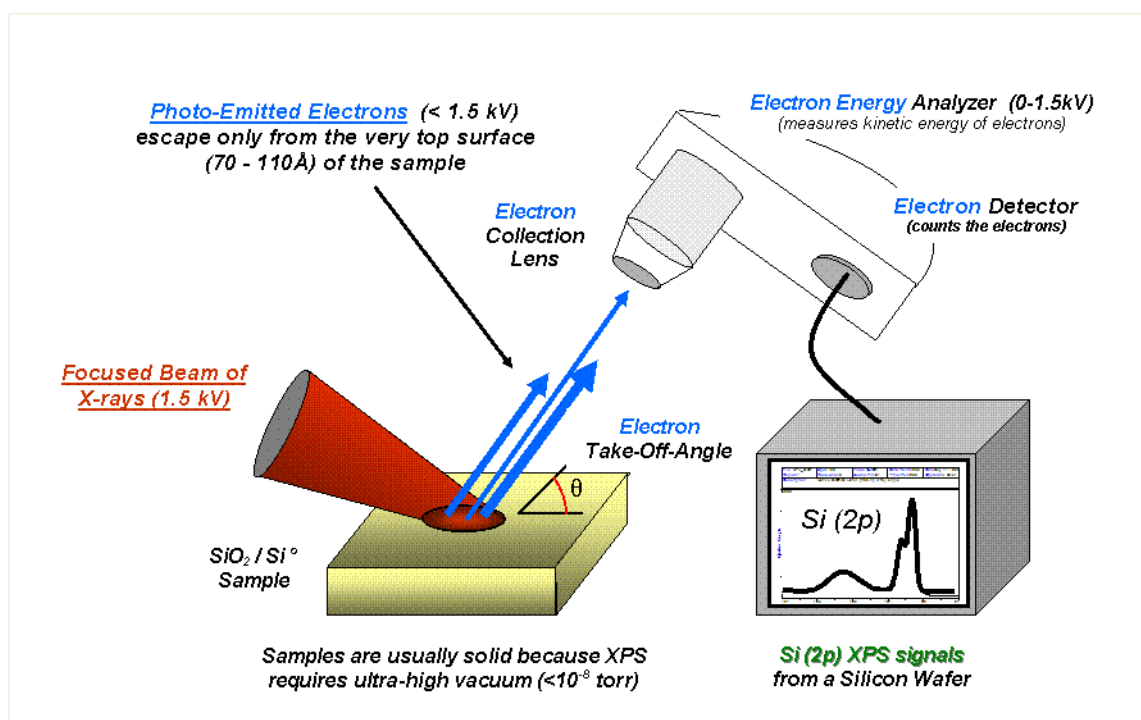
Fig A.2.11: *The schematic working principle of X-ray Photo-electron Spectroscopy.*

Fig A.2.11.1: *XPS Instrument used in the present study from Omicron, Germany.*

A.2.10 Raman Spectroscopy:

The Raman Effect was first observed in 1928 by Sir. C.V. Raman and the effect named him[11]. When light is illuminated on materials, the majority of the light is elastically scattered from materials, is called Rayleigh scattering. Here scattered light has the same wavelength as the incident light source. But Raman scattering is an inelastic scattering process of electromagnetic radiation by matter. Raman Spectroscopy with many advantages such as versatility, convenience, nondestructive nature and being a non-contact technique requiring no sample preparation, is very widely used as a characterization tool, also in the field of semiconductors. Raman spectroscopy probes the energy shift of in-elastically scattered light corresponding to a specific resonant frequency of quantized lattice vibrations providing the information of the material under analysis, such as electronic and magnetic properties. Thus, the light interaction with the solid gives rise to a scattering radiation both in higher and lower frequencies of spectral distribution.

The higher frequency line observed is called as anti-stokes and the lower frequency line is called as stokes line. Furthermore, in our study, we have used a visible laser for excitation and obtain a laser resolution of ~1μm which is determined by the beam waist of the probe laser at the sample surface. In case of III-nitride semiconductors, Raman Spectroscopy is extensively used to measure alloy composition, Ga and N vacancy and strain in the material.

The representative Raman spectrum of GaN is shown in **Fig A.2.12**, the marked E_2 high mode shift is a characteristic of residual strain in the film.
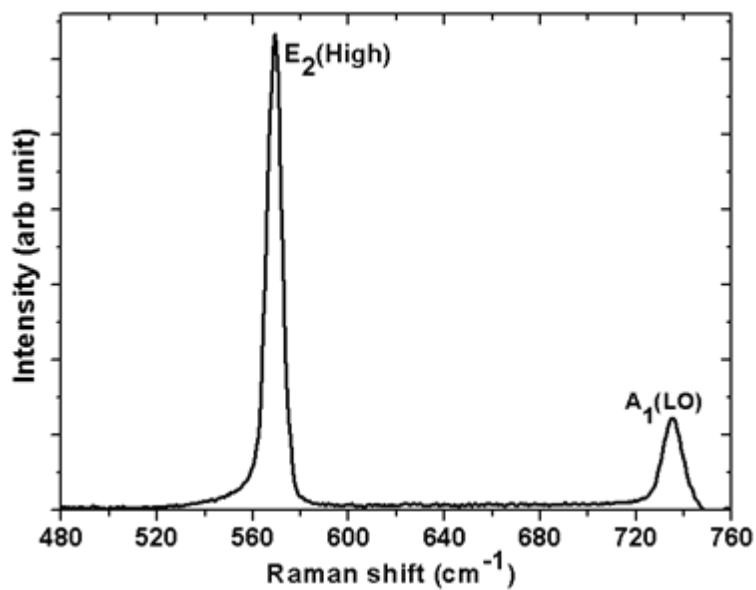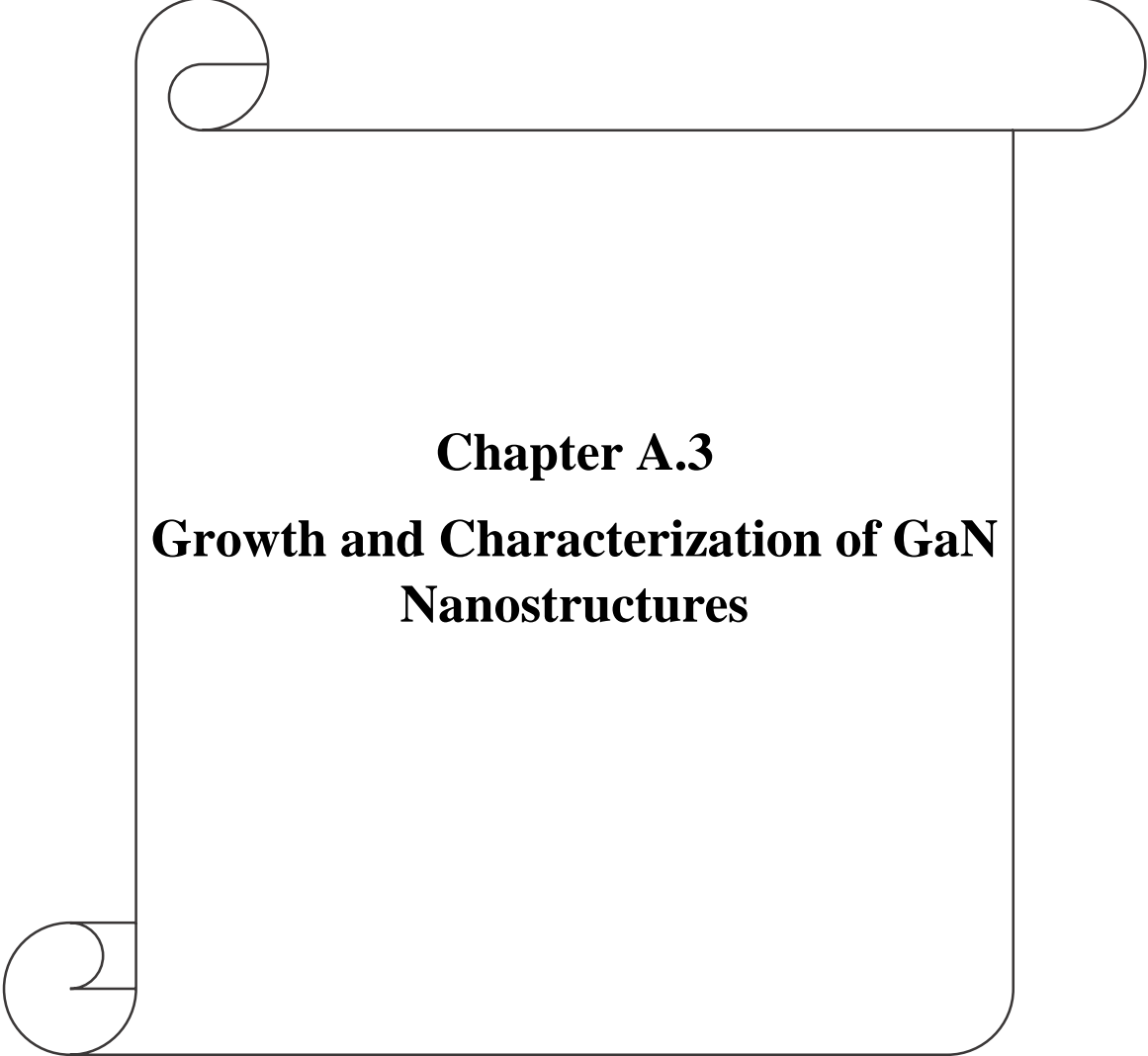

Fig A.2.12: *The representative Raman spectrum of GaN showing E_2 (high) mode and A1 (LO) mode.*

A.2.13 References

1) A.Y Cho and J.F Arthur, Progress in Solid-State Chemistry, Vol. 10, Part 3. pp. 157-191.

2) Image Courtesy: en.rusano.com

3) SVT Associates: http://www.svta.com/

4) A.Y. Cho, Journal of Applied Physics 42,2074 (1974).

5) Ichimiya and P.I. Cohen, Reflection High Energy Electron Diffraction, Cambridge University Press (2004).

6) H.Y Chen, H.W. Lin, C.H. Shen, and S. Gwo, Applied Physics Letters 89, 2431059 (2006).

7) G.I. Goldstein, D.E. Newbury, P. Echlin, D.C. Joy, C. Fiori, and E Lifshin, Scanning Electron Microscopy and X-ray Microanalysis. New York: Plenum press (1981).

8) S.L Chang, X-ray Multiple wave diffraction: Theory and application, Springer- Verlag Berlin Heidelberg (2004).

9) High Resolution X-ray Diffraction, www2009.ph.tum.de, HR-XRD User guide (2009).

10) HR-XRD User guide Bruker instrument D8 Discover HR-XRD.

11) C.V Raman. Nature, 121,619 (1928).

Chapter A.3
Growth and Characterization of GaN Nanostructures

Chapter A.3

Growth of GaN Nanostructures on c-plane Sapphire

This chapter describes the growth of GaN Nanostructures on bare c-plane sapphire using Plasma assisted-Molecular Beam Epitaxy (PA-MBE) and their structural and optical characteristics.

A.3.1 Introduction

Group III nitrides are potential candidates for high-performance optoelectronic devices and in particular GaN semiconductors have gained significance due to their excellent properties and appropriate for high power and high efficiency applications. The band-gap engineering possible in these materials make them tunable over a wide energy range. Formation of defect controlled nanostructures like nanowires, nanocolumns, nanorods and nanowalls with tunable properties is one of the novel approach in the growth of group III nitride films. Now a days much attention has been paid towards GaN nanostructures such as nanowalls, nanowires, and nanorods as they are strain-free and dislocation-free with large surface-to-volume ratio. These exotic properties have made GaN nanostructures superior to conventional 2-D GaN[1]. In spite of all these promising properties fabrication of an electronic device using GaN nanostructures is complicated since the electron flow among individual nanostructures is inhibited by the separation between them. These complexity can be overcome by growing GaN nanowalls which has continuity along the walls around the void regions, which are connected and thus facilitating electron flow in the device fabricated. Kesaria *et al.,* of our own group have reported the growth of GaN nanowall network on sapphire substrate using molecular beam epitaxy (MBE)[2]. Here we present the growth of GaN nanostructures on bare c-plane sapphire substrate utilizing two different Ga flux maintained by two appropriate Ga effusion cell temperatures.

A.3.2 Experimental Section

This experimental study has been performed in (SVT Associate, Inc.) plasma-assisted molecular beam epitaxy system equipped with a standard effusion cell for Ga and a radio frequency (RF) nitrogen plasma source. The RF plasma source was operated at fixed forward power of 350 W. Both Ga vapour and nitrogen plasma flux were measured with a beam flux gauge. The Ga Beam Equivalent Pressure was kept constant at 4.8×10^{-7} Torr, while nitrogen pressure was maintained at 2.5×10^{-5} Torr. Prior to growth, the bare c-plane sapphire substrates were cleaned via chemical treatment, and then degassed at 600°C for 60 min in 1×10^{-9} Torr vacuum in the preparation chamber, and at 800°C for 30 min in the growth chamber. Typical streaky RHEED pattern (not shown here) was observed to ascertain a clean substrate surface before commencing growth. The two samples(**S-1** and **S-2**) discussed in this chapter are grown at a substrate temperature of 630°C and with N_2 flux of 3sccm. Sample S-1 was grown with a Ga effusion cell temperature of 1000°C for 4 hours duration, while sample S-2 was grown at 1100°C for 2 hours. The monitoring of epitaxial growth is done *in situ* by reflection high-energy electron diffraction (RHEED, Stiab) and ex situ by X-ray diffraction (Bruker). The surface morphologies of the GaN microstructures were analysed by a field-emission-scanning electron microscope (FESEM, FEI, *Netherlands*) at an operating voltage of 20KV. PL (Horiba Jobin Yvon) was measured at room temperature using a Xe lamp source with an excitation wavelength of 325 nm. Optical absorption measurements were carried out in the transmission mode configuration using an (Perkin Elmer) Lambda 750 spectrometer. Raman measurements were taken on a Raman spectrometer with 180° back-scattering geometry. A commercial Epilayer (TDI, USA) of 2μm GaN grown by VPE was used in this study as a reference sample, where ever required because of its flat nature.

A.3.3 Results and Discussion

A.3.3.1 Morphological evolution of GaN Nanostructures on c-Al₂O₃.

FESEM images and their corresponding RHEED patterns (viewed along the [10-10] and [11-20] azimuth) of the two GaN films(**S-1** and **S-2**) grown on c-plane Al₂O₃ substrate are shown in **Fig.A.3.1**. The six-fold spotty pattern indicates formation of a wurtzite film with SK growth mode with 3D structures which is in agreement with our FESEM images. **Fig. A.3.1***(S-2)* is the plan view FESEM image and its RHEED pattern of the film grown at 1100°C Ga K-

Cell temperature for 2h. Matrix type surface morphology of this film is composed of nanowalls whose thickness varies from 20 to 50 nm whereas their length varies from 140 to 270 nm. In general, two nanowalls(*S-1 and S-2*) seems to have a common centre, and each nanowall seems to be aligned at 120° angle with each other. The pits amidst these nanowalls have an aerial density of an order of 10^{10} cm^{-2}, which coincides with the aerial density of extended defects expected at a GaN/c-sapphire interface. The spotty RHEED pattern viewed along [11-20] azimuth has an anisotropic spread along the horizontal {1-100} direction which may be due to preferential domain misalignment along horizontal {11-20} direction of the nanowalls[2]. This matrix like surface morphology is due to relaxation of the strain generated in the over layer due to 16% lattice mismatch between GaN and Al$_2$O$_3$ in the early stages of growth.
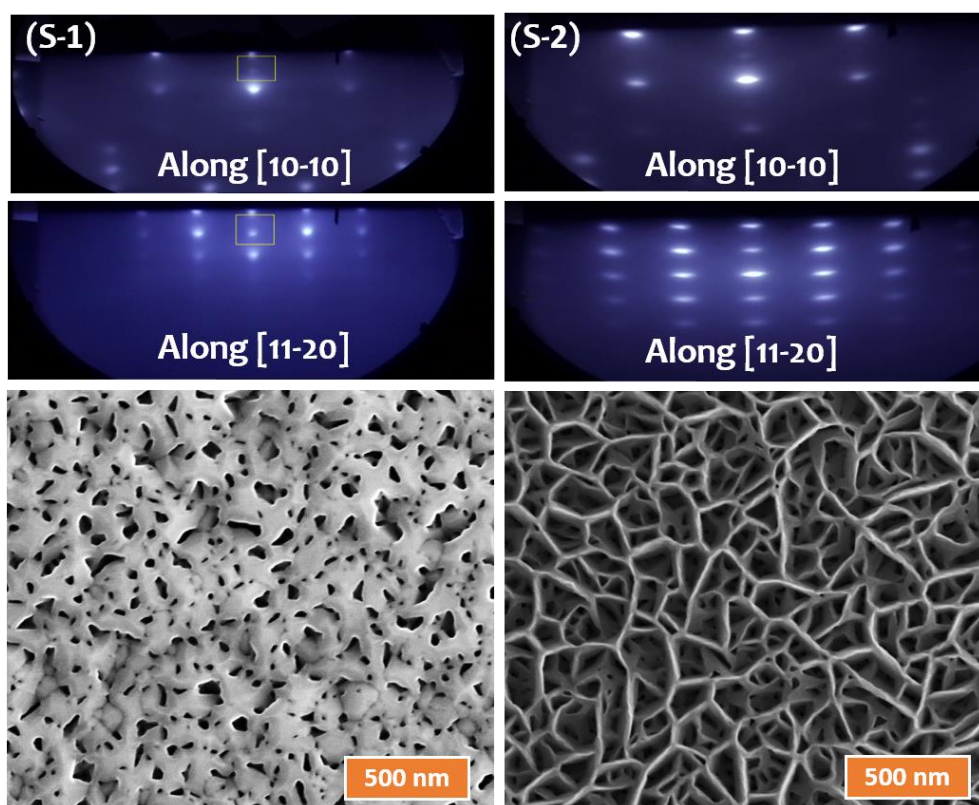
Fig A.3.1: *Plan view FESEM images with their corresponding RHEED pattern of the two GaN films S-1 and S-2.*

Fig. A.3.1*(S-1)* shows plan view FESEM image of film grown at 1000°C Ga K-Cell temperature for 4h. The morphology of GaN film become more compact and flattened. This GaN film shows no nano-sized matrix walls but instead the (blunt) morphology is similar to the typical MBE grown with a V/III ratio of 25, with edge and threading dislocations of order 10^{10} cm^{-2} very clearly visible[3]. RHEED pattern is spotty and seems to be

circular with no horizontal spread which may be due to larger domain size and lesser surface roughness. However the spots are sharp but extended, which may be due to the high defect density in the films. The cross sectional FESEM images of the two films S-1 and S-2 are shown in **Fig.A.3.2** which shows the film thickness as 0.457 nm for S-1 and 1.3μm for S-2.
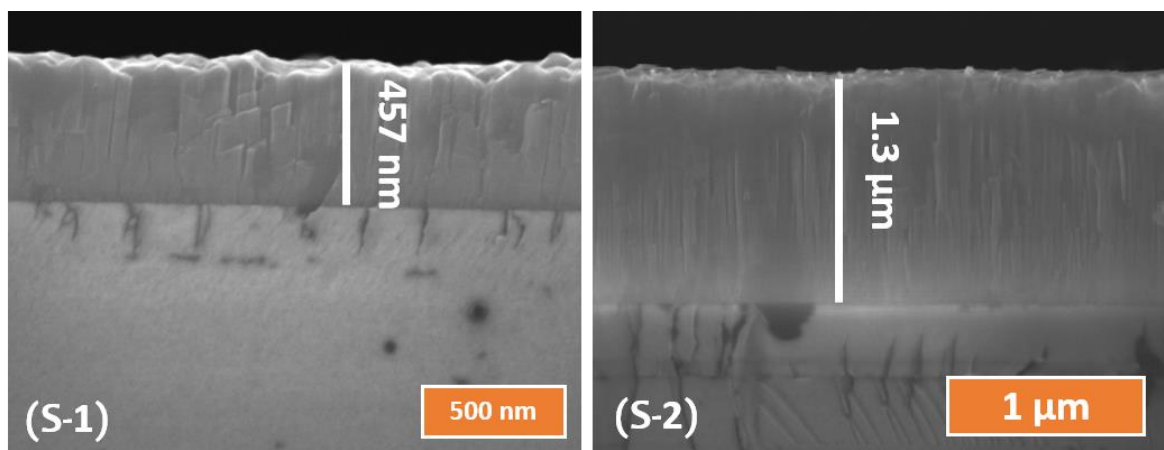
Fig A.3.2: *Cross section FESEM images of the two GaN films S-1 and S-2 grown on c-plane sapphire substrate.*

To compare the surface roughness of the GaN films S-1 and S-2 with Epilayer in addition to morphology we had done AFM imaging which is shown in **Fig A.3.3**. The AFM images show that the Epilayer has the least surface roughness which is evident from its flat morphology and the films S-1 and S-2 have high surface roughness attributed to their 3-D Nano-network morphologies. The surface roughness values are found to be 1.5 nm for GaN Epilayer and 6.5 nm for GaN sample S-1 and 45 nm for GaN Nanowall network sample S-2.
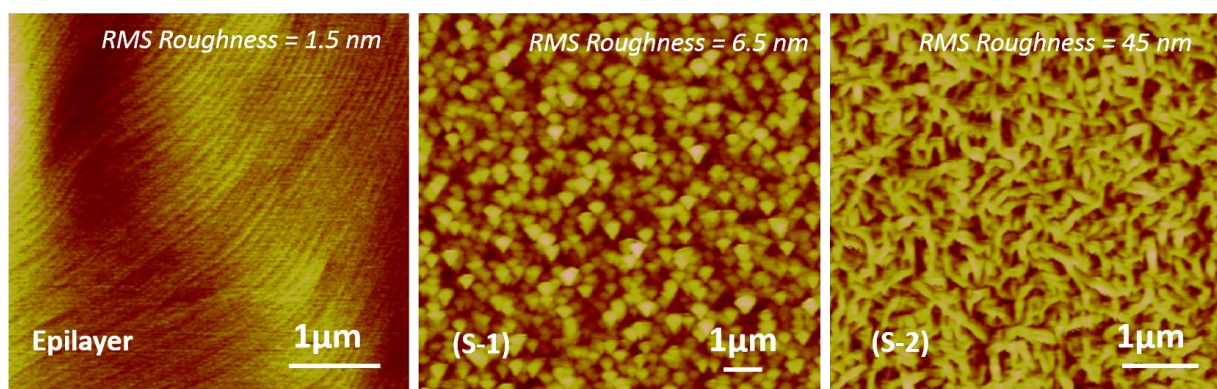

Fig A.3.3: *AFM images of commercially obtained GaN Epilayer and the two GaN films S-1 and S-2 grown on c-plane sapphire substrate.*

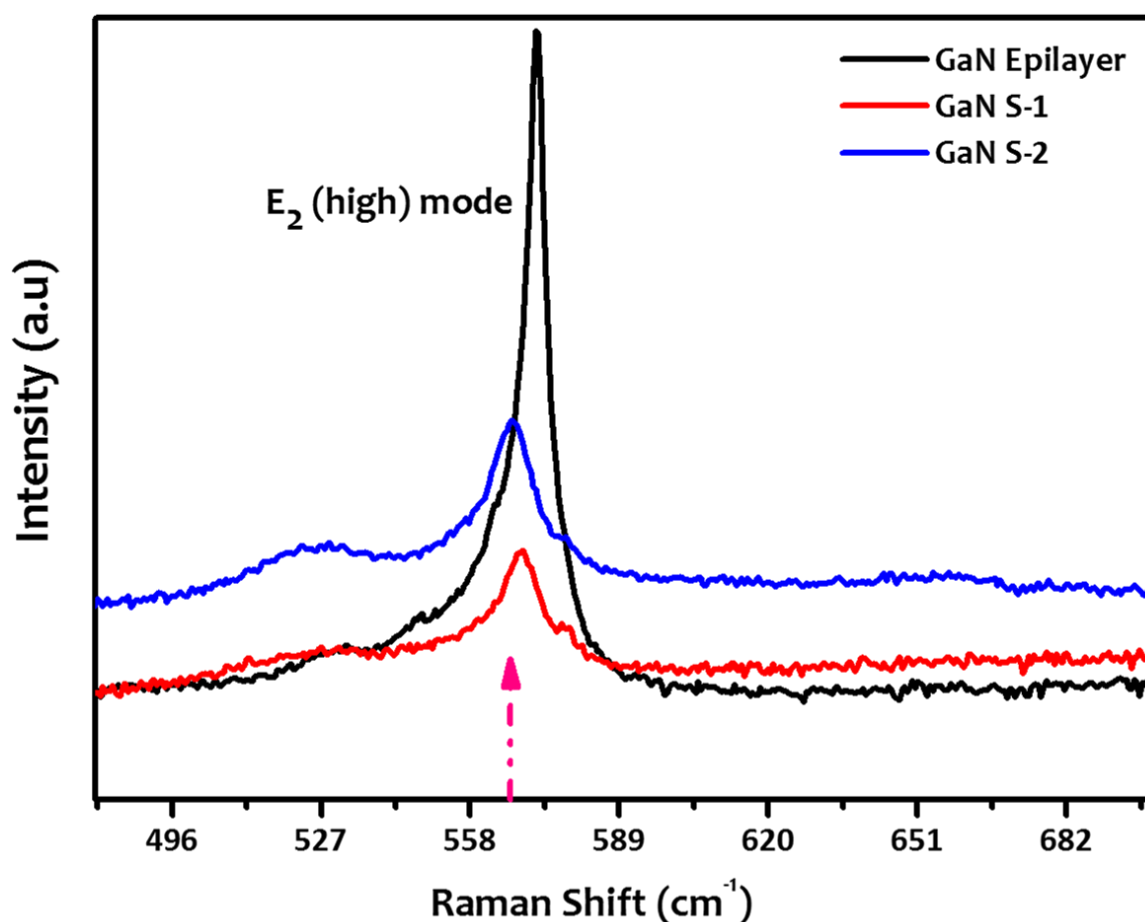## A.3.3.2 Structural characterization of GaN Nanostructures

The crystal structure and the orientation of the films were deduced by XRD (Bruker) using a Cu Kα source operating at a wavelength of 0.15 nm. **Fig.A.3.4** shows the representative XRD pattern of the two MBE grown films S-1 and S-2 showing the characteristic peaks of the wurtzite hexagonal structure. The XRD Peaks at 2θ =34.54° and 72.8° are due to reflections from (0 0 0 2) and (0 0 0 4) plane[3], respectively, of wurtzite GaN. The high intensity of (0002) and (0004) peaks of GaN for both the films showed that the films had high crystallinity and grew along the c-direction epitaxially with respect to the c-plane sapphire substrate. Therefore we conclude that the GaN films grew with their c-plane parallel to the substrate surface. No additional peaks in XRD patterns confirm that the films are single crystalline.
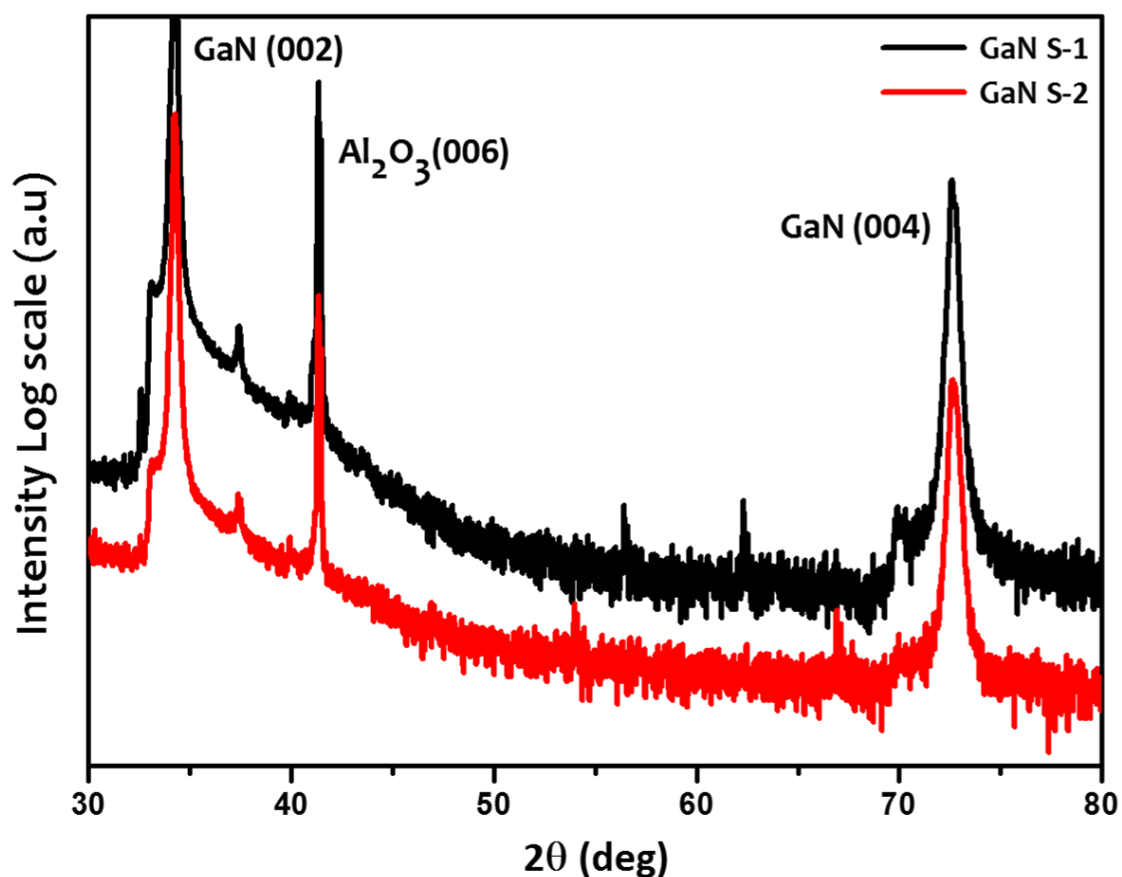
Fig A.3.4: XRD pattern of GaN films S-1 and S-2 grown on c-plane sapphire substrate

The crystalline quality and the stress in the GaN films were further investigated by room temperature Raman Spectroscopy. A typical room temperature Raman spectrum of GaN nanostructured samples grown at different Ga flux and growth duration acquired in the back-

scattering geometry is shown in **Fig A.3.5**. The Raman spectrum is dominated by strong E_2 (high) mode, which manifests due to the vibration of lighter N atoms of GaN and is sensitive to in-plane stress in the films. The GaN epilayer sample shows intense E_2 (high) mode and narrow line width of 6cm^{-1} which is attributed to its high quality and epitaxial nature. The GaN samples S-1 and S-2 shows strong symmetric E_2 (high) mode of line widths 13 cm^{-1} and 12 cm^{-1}, respectively. The Sample S-1 has E_2 line at 568.3 cm^{-1} which has a shift of $\Delta\omega$= +1.9 cm^{-1} (with respect to 566.4 cm^{-1} (Indicated in the **Fig A.3.5** with vertical arrow) of stress free bulk GaN sample) indicating compressive stress in the film. And in case of Sample S-2 the Raman shift was found to be $\Delta\omega$= +0.1 cm^{-1}, which also indicates compressive stress. For both S-1 and S-2 the shifts (+1.9 cm^{-1} and +0.1 cm^{-1}, respectively) are very small in comparison to that of epilayer (+5.3 cm^{-1}), indicating that they are more relaxed than epilayer.
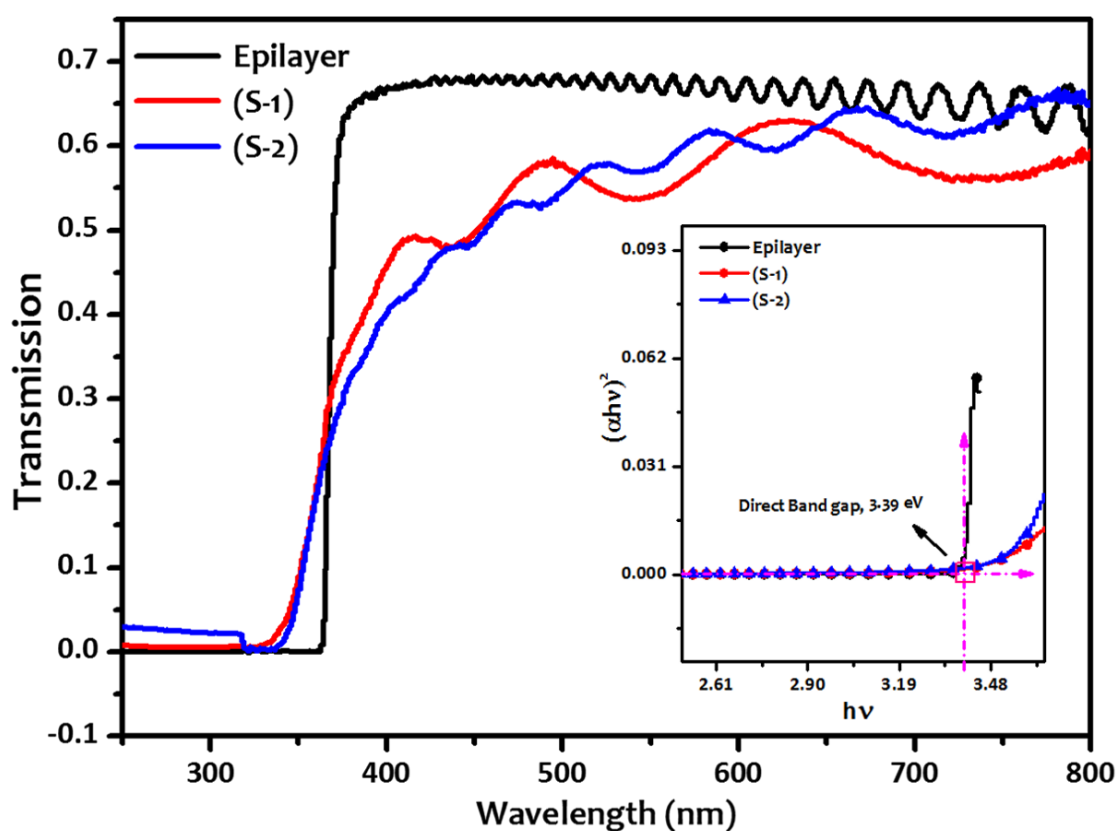

Fig A.3.5: *Raman Spectra of GaN Epilayer and films S-1 and S-2 grown on c-plane Sapphire substrate. The vertical arrow indicates the Raman shift 566.4 cm^{-1} for stress free bulk GaN Sample.*

A.3.3.3 Optical Characterization of GaN Nanostructures

The absorption measurements were taken in transmission mode on Perkin Elmer Lambda 750 UV-Vis-NIR spectrometer. For all the measurements bare c-plane sapphire substrate was used as blank or reference. Mechanisms which broaden or shift exciton resonance such as impurities, doping, strain, and phonon interactions, in turn, broaden or *shift the absorption edge* and influence optical constants near bandgap[4]. The transmission spectra shows up interference fringes due to the interference phenomenon by light wave travelling through the two layer dielectric-stack **air/GaN/Sapphire/air**[4].

Fig A.3.6: *Transmission Spectra of GaN Epilayer and GaN films S-1 and S-2 grown on c-plane Sapphire substrate. The inset indicating tauc plot for direct bandgap.*

If the thickness of the film is not uniform or is slightly tapered then the interference effects are destroyed and the transmission will be a smooth curve[5]. **Fig A.3.6** shows the transmission spectra of GaN Epilayer and GaN samples S-1 and S-2. The amplitude of the adjacent maxima and minima of the interference fringes is significantly less for GaN samples S-1 and S-2 in comparison to GaN Epilayer due to the rough 3-D morphology, which scatters

the incident light resulting in reduced transmission. The bandgap was found to be 3.39 eV for GaN epilayer, 3.66 eV for S-2, and 3.7 eV for S-1. The variation in the bandgap is due to the different thickness of the films exhibiting confinement effect. The thicknesses of the samples are 2μm, 1.3μm and 457nm for epilayer, S-1 and S-2, respectively.

Room temperature Photo-luminescence (using Horiba, Jobin Yvon) was measured using a Xe lamp source with an excitation wavelength of 325 nm and slit width of 3nm. **Fig A.3.7** shows the room temperature normalized PL spectra of GaN Epilayer and GaN samples S-1 & S-2. The inset shows the intensity comparison of the photoluminescence spectra of the three films obtained under similar conditions. The GaN samples S-1 and S-2 with blunt and Nanowall network morphology have the highest PL intensity of the near band edge peak at 3.39 eV and 3.45 eV, respectively. The sample S-2 with nanowall network morphology not has any defect related band, while sample S-2 with blunt morphology has a defect related peak around 2.2 eV (Green) which may be attributed to defect related yellow luminescence peak. The epilayer showed a peak close to the band gap value at 3.42 eV; but there also was an intense deep-level defect-related peak at 2.3 eV. The value of the near band edge peak for bulk (unstressed) GaN film was taken to be 3.40 eV[6]. The blue shift in the two films, epilayer and sample S-1 was 20 meV and 30 meV, respectively. A red shift of 10meV was observed in the sample S-1 in comparison with near band edge peak of bulk unstressed GaN film.

Similar shifts of 30 meV are shown for GaN films grown on bare c-plane sapphire[7], and Rieger et al.,[8] report a strain related blue shift of 27 ± 4meV/GPa for GaN thin films grown on c-plane sapphire with a thin AlN intermediate layer. The blue shift is also known to be caused by a partial reduction of the piezoelectric field due to nanostructuring[9]. The FWHM of the PL linewidths were 140 meV for S-1, but increased to 180 meV for S-2, while that of the epilayer was 90 meV, suggesting the presence of band tail states in the conduction band[10]. The absorption profiles of the films were not sharp, (*as seen from the transmission spectra fig A.3.6*) indicating that the absorption took place over a range of energies available at the band tail states.

The flat epilayer with minimal surface states, on the other hand showed a sharp absorption band edge and interference fringes (**Fig. A.3.6**), characteristic of a flat film.
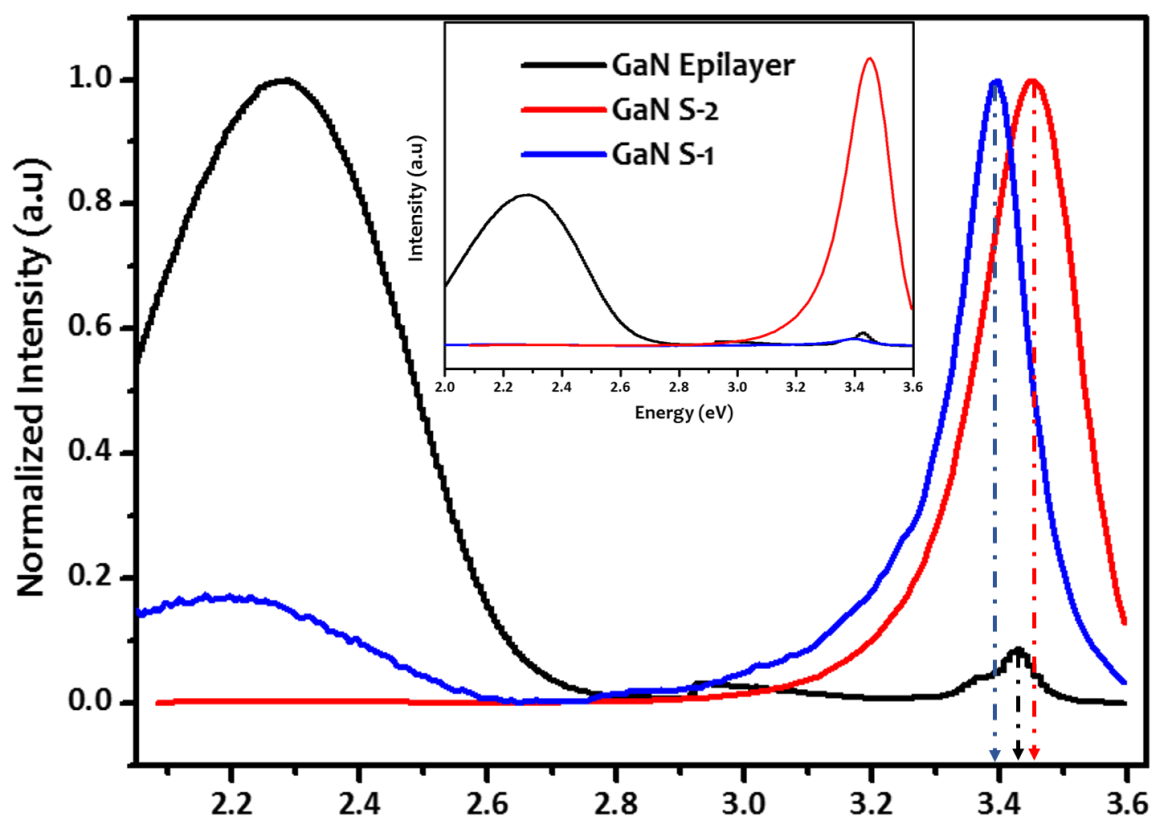
Fig A.3.7: *Room temperature PL Spectra of GaN epilayer and GaN films S-1 and S-2 grown on c-plane Sapphire substrate. The inset shows the intensity comparison of PL spectrum of all the films under similar conditions.*

A.3.3.4 Hall measurements of GaN Nanostructures

Hall measurements were carried out in the standard Van der Pauw geometry. Indium contacts were made on the films for ease of operation. Ohmic nature of the contacts was established by plotting the I-V curves prior to hall measurements. Following **table A.3.1** presents a summary of the Hall measurements performed at room temperature (300 K) for GaN epilayer and GaN samples S-1 and S-2. It is observed that all of them showed a negative Hall coefficient, indicating that the majority carriers are electrons and samples S-1 and S-2 show carrier concentrations $\sim 10^{20}$ cm^{-3}, and low mobility ($\sim$13-16 cm^2/V-s). This low mobility can be understood keeping in mind the morphology of our samples, which encircle giant

dislocations. Over the years, as-grown GaN samples are known to be *n*-type semiconductors without intentional doping, implying the presence of donors. These donors must be associated with defects or impurities, since perfect GaN cannot provide thermal carriers. This has been thought to be caused by the spontaneous formation of nitrogen vacancies. In GaN the defect with the overall lowest formation energy is the nitrogen vacancy, under both Ga-rich and N-rich conditions. If deviations from stoichiometry occur due to point defect formation, they will therefore always tend toward nitrogen-deficient material (even under N-rich conditions) [11, 12]. This was confirmed by explicit self-consistent calculations of point-defect concentrations and stoichiometry. The reason for this asymmetry in GaN can be found in the high binding energy of nitrogen molecules, which makes it difficult (or even impossible) for the GaN solid to ever become nitrogen-rich: Nitrogen atoms must prefer to leave the solid and become part of N_2 molecules, rather than incorporating in the solid in the form of nitrogen-rich point defects[12]. When the material shows n type conductivity, it facilitates the formation of Ga vacancies in the system[13].

Properties	GaN Epilayer	GaN Sample S-1	GaN Sample S-2
Carrier Concentration (cm^{-3})	-10^{18}	-10^{20}	-10^{20}
Mobility (cm^2/Vs)	77	16	13
Resistivity (ohm-cm)	5.2×10^{-2}	2.3×10^{-3}	3×10^{-3}
Magneto-resistance (ohm)	1.2×10^{0}	4.7×10^{-2}	5.35×10^{-2}
Sheet Concentration (cm^{-2})	10^{14}	10^{15}	10^{16}

***Table A.3.1:** Summary of Hall Measurements.*

Moreover, existing reports on GaN thin films have shown that the Ga vacancy concentration correlates with the intensity of the yellow luminescence at 2.2 to 2.3 eV, suggesting that the acceptor states of V_{Ga} (gallium vacancy) are involved in this optical

transition. The YL was also found to be stronger in samples grown under N-stable conditions in MBE consistent with higher V_{Ga} concentrations when the growth is more N rich.

Hence, detailed information about the nature of vacancies present in our system can further need to be de-convoluted by a rigorous analysis of Photoluminescence (PL) and transport measurements.

A.3.3.5 Brief XPS analysis of GaN Nanostructures

To know the surface composition of the GaN samples XPS measurements were acquired and peaks corresponding to major elements Gallium, Nitrogen, Oxygen and Carbon were observed. All the spectra were corrected for the shift during measurements by taking C-1s peak as reference. Surface elements are indicated by taking highest intensity prominent peaks. **Fig A.3.8** shows the XPS spectra for the GaN samples indicating various elements present on the surface. The peak positions are summarized in **table A.3.2**. Apart from Ga and N, oxygen and Carbon contamination was also observed. This C contamination can be due to handling of samples in open air, whereas sources of oxygen impurities need not be the same. It was possible to get rid of the contamination via energetic 2keV Ar+ ion sputtering (spectrum not shown here), and then it was confirmed that the GaN films were clean, while the contaminants were only on the surface due to sample handling.
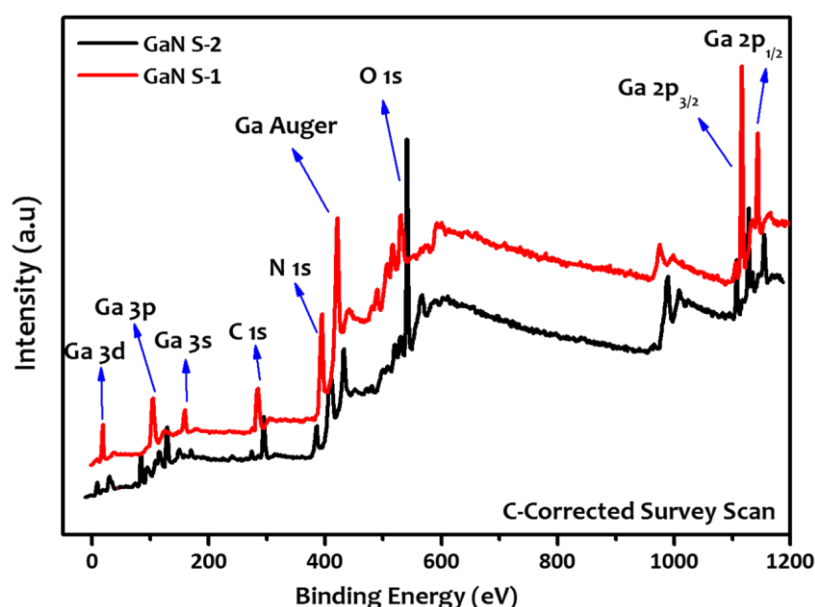
Fig A.3.8: *XPS Spectra of GaN films S-1 and S-2 grown on c-plane Sapphire substrate.*

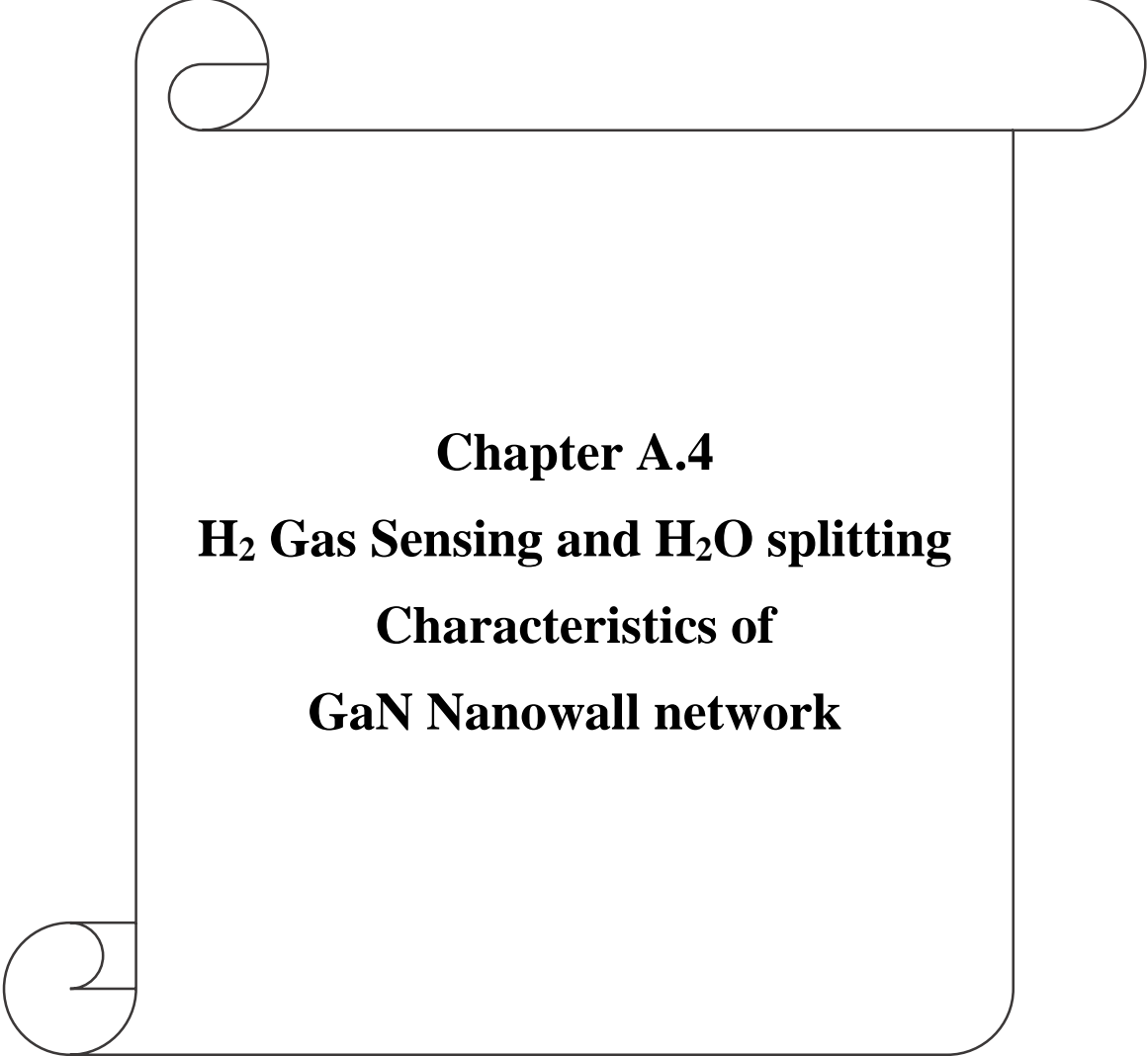| Peak /Element Name	XPS Peak Position (eV) in GaN	
	(S-1)	(S-2)
Ga 3d	18.0	19.5
Ga 3p	104.0	104.5
Ga 3s	159.0	159.5
C1s	284.5	284.5
N1s	395.0	396.5
Ga Auger	421.0	422.5
O 1s	530.0	530.0
Ga 2p $_{3/2}$	1116.0	1117.5
Ga 2p $_{1/2}$	1143.0	1144.5

Table A.3.2*: Summary of XPS Peaks and peak positions.*

A.3.4 Summary

In summary, GaN nanostructured thin films of different morphology were grown by varying Ga flux and growth time. The grown films are characterised for their structural, optical and electrical properties. The films with different thickness show corresponding variation in the bandgap obtained from transmission measurements, which may be attributed to confinement effect. In particular GaN S-2 which has nanowall network morphology shows a very intense PL near band edge emission without any defects, while both epilayer and S-1 show up defect related emission around 2.2 eV. The PL was found to be broad even at low temperature (at 10K) and we attribute this broadness may be due to band tail states near conduction band edge. The GaN S-2 also shows intense Raman active E_2 (high mode) with very less shift (of $\Delta\omega$=+0.1 cm^{-1} with respect to unstressed bulk GaN), indicating more relaxed compared to GaN epilayer ($\Delta\omega$=+5.3 cm^{-1}).

A.3.5 References

1) Aihua Zhong and Kazuhiro Hane, Nanoscale Research Letters 2012, 7:686.

2) Manoj Kesaria, Satish Shetty and S.M Shivaprasad, Journal of Crystal Growth 326 (2011) 191–194.

3) J.C. Johnson, H.-J. Choi, K.P. Knutsen, R.D. Schaller, P. Yang, R.J. Saykally, Nat. Mater. 1 (2002) 106

4) J.F Muth et al., Appl. Phys. Lett. 71 (18), 3 (1997).

5) R Swanepeol, J.Phys. E: Sci. Instrum., Vol. 16, 1983.

6) S. Strite, H. Morkoç, J. Vac. Sci. Technol. B 10 (1992) 4.

7) C. Kisielowski, J. Krüger, S. Ruvimov, T. Suski, A.W. Ager III, E. Jones, Z. Liliental-Weber, M. Rubin, E.R. Weber, M.D. Bremser, R.F. Davis, Phys. Rev. B 54 (1996) 24.

8) W. Rieger, T. Metzger, H. Angerer, R. Dimitrov, O. Ambacher, Appl. Phys. Lett. 68 (1996) 970.

9) V. Ramesh, A. Kikuchi, K. Kishino, M. Funato, Y. Kawakami, J. Appl. Phys. 107 (2010) 114303.

10) H.P. Bhasker, S. Dhar, A. Sain, M. Kesaria, S.M. Shivaprasad, Appl. Phys. Lett. 101 (2012) 132109.

11) J. Neugebauer and Chris G. Van de Walle, Phys. Rev. B 50, 8067 (1994)

12) Chris G. Van de Walle, J. Neugebauer J. Appl. Phys. 95, 3851 (2004)

13) III-V Nitride Semiconductors: Defects and Structural Properties M.O. Manasreh (Ed.), 2000 Elsevier Science.

Chapter A.4
H$_2$ Gas Sensing and H$_2$O splitting Characteristics of
GaN Nanowall network

Chapter A.4

Studies on water splitting and gas sensing properties of GaN nanowall network

Nanoporous (NP) semiconductors are interesting structures in that their mechanical, electrical, and optical properties can be modified significantly from their host materials. It should be noted that the material property can be tuned with porosity, periodicity, and height of the nanopores, so they may be considered as a new material with variable material parameters. Moreover, their greatly increased surface area makes them promising for an electrode in electrochemical (EC) surface reaction and for gas sensing.

A.4.A Photo-electrochemical water splitting studies on GaN Nanowall network.

A.4.A.1 Introduction

To effectively address the depletion of fossil fuels and the serious environmental problems accompanying their combustion, modern society has been searching for new forms of energy that are clean, renewable, cheap, safe, and viable alternatives to fossil fuels and nuclear energy.

The efficient utilization of solar energy could alleviate many energy and environmental issues, as the solar energy irradiating the surface of the Earth (1.3×10^5 TW) exceeds the current global human energy consumption (1.6×10^1 TW in 2010[2]) by roughly four orders of magnitude. In this direction, overall water splitting under sunlight has received much attention for production of renewable hydrogen from water on a large scale[1-4]. Since the discovery of the Honda–Fujishima effect in the early 1970s, which demonstrated photo-assisted electrochemical water oxidation on an n-type TiO_2 single-crystal electrode by band-gap excitation,[5] photo-catalytic and photo-electrochemical (PEC) water splitting on semiconducting materials has been studied extensively. Photo-electrochemical (PEC) water splitting is regarded as a promising solution to produce H_2, a renewable energy carrier, from abundant and clean resources of sunlight and water.

Thermodynamics of photo-electrochemical water splitting.

When a semiconductor absorbs photons with energies higher than its band gap energy, electrons in the valence band are excited to the conduction band. As a result, excited electrons and holes are generated in the conduction and valence bands, respectively. These photogenerated carriers can drive reduction and oxidation reactions if the charge injections into the reactants are thermodynamically favourable.

When a semiconductor electrode is immersed in an electrolyte solution, electron transfer takes place between the semiconductor and the electrolyte solution so that the Fermi level is equilibrated with the redox potential of the electrolyte solution.[6] An electrolyte solution accepts (/donates) electrons from (/to) a semiconductor when the Fermi level of the semiconductor is more negative (/positive) than the reduction potential of the electrolyte solution. Since the density of electrons in a semiconductor is finite and the potential of the band positions at the interfaces can be pinned, the electron transfer causes band bending.

In electrodes of n-type semiconductors, which act as *photoanodes*, photoexcited holes accumulate on the surface of the semiconductor and are consumed in oxidation reactions, while electrons are transferred to a counter electrode via the back contact and an external circuit, and used in reduction reactions, as shown in **Fig. A.4.A.1 (a)**. The top of the valence band must be more positive than the oxygen evolution potential to allow a photoanode to generate oxygen.

On the other hand, a p-type semiconductor works as a *photocathode* for hydrogen evolution when the conduction band edge is more negative than the hydrogen evolution potential as shown in **Fig. A.4.A.1 (b)**.

Accordingly, PEC reactions on photoelectrodes are driven by photoexcited minority carriers in both cases. The potential of electrons on the counter electrode is identical to the Fermi level of the photoelectrode under photoexcitation. An external voltage can be applied between a photoelectrode and a counter electrode to compensate for the potential deficiency in order to drive redox reactions on a counter electrode even if the Fermi level of the photoelectrode is positioned at an undesirable potential. In such a case, the external power input, which is the product of the current and the applied voltage, should be subtracted from the energy output when the energy conversion efficiency is considered.[7]

Alternatively, a photoanode and a photocathode can be connected in tandem as in Z-scheme water splitting (see **Fig A.4.A.1(c)**) instead of using a single photoelectrode and a counter electrode.
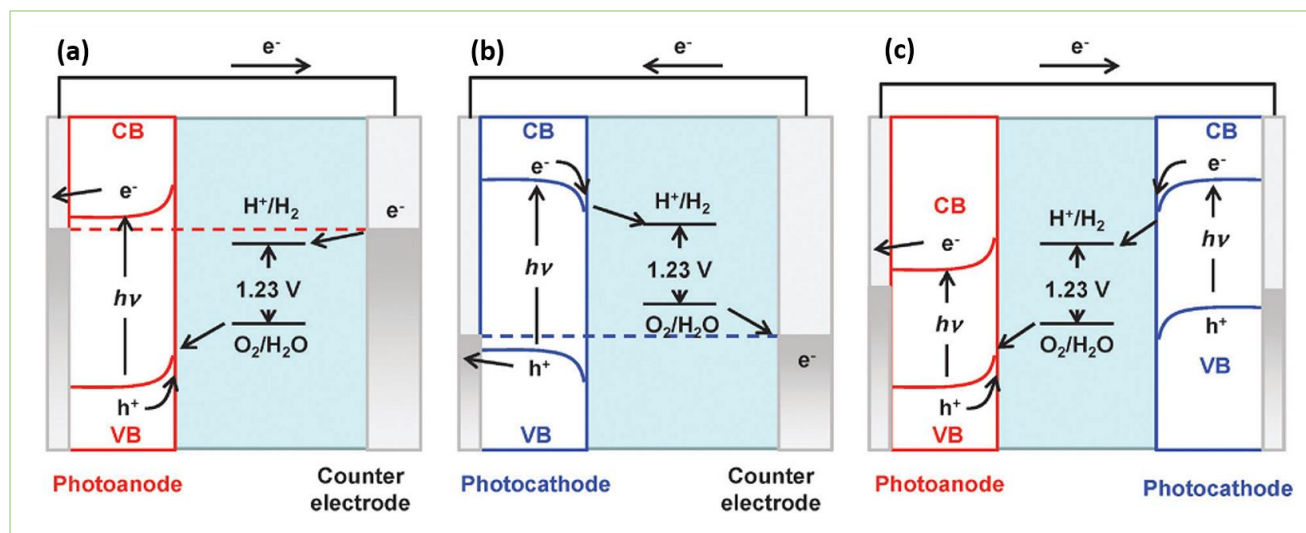
Fig. A.4.A.1: *Energy diagrams of PEC water splitting using (a) a photoanode, (b) photocathode, and (c) photoanode and photocathode in tandem configuration. The band gaps are depicted smaller in (c) to emphasize that semiconductors with a narrow band gap can be employed.* ***Adapted from[1] with permission © Royal Society of Chemistry 2014.***

In the tandem configuration, the maximum photocurrent and the working potential of the photoelectrodes are theoretically determined by the intersection of the steady current–potential curves of the respective photoelectrodes.[8] The best performing photoelectrochemical devices known today are Tandem cells, in which the necessary potential for water electrolysis is produced by a combination of two or more semiconductors connected in series. The advantage of this 'Tandem' configuration is that semiconductors with smaller bandgaps can be used, which absorb a greater fraction of the solar spectrum.

Recently, the use of group III nitride semiconductors for water splitting has attracted considerable attention[9]. Due to the more negative potential of the nitrogen 2p orbital, compared to that of the oxygen 2p orbital, metal nitrides often possess a narrow band gap and can potentially encompass nearly the entire solar spectrum. Moreover, the inherent chemical stability of nitrides also favours their use in the harsh photo-electrochemical reaction environment[10]. Photovoltaic devices composed of III-V materials have the highest conversion

efficiency of any solar conversion system[20]. However, when used in photo-electrochemistry these materials show very short lifetimes due to photocorrosion. A non-traditional III-V nitride that shows excellent stability as a PEC device is GaN. Its band edges meet the energetic overlap condition, the only known single junction III-V that does. Its stability is a property rarely observed in III-V semiconductors.

In this work (***done in collaboration with Prof Sampath, IPC, IISc, Bengaluru***), we have attempted to use the GaN nanowall network for pure water splitting.

Our work was motivated by the large surface to volume-ratio of the GaN nanostructure grown in our lab that may enhance the light absorption and also it's straddling band alignment with the redox potential of water.

A.4.A.2 Experimental Method and Setup

A conventional three electrode configuration in a single compartment cell was used with GaN Sample, Platinum (Pt) and saturated standard calomel electrode (SCE) as working, counter, and reference electrodes, respectively. Xenon arc lamp was used as an excitation source. The electrical contacts are made using In metal. Photocurrents as a function of electrode potential were measured with a scanning potentiostat. Freshly prepared 1.0 M HBr solution was used as electrolyte solution. A schematic of the setup used is shown in **Fig A.4.A.2**. For the experiment, a 0.6µm GaN nanowall network (n $=5x10^{20}$ cm^{-3}) was grown on the c-plane sapphire substrate by molecular beam epitaxy. For comparison a commercial GaN epilayer of 2µm obtained from TDI, USA was used. The surface morphology of the GaN nanowall network and epilayer is displayed in **Fig A.4.A.3**.

The GaN nanowall network and GaN epilayer were used as *photoanodes* during water splitting experiments in the HBr electrolyte under the illumination of light from Xenon arc lamp. The current–voltage (I–V) characteristics were measured under dark and illumination, while a Pt counter electrode was used as a cathode. The generation rate of H₂ gas was indirectly evaluated by measuring the photocurrent.
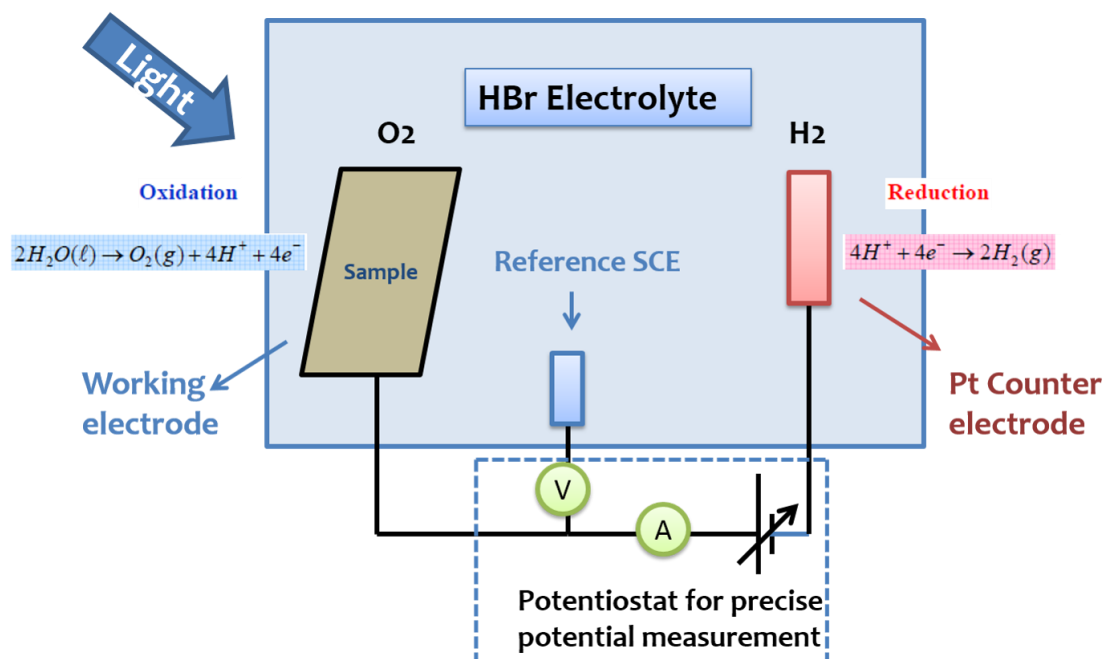
Fig A.4.A.2: *Schematic of experimental setup used in the present study.*
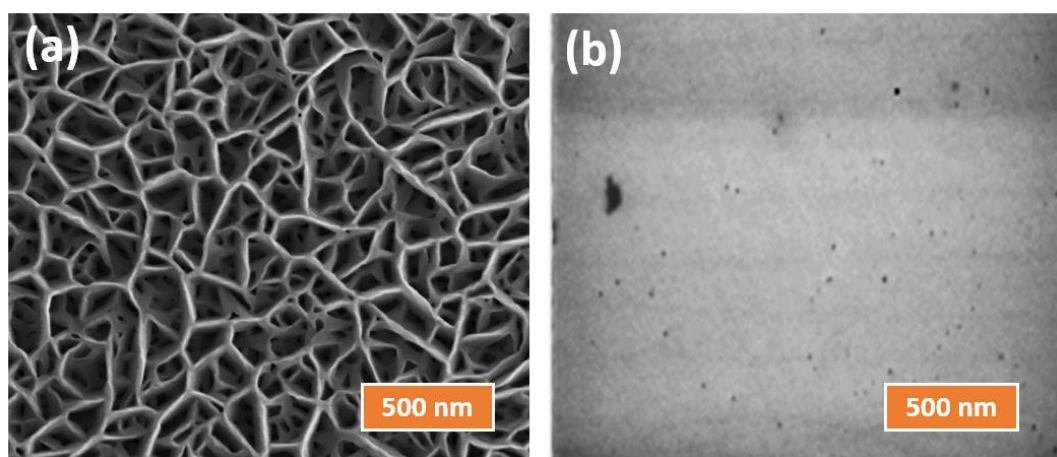

Fig A.4.A.3: *The plan view FESEM images of (a) GaN nanowall network and (b) GaN epilayer.*

A.4.A.3 Results and Discussion

Figure A.4.A.4 (*Linear Sweep Voltammogram*) shows the photocurrent density as a function of voltage applied between working electrode and counter electrode in 1.0 M HBr electrolyte. It compares the photo-anode performances of GaN nanowall network and planar GaN epilayer. The measured photocurrent density of GaN epilayer was higher even at zero applied voltage, while for GaN nanowall network the photocurrent density starts increasing

especially when the applied bias was above 1.25 V. It may be attributed to the current crowding at the semiconductor∕electrolyte (S∕E) interface. As was reported by Waki *et al*, current crowding degraded water splitting efficiency considerably when the density of photogenerated carriers at the S∕E interface was high[11].
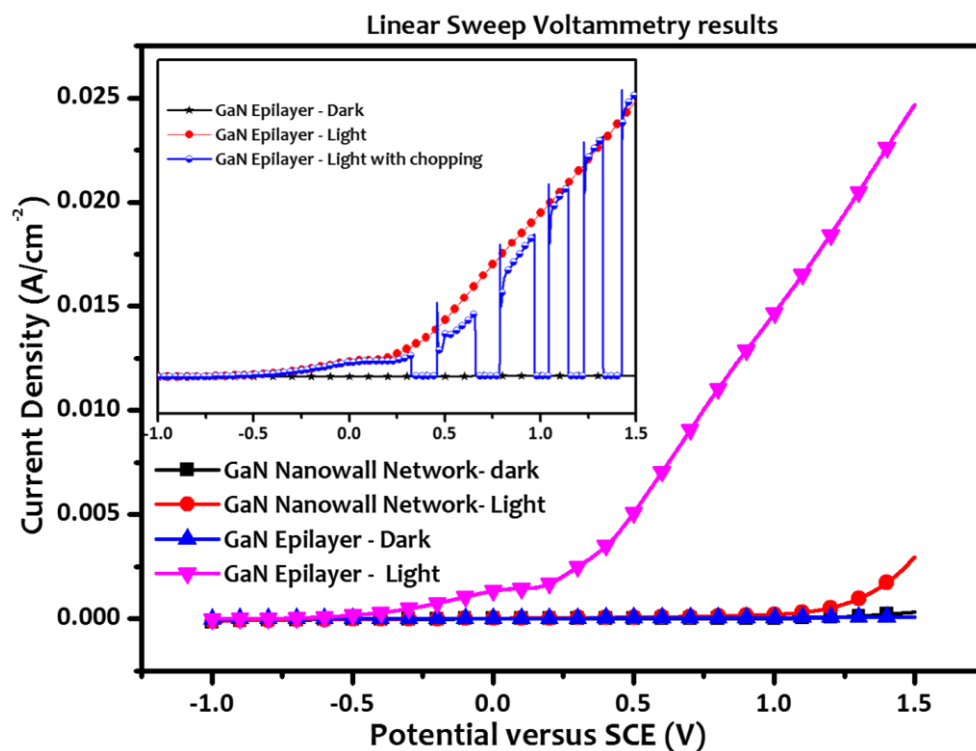
Fig A.4.A.4: Photocurrent–potential curves of Nanowall network GaN and planar GaN photoanodes. Dark currents are shown for comparison. The inset shows PhotoCurrent-Voltage curve for Epilayer with chopping the light in between manually during experiment.

The stability of the photoanodes were characterized at different applied voltages and **Fig A.4.A.5** shows the photocurrent density as a function of operation time at repeated on/off cycles of illumination. Both GaN nanowall network and GaN epilayer electrodes showed almost no degradation of the water splitting efficiency with time; the planar GaN epilayer showed higher photocurrent density even at zero applied voltage as discussed before and its magnitude still increased with applied voltage (not shown here for clarity of the figure). While GaN nanowall network showed comparatively little photocurrent even at higher applied voltages of 0.5 and 1V.
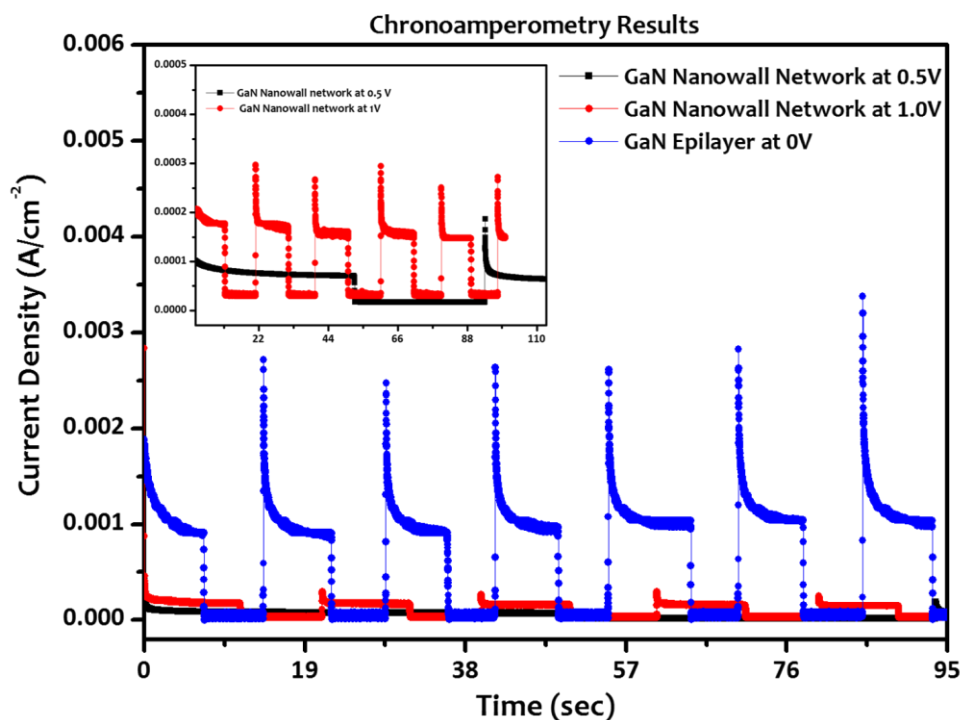
Fig A.4.A.5: *Degradation of photocurrent as a function of water splitting time at repeated on/off cycles of illumination for GaN epilayer at 0V and GaN nanowall network at 0.5 and 1V. The inset shows the same graph without the curve for GaN epilayer for clarity.*

A.4.A.4 Conclusions and Future outlook

It turned out that the commercial GaN epilayer itself was superior to GaN nanowall network for photo-electrochemical water splitting without any applied external voltage. The reason for the inability of GaN nanowall network for water splitting at lower applied voltage may be attributed to the current crowding at the semiconductor/electrolyte interface, which is widely accepted in literature. So we need to think forward towards reducing carrier concentration in GaN nanowall network to make it to show superior water splitting properties. However with applied voltage 1.3V and above, we have found that the magnitude of the photocurrent is higher for GaN Nanowall network than epilayer. It appears that we need to study some more samples by controlling defects to reduce the operating voltage.

Although direct, the band gap of GaN (3.4 eV) is too wide for terrestrial solar applications; it absorbs only in the UV, leading to low photo electrochemical efficiency. But by bandgap engineering of GaN, AlN and InN, bandgap can be tuned to absorb the full solar spectrum ranging from red, well into the ultraviolet, without disturbing much of its crystal structure.

A.4.B H$_2$ Gas Sensing studies on GaN Nanowall network.

A.4.B.1: Introduction

It is of great interest to develop a hydrogen (H$_2$) sensor that is capable of operating in harsh environmental conditions such as chemically corrosive ambient. Because of its high resistance to acids and alkalis as well as large band gap (3.4 eV), H$_2$ sensor based on GaN semiconductor could be used for many harsh applications. These include gas sensing operations in a chemical reactor processing, fuel leak detections in space vehicles as well as automobiles, and emissions from industrial process. For these sensors, it is important to operate with minimum power consumption near room temperature, especially for a long-term H$_2$ monitor.

H$_2$ sensors on the planar GaN film has been investigated. A resistive type H$_2$ sensor on a GaN film was demonstrated in 2005[12]. The primary researches are focused on the platinum (Pt) or palladium (Pd)/planar GaN film Schottky diode type H$_2$ sensors, of which the catalytic metal Pt or Pd dissociates the H$_2$ molecules to H atoms [13, 14]. Schottky diodes are well formed on the planar GaN film, exhibiting high sensitivity and stability. Additionally, a Pt/SiO$_2$/GaN (MIS, metal–insulator semiconductor) Schottky diode type H$_2$ sensor also has been investigated by Tsai and co-workers, which improves the sensitivity, response time, and thermal stability[15, 16]. Both the resistive and Schottky type H$_2$ sensors on the GaN film, however, are required to be heated, typically to 200 °C[12, 14]. The response time[14] is about 7 min in 980 ppm H$_2$ at 60 °C. On the other hand, nanostructures are promising in improving the performance of H$_2$ sensor due to its confinement effects and large surface area to volume ratio[17, 18]. (*Excerpt reused with permission from[19] © Elsevier 2014*).

A.4.B.2: Experimental Section

In this work (***which is done in collaboration with Prof. Navakantha Bhat of Centre for Nanoscience and Engineering, IISc, Bengaluru***) we have attempted to study the resistive type H$_2$ sensor on GaN nanowall network. The porous GaN nanowall network (0.6μm thick) is of high quality and was epitaxially grown on c-plane (0001) sapphire substrate by MBE.

Different from a separated nanowire or nanotube, the porous GaN nanowall network is continuous and aids electric current in the lateral direction. Because of its in-plane electrical conductivity, fabrication of an electrical device on the porous GaN nanowall network is expected to be as easy as that on a planar GaN film. Device structures consisting of 15μm and 100μm interdigitated electrodes of platinum (90 nm thick) were deposited using RF magnetron sputtering and patterned using photo-lithography inside clean room.

The experimental setup mainly consists of Keithley multimeter to measure current, applying constant voltage to the GaN sensing device. The device is mounted on a graphite block which in turn equipped with eurotherm temperature controller. Mass flow controllers are used to allow known amount of gas to be passed over the device. The H_2 gas diluted with 80% of N_2 is used for sensing measurements with synthetic air as reference gas. A schematic of the setup is shown in **Fig A.4.B.1**.
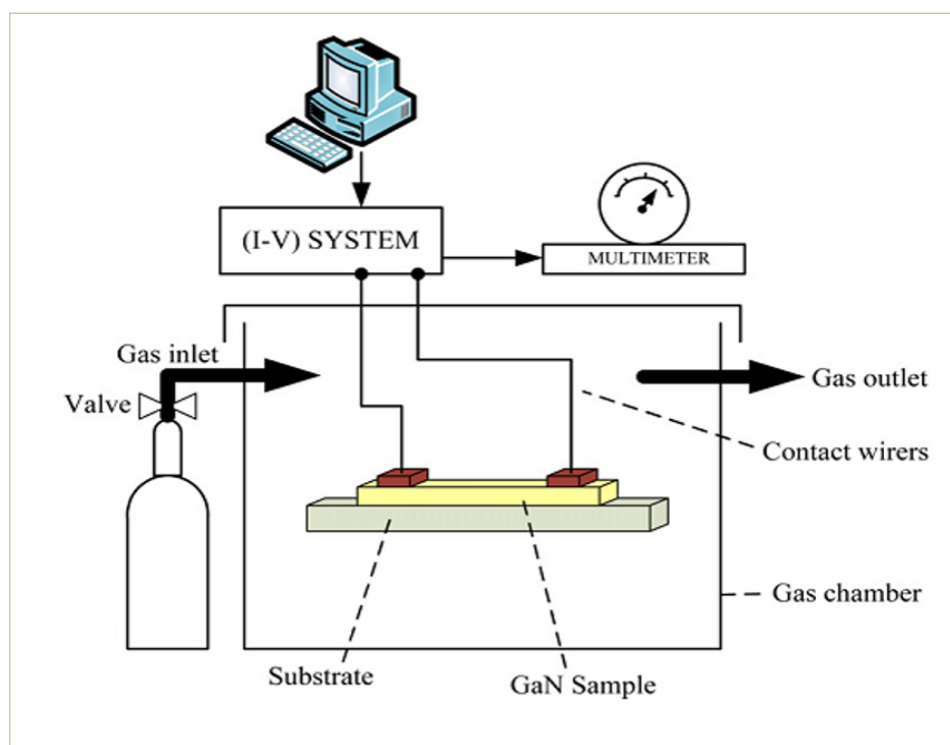
Fig A.4.B.1. *Schematic of gas sensing experimental setup.*

A.4.B.3: Results and discussion

The optical image of the device structure is displayed in **Fig A.4.B.2 (a),** along with FESEM micrographs of GaN nanowall network in which GaN nanowalls overlap and interlace with one another, forming an in-plane electrically conductive porous nanostructure. The typical width of the GaN nanowall and the size of the pores may be 150 and 200 nm, respectively. In the gas sensing process, the diffusivity of gases into sensor and their reactivity with sensitive material together determine the performance of a gas sensor.
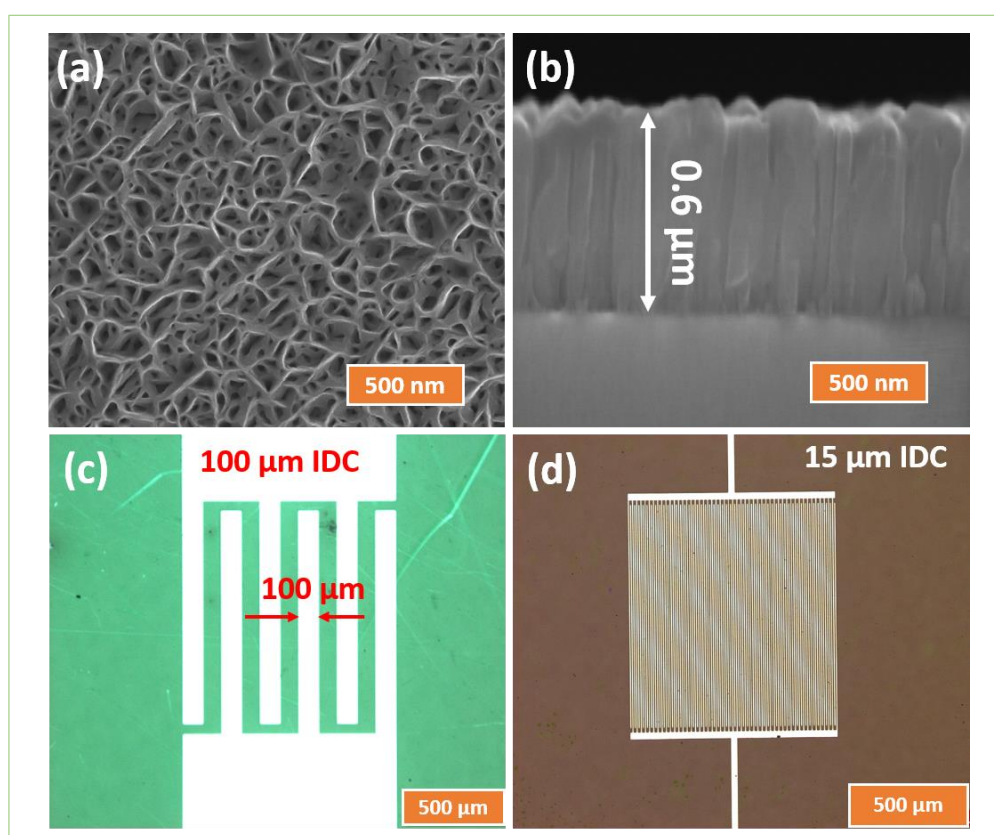

Fig A.4.B.2: *(a) Plan view FESEM and (b) Cross section image of GaN nanostructure, and (c) and (d) optical image of device structures.*

Gas Sensing Measurement:

Fig A.4.B.3 shows the change in the resistance of the Pt/Porous GaN nanostructure device as a function of time in 1000 ppm of H_2 gas diluted in synthetic air at various operating temperatures. With the increase of operating temperature the sensing response was found to increase till 100 °C at a fixed H_2 concentration of 1000 ppm. The sensor's response and recovery was found to be reasonably good at the operating temperature of 50 °C, which prompted us to do the sensing measurement at room temperature as well as at 50 °C, and the results are displayed in **Fig A.4.B.4**.
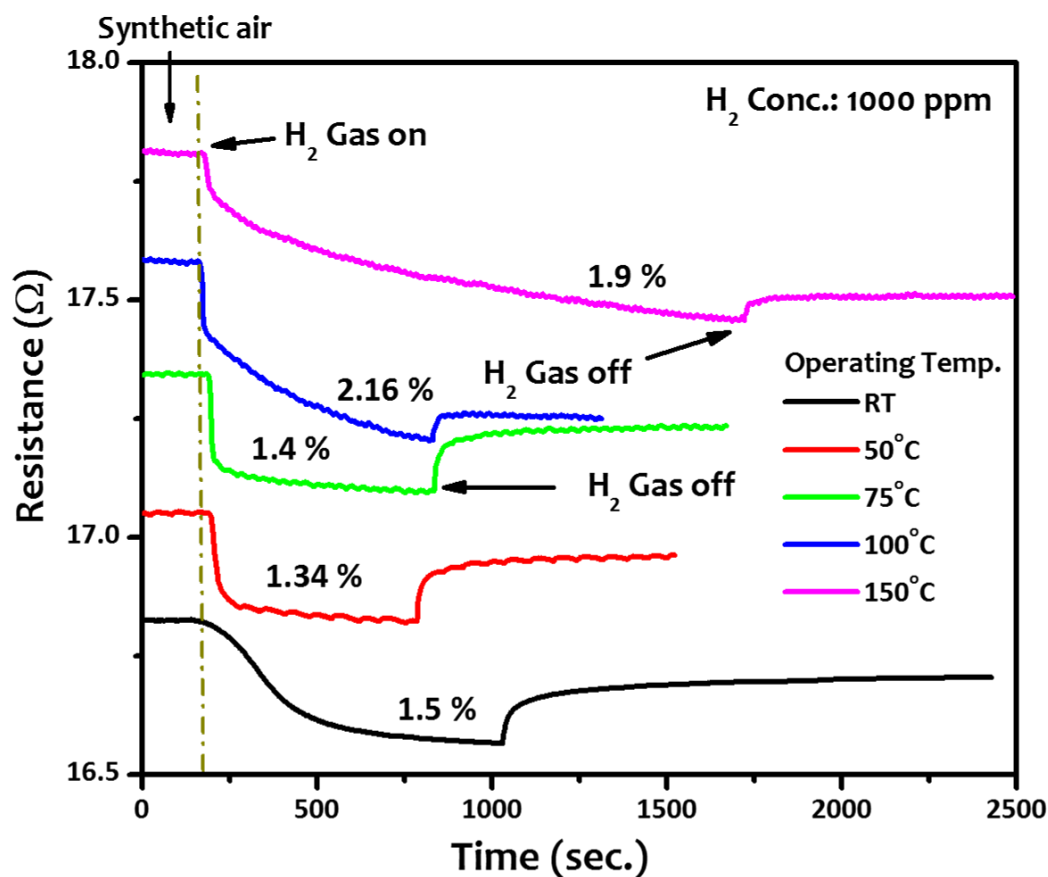
Fig A.4.B.3: *Pt/ porous GaN device Resistance Versus time at various operating temperatures with a fixed 1000 ppm H₂ gas concentration.*
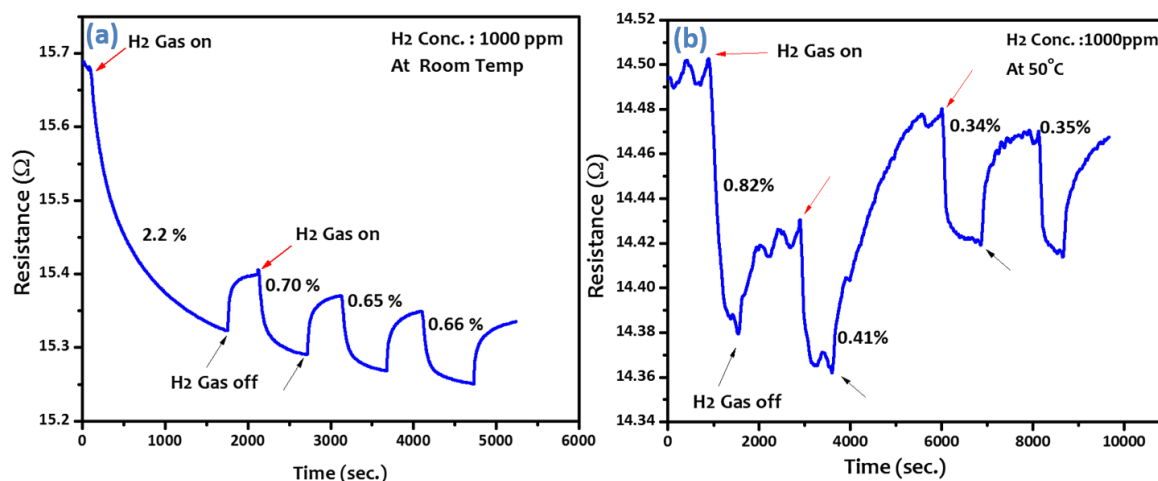
Fig A.4.B.4: *Pt/ porous GaN device Resistance Versus time at (a) Room temperature and (b) 50 °C with a fixed 1000 ppm H_2 gas concentration.*

At room temperature **Fig A.4.B.4 (a)**, initially in the first cycle, the resistance changed drastically for a fixed H_2 concentration of 1000 ppm, but the recovery of the resistance after switching off the test gas (H_2) flow was poor. However when the sensor was exposed to the same fixed H_2 concentration the response was found to be low in comparison with the first cycle. This may be due to the bad recovery of sensor's resistance after first cycle. At 50 °C operating temperature the sensor behaved randomly in response to a fixed H_2 gas concentration of 1000 ppm.

A.4.B.4: Conclusion and Future outlook

In conclusion, the response and recovery of the Pt/Porous GaN nanowall network sensor was fast at higher temperature (50 °C), but the sensitivity was low as compared to the room temperature sensing. In other words, at Room temperature the sensitivity is high as compared to sensing at 50°C, but the response and the also recovery time of the sensor was more.

We need to think of how to improve the resistance recovery in the Pt/Porous GaN H_2 Sensor device. We also need to look at effect of high carrier concentration of GaN nanostructure on its gas sensing properties.

A.4 References

1) T. Hisatomi, J. Kubota and K. Domen, Chem. Soc. Rev., 2014, **43**, 7520

2) *BP Statistical Review of World Energy June 2013*, BP Statistical Review of World Energy, BP p.l.c, 1 St James's Square, London, SW1Y 4PD, UK.

3) K. Maeda and K. Domen, J. Phys. Chem. Lett. 2010, 1, 2655–2661.

4) A. Kudo and Y. Miseki, Chem. Soc. Rev., 2009, 38, 253.

5) A. Fujishima and K. Honda, Nature, 1972, 238, 37.

6) K. Sivula, J. Phys. Chem. Lett., 2013, 4, 1624.

7) Z. Chen, T.F. Jaramillo, T.G. Deutsch, A. Kleiman-Shwarsctein, A.J. Forman, N. Gaillard, R. Garland, K. Takanabe, C. Heske, M. Sunkara, E.W. McFarland, K. Domen, E. L. Miller, J. A. Turner and H. N. Dinh, J. Mater. Res., 2010, 25, 3.

8) M. G. Walter, E. L. Warren, J. R. McKone, S. W. Boettcher, Q. Mi, E. A. Santori and N. S. Lewis, Chem. Rev., 2010, 110, 6446.

9) Luo, W. J.; Liu, B.; Li, Z. S.; Xie, Z. L.; Chen, D. J.; Zou, Z. G.; Zhang, R. Appl. Phys. Lett. 2008, 92, 262110.

10) Jung, H. S.; Hong, Y. J.; Li, Y.; Cho, J.; Kim, Y. J.; Yi, G. C. ACS Nano 2008, 2, 637.

11) Waki I, Cohen D, Lal R, Mishra U, DenBaars S and Nakamura S 2007 *Appl. Phys. Lett.* **91** 093519.

12) F. Yun, S. Chevtchenko, Y.-T. Moon, H. Morkoc, T.J. Fawcett, J.T. Wolan, GaN resistive hydrogen gas sensors, Appl. Phys. Lett. 87 (2005) 073507-1–073507-3.

13) J.-R. Huang, W.-C. Hsu, Y.-J. Chen, T.-B. Wang, K.-W. Lin, H.-I. Chen, W.-C. Liu, Comparison of hydrogen sensing characteristics for Pd/GaN and Pd/Al0.3Ga0.7As Schottky diodes, Sens. Actuators B: Chem. 117 (2006) 151–158.

14) J.-R. Huang, W.-C. Hsu, H.-I. Chen, W.-C. Liu, Comparative study of hydrogen sensing characteristics of a Pd/GaN Schottky diode in air and N2 atmospheres, Sens. Actuators B: Chem. 123 (2007) 1040–1048.

15) T.-H. Tsai, J.-R. Huang, K.-W. Lin, W.-C. Hsu, H.-I. Chen, W.-C. Liu, Improved hydrogen sensing characteristics of a Pt/SiO2/GaN Schottky diode, Sens. Actuators B: Chem. 129 (2008) 292–302.

16) T.-H. Tsai, J.-R. Huang, K.-W. Lin, C.-W. Hung, W.-C. Hsu, H.-I. Chen, W.-C. Liu,Improved hydrogen-sensing properties of a Pt/SiO2/GaN schottky diode, Electrochem. Solid-State Lett. 10 (2007) J158–J160.

17) M. Zhao, J.X. Huang, C.W. Ong, Room-temperature resistive H2 sensing response of Pd/WO3 nanocluster-based highly porous film, Nanotechnology 23 (2012) 315503.

18) H. Liu, D. Ding, C. Ning, Z. Li, Wide-range hydrogen sensing with Nb-doped TiO2 nanotubes, Nanotechnology 23 (2012) 015502.

19) Zhong A, Sasaki T, Hane K. Platinum/porous GaN nanonetwork metal-semiconductor Schottky diode for room temperature hydrogen sensor. Sens Actuators Phys 2014; 209:52-6.

20) Todd G. Deutsch, Carl A. Koval, and John A. Turner. III-V Nitride Epilayers for Photoelectrochemical Water Splitting: GaPN and GaAsPN, J. Phys. Chem. B, 2006, 110, 25297-25307.

Part-B

Growth and characterization of TiO₂ thin films on different planes of sapphire by Atomic Layer Deposition

ALD
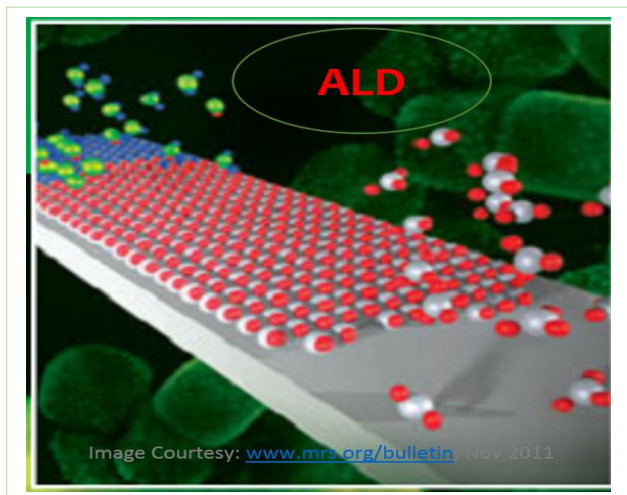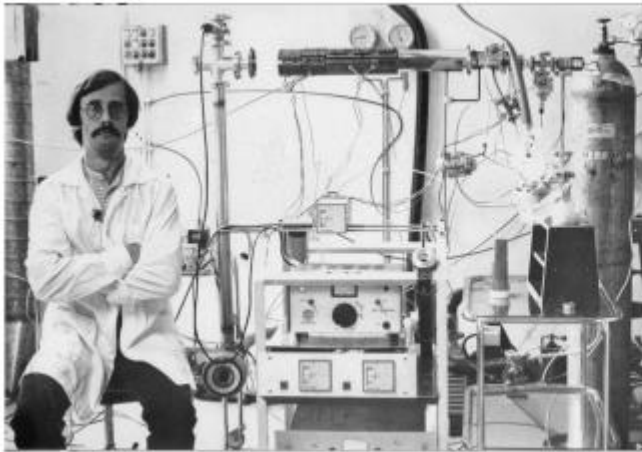
The very first experiment for a chloride process was tried by combining $ZnCl_2$ and elemental S, then by adding H_2 flow over the heated sulphur source. The experiments were not successful. The famous picture of Sven Lindfors sitting next to the glass tube ALD reactor was taken after the first successful $ZnCl_2/H_2S$ process – what is missing in the picture was Arto Pakkala and his first reaction to the success: "Siinä se on!" ("That's it!")

(Photo Courtesy: ''40 years of ALD in Finland'' by
Finnish Centre for excellence in Atomic Layer Deposition).

Chapter B.1
Introduction and Motivation

Chapter B.1
Introduction and Motivation

This chapter highlights the history, evolution, need and the basic concept underlying Atomic Layer deposition (ALD). ALD is a unique chemical process that yields ultrathin film coatings with exceptional conformality on highly non-uniform and non-planar surfaces, often with sub nanometre scale control of the coating thickness. Recently, with scaling down of semiconductor devices, need for nanotechnology has increased enormously. For nanoscale devices especially, each of the layers should be as thin and as perfect as possible. Thus, the application of atomic layer deposition (ALD) to nanofabrication strategies and emerging nano-devices has sparked a good deal of interest due to its inherent benefits compared to other thin film deposition techniques. Since the ALD process is intrinsically atomic in nature and results in the controlled deposition of films at the atomic scale, ALD produces layers with nano-meter scale thickness control and excellent conformality[1].

B.1.1 ALD history and evolution:

The concept of the Atomic Layer Deposition (ALD) process was first published by Prof. V.B. Aleskovskii in the Soviet Union in 1950s[2]. The actual invention and the first patent for ALD technology was launched by Prof. Tuomo Suntola and his co-workers in the 70s in Finland[3]. Much interest has recently developed for Atomic layer deposition (ALD) as a potential deposition method for advanced thin-film structures. The motivation for the development of ALD was the need for a deposition method for thin-film electroluminescent (TFEL) flat-panel displays. For such an application, high-quality dielectric and luminescent films are required on large-area substrates[4]. ALD is still used today in the industrial production of TFEL displays. In the mid-1980s the applicability of ALD to epitaxial compound semiconductors was demonstrated and great efforts were made in the preparation of III–V compounds in the late 1980s[5]. Due to the unfavourable chemistry between group III alkyl compounds and group V hydrides, no real benefits were achieved with ALD, compared to metal–organic vapour phase epitaxy (MOVPE) or molecular beam epitaxy (MBE). The renaissance of ALD began in the mid-1990s, with the interest focused on silicon-based

microelectronics. Shrinking device dimensions and increasing aspect ratios in integrated circuits (IC) require the introduction of new materials and thin-film deposition techniques. ALD is considered as one deposition method with the greatest potential for producing very thin, conformal films with control of the thickness and composition of the films possible at the atomic level.

B.1.2 Concept of ALD

The distinct feature of ALD which is a special modification of chemical vapour deposition (CVD) is that film growth takes place in a cyclic manner. One Atomic layer deposition cycle consists of four essential steps: 1) precursor exposure, 2) evacuation or purging of the precursors and any by-products from the chamber, 3) exposure of the reactant species, typically oxidants or reagents, and 4) evacuation or purging of the reactants and by-product molecules from the chamber (as schematically shown in **Fig. B.1**).The growth cycles are repeated as many times as required for the desired film thickness. Depending on the process and the reactor being used, one cycle can take time from 0.5 s to a few seconds, and may deposit between 0.1and 3 Å of film material. The cycle time depends particularly on the aggressiveness of the film-formation reaction. In ALD, contrast to CVD, reactions with as negative a value of ΔG as possible are desired. Although there are many similarities between ALD and chemical vapour deposition (CVD), the clear and distinctive feature of ALD lies in the self-limitation for precursor adsorption and alternate, sequential exposure of precursors and reactants. This result in the unique characteristics of ALD.

Commonly, in the growth of binary compounds such as metal oxides, a reaction cycle mainly consists of two reaction steps. In one step the metal compound precursor is allowed to react with the surface, and in the other step it reacts with the oxygen precursor. Between the steps a purge is applied to remove the excess of precursor and the reaction by-products. The self-controlled growth mode of atomic layer deposition offers several advantages. The thickness of the films can be controlled in a straightforward manner by controlling the number of reaction cycles, therefore enabling the controlled growth of ultra-thin layers. The precursors form stoichiometric films with large area uniformity and conformality even on complex surfaces with deformities.
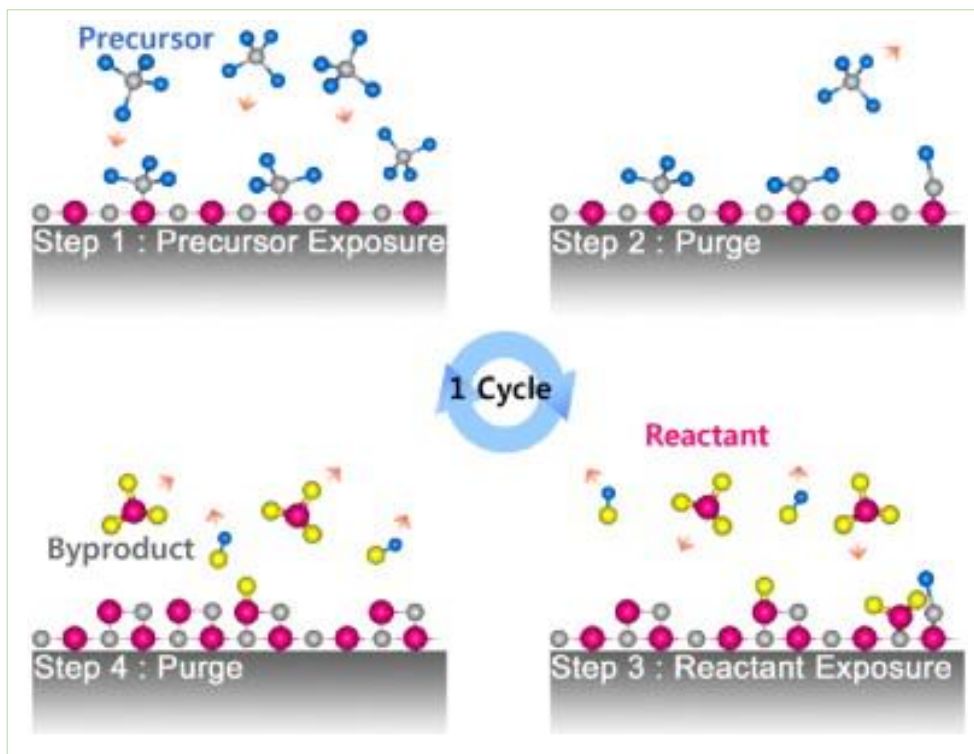
***Fig. B.1:** Schematic of one ALD cycle[1]. © Thin solid films, Elsevier 2015.*

Non-ideal ALD Behaviour and the ALD window

Atomic later deposition may not be achieved by many ALD systems, and they might not be self-limiting, because the surface species may allow additional adsorption and decompose. This decomposition may occur even at the minimum temperatures required for the surface reactions. Some other ALD systems may involve surface reaction that may never reach completion[6]. These reactions may proceed to some percentage of completion and then stop. These reactions will display self-limiting growth but with large amounts of impurities remaining in the films.

The processing temperature range for ALD[6] or the so-called "ALD window" is the region of nearly ideal ALD behaviour between the non-ideal regions as shown in **Figure B.2**. The reactants could condense on the surface or the surface reactions may not have enough thermal energy to reach completion, at lower temperatures. The surface species could decompose and allow additional reactant adsorption, at higher temperatures. This behaviour is

similar to CVD by unimolecular decomposition. The surface species needed for ALD could also desorb from the surface at higher temperatures and be unavailable for additional surface reactions. This desorption would lead to the decrease of the ALD growth per cycle at higher temperatures. This was observed in the ALD of Al_2O_3.

One system that displays dramatic nonideal ALD behaviour is TiN ALD using tetradimethylaminotitanium (TDMAT) and NH_3. Although this ALD system was initially presented as a working ALD process[7, 8], additional studies revealed that the surface reactions did not reach completion, impurities were left in the resulting films, and the films had significant porosity that led to their easy oxidation[9]. TiN ALD using TDMAT and NH_3 has no "ALD window" where the ALD process is reasonable. In contrast, TiN ALD using $TiCl_4$ and NH_3 is a well-defined ALD process that occurs at higher temperatures and produces HCl as a reaction product[10].
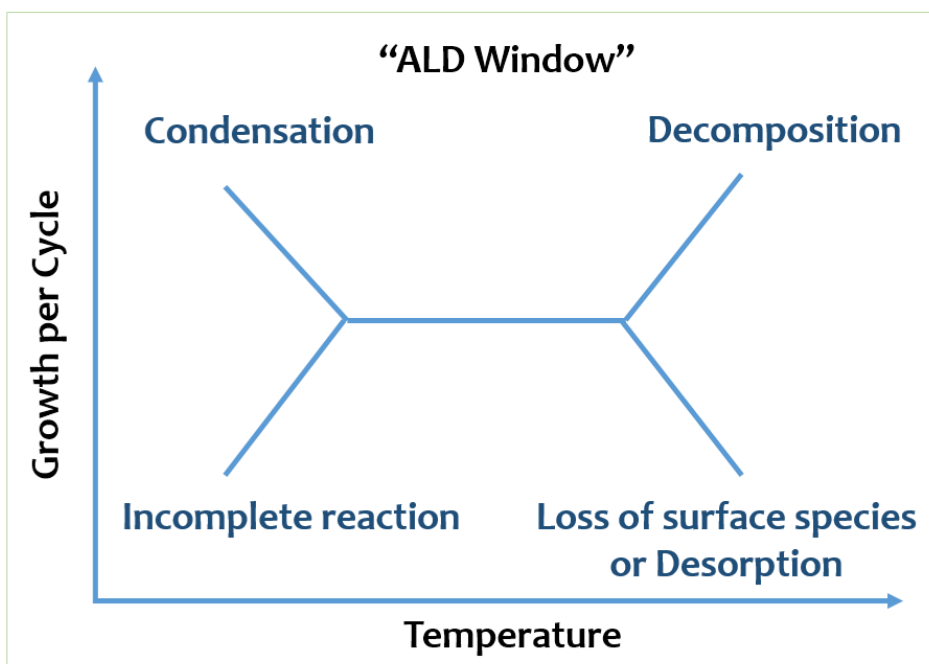
Figure B.2: *Schematic of possible behaviour for the ALD growth per cycle versus temperature showing the "ALD" window*[6].

The ALD on Biological templates, atmospheric pressure ALD, area selective ALD for spatial patterning, are emerging areas which shows that the field of ALD is growing rapidly and expanding into many applications outside of semiconductor processing[6]. The main virtues of ALD are its precise thickness control and its extreme conformality on high aspect ratio

structures. These virtues have been recognized by the above mentioned emerging application areas.

B.1.3 ALD Precursors:

ALD precursors can be gases, volatile liquids, or solids. The vapour pressure must be high enough for effective mass transportation and efficient chemical reaction; all solid, and some liquid precursors need to be heated, to attain optimum vapour pressure. Thanks to the self-limiting growth, demands for the evaporation rates to remain constant are more relaxed than in CVD, thus making it easier to use solid precursors. The challenging task of pulsing precursors evaporated at high temperatures is solved by inert-gas valving[11]. The precursors must be thermally stable at the growth temperature. Decomposition would destroy the self-limiting growth mechanism and the related advantages. In some applications, such as protective coatings, slightly thermally unstable precursors can be acceptable if their decomposition is slow (compared to the pulsing sequence times), and makes only a small contribution to the overall growth. The precursors must adsorb or react with the surface sites, such as hydroxyl groups on oxide surfaces. The type of adsorption, molecular or dissociative, and reaction mechanisms has been extensively studied[12] *in-situ* with quartz-crystal microbalance and mass spectrometric measurements. Different mechanisms have been found for different precursors. Typical metal precursors used in ALD are halides, especially chlorides, alkyl compounds, and alkoxides. Recently, Organometallic compounds, such as cyclopentadienyl complexes and alkyl and silyl amides have gained more attention[13]. The nonmetal precursors used are: water, hydrogen peroxide, and ozone for oxygen; hydrides for chalcogens; ammonia, hydrazine, and amines for nitrogen; hydrides for group V elements[12].

B.1.4 Chemical mechanism in ALD

The basic chemical mechanism active in ALD involves two vapour phase reactive chemical species, typically a metalorganic precursor and a co-reactant such as an oxygen source or a reducing agent. The precursor and co-reactant species are transported sequentially into a heated reaction zone containing a receptive growth surface, resulting in two time-separated half reaction steps. Time-separated exposure is ensured by purging the reactor with

inert gas between the reactant exposure steps. A typical ALD cycle is presented schematically in **Fig B.3.**
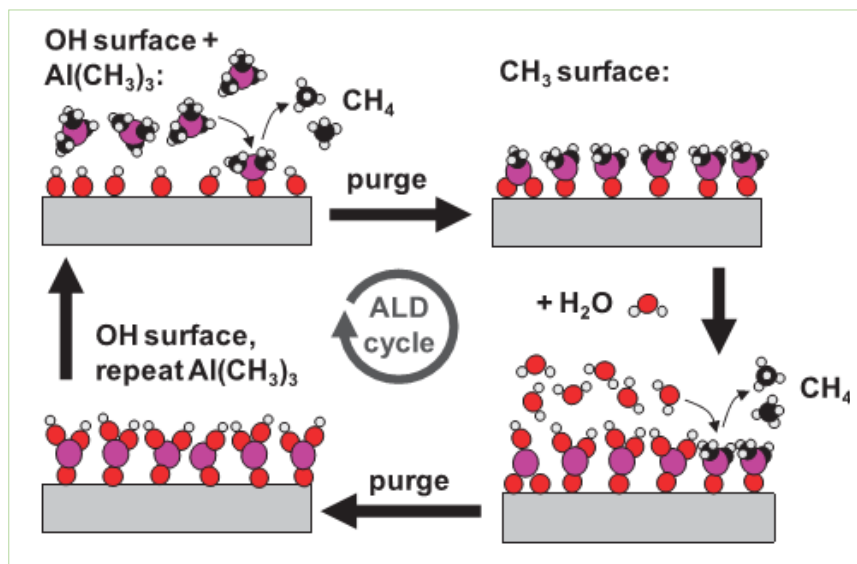
Fig B.3: *Schematic diagram of one cycle of atomic layer deposition (ALD) of aluminum oxide using sequential saturation exposures of trimethylaluminum (Al(CH₃)₃) and water, separated by inert gas purging steps[14]. © Cambridge University press.*

As shown in the top-left of the figure, the first precursor exposure step leads to the first ALD half-reaction. In this step, the precursor chemically reacts and bonds to the surface without fully decomposing. The precursor also changes the dominant surface termination, leaving the surface ready to react with the co-reactant. The remaining vapour products are pumped or pushed out of the deposition zone using inert gas flow. For the second ALD half-reaction, the co-reactant is transported to the growth surface where the co-reactant reacts on the surface. The vapour products are flushed out, and the "ALD cycle" starts over again. In common thermal ALD processes, these half-reactions are driven by a favourable change in free energy (i.e., $\Delta G < 0$), and any activation barrier is easily traversed. Generally, the reaction enthalpy change, ΔH, is also <0, although a positive entropy change could drive reactions with $\Delta H > 0$ to be thermodynamically favourable. In plasma or other "energetically enhanced" ALD processes, different reactants are used that change the overall reaction thermodynamics[14]. The plasma or other external energy source is supplied during at least one of the half-reaction steps to allow the entire reaction to proceed. The critical defining feature of a "true ALD" process is that the half-reactions are self-limiting. Once the precursor has reacted with sites prepared

during the previous co-reactant exposure, the surface reaction stops- that is, the surface sites prepared by the precursor reaction are reactive to the co-reactant, but not the precursor itself. This means that during steady state growth, the precursor will typically deposit at most only one monolayer during each half-reaction cycle, even when the surface is exposed to the reactant species for long periods of time. One must ensure that enough precursor is delivered to achieve full saturation, otherwise, growth will be non-ideal and non-uniform.

B.1.5 ALD Capabilities and Application in Microelectronics

Atomic layer deposition (ALD) not only presents a direct way to prepare nanomaterials when combined with templates, but also allows surface engineering to fine-tune the properties of the material. The main point here is not the list of materials that can be deposited by ALD but to engineer materials and structures according to the requirement. (See figure below).
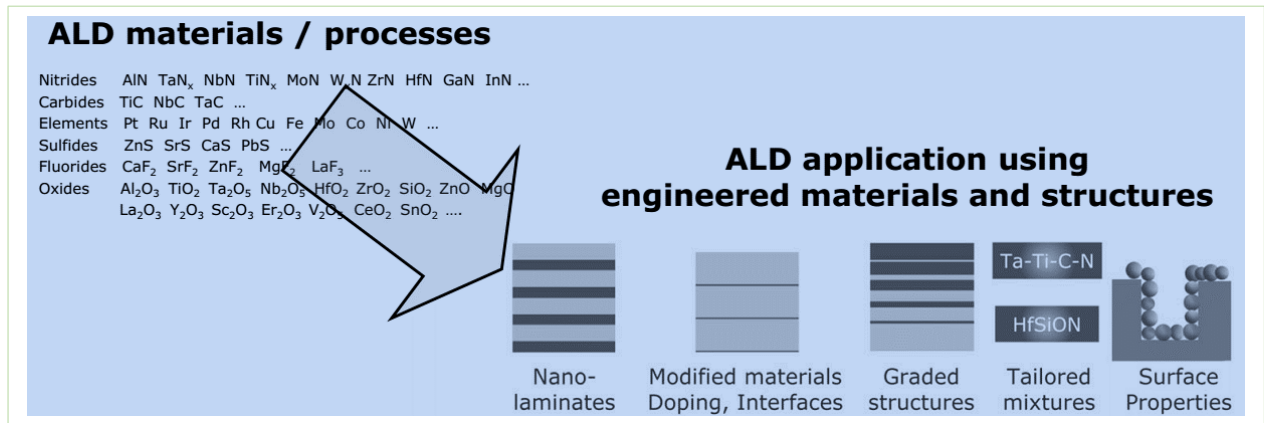

**Fig B.4:** *Schematic of ALD capabilities*[15] © Beneq 2010.

ALD features ability for sub nanometre thickness control of high quality pin-hole free films and in theory perfect conformality for the deposited film into high aspect ratio or 3D-features, which are becoming ever more significant as device dimensions shrink.

ALD is a useful process for the fabrication of microelectronics due to its ability to produce accurate thicknesses and uniform surfaces in addition to high quality film production using various different materials. In microelectronics, ALD is studied as a potential technique to deposit high-*k* (high permittivity) gate oxides, high-*k* memory capacitor dielectrics, ferroelectrics, and metals and nitrides for electrodes and interconnects. In high-*k* gate oxides, where the control of ultra-thin films is essential, ALD is only likely to come into wider use at the 45 nm technology. In metallization, conformal films are required; currently it is expected that ALD will be used in mainstream production at the 65 nm node. In dynamic random access

memories (DRAMs), the conformality requirements are even higher and ALD is the only method that can be used when feature sizes become smaller than 100 nm. Several products that use ALD include magnetic recording heads, MOSFET gate stacks, DRAM capacitors, non-volatile ferroelectric memories, and many others.

B.1.6 ALD at JNCASR

The ALD system very recently installed in our JNCASR is Beneq TFS-200 from Beneq Oy, Vantaa, Finland. The TFS 200 represents State-of-the-art design and technical solution that enables deposition of superior quality coatings on a broad array of substrate materials and sizes. It has three different modes for deposition of materials viz., thermal, remote plasma and fluidized bed reactor (FBR) together with ozone generator to use ozone as co-reactant in place of any oxygen source. The TFS 200 can coat wafers, planar objects and porous bulk materials, as well as particles (using FBR) and complex 3D objects with high aspect ratio features. Currently we have a capability of using two liquid source precursors and one hot source (can be operated at 300 °C) at a time. The deposition can be monitored *in-situ* using Quartz crystal microbalance (QCM) and residual gas analyser (RGA).
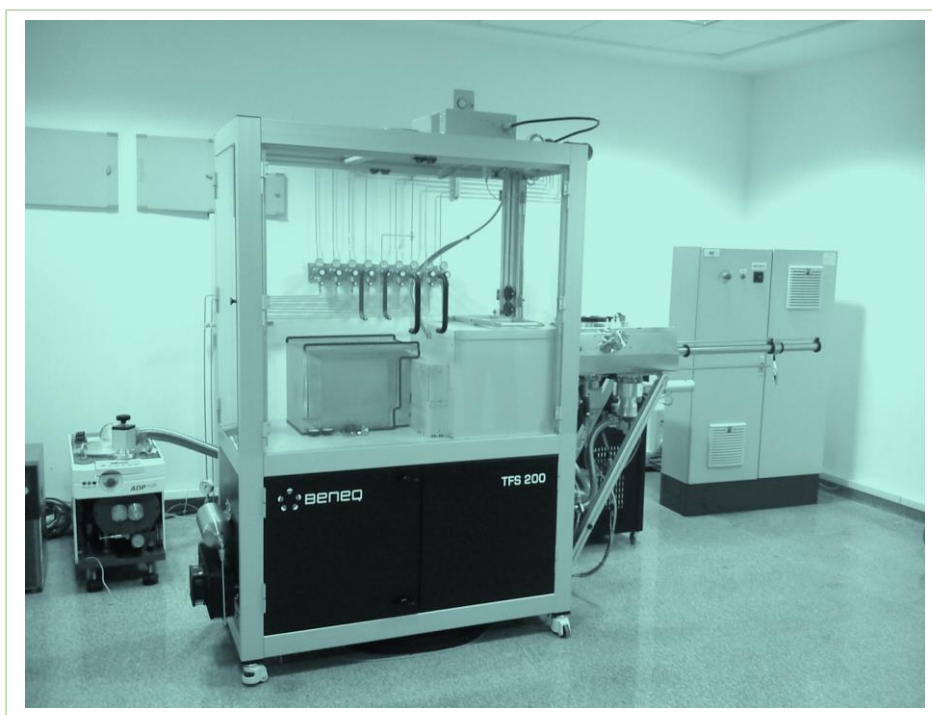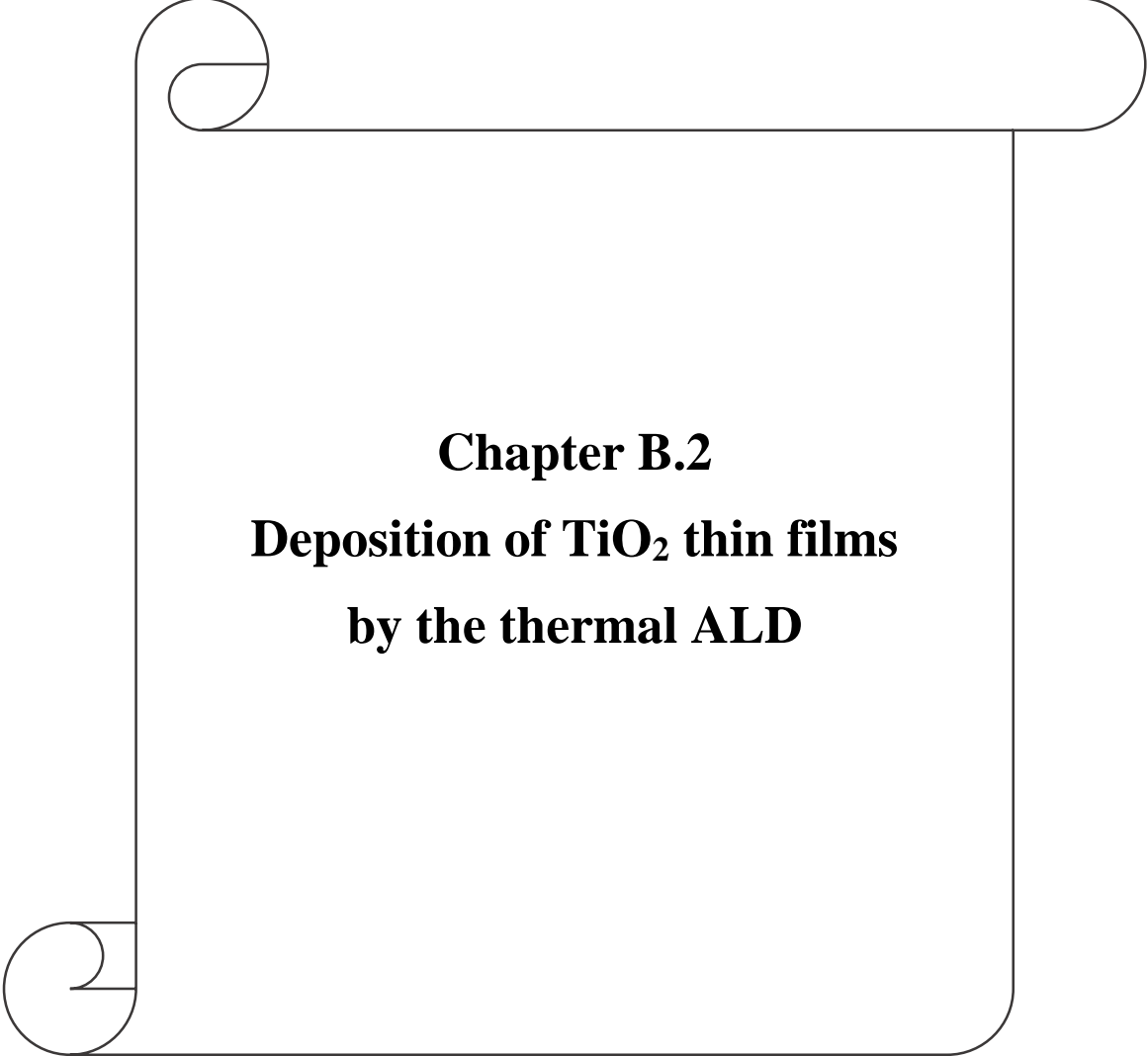

Fig B.5: *Beneq TFS-200 ALD system installed at JNCASR, Bengaluru, INDIA.*

Scope of Part B of the thesis:

This Part B of the thesis is an attempt to deposit TiO_2 films on different planes of sapphire by thermal atomic layer deposition and try to study the effect of crystallographic orientation of sapphire substrate on the deposited TiO_2 films. Most of the TiO_2 films grown by various techniques in the literature has yielded mixed rutile and anatase phases. Both of these phases have tetragonal crystal structure but show a significant difference in their optical and electrical properties. For example, the dielectric constant of rutile[15] is much higher than anatase and rutile is direct bandgap while anatase is indirect[16]. This motivated us somewhat to try and observe which phase actually dominates in our case.

B.1 References

1) Hyungjun Kim, Han-Bo-Ram Lee, W.-J. Maeng, Applications of atomic layer deposition to nanofabrication and emerging nanodevices, Thin Solid Films, 517, 8, 2009, 2563-2580.

2) V. B. Aleskovskii, J. Appl. Chem. USSR. 47 (1974) 2207.

3) T. Suntola, J. Antson, U.S. Patent 4,058,430, 1977.

4) M. Leskela, W.-M. Li, M. Ritala, Semicond. Semimetals 1999, 64, 413 – 487.

5) Atomic Layer Epitaxy (Eds.: T. Suntola, M. Simpson) Blackie, Glasgow, 1990, p. 182.

6) Atomic Layer Deposition: An Overview, Steven M George, Chem. Rev., 2010, 110, 111-131.

7) Lim, J. W.; Park, H. S.; Kang, S. W. J. Electrochem. Soc. 2001, 148, C403.

8) Min, J. S.; Son, Y. W.; Kang, W. G.; Chun, S. S.; Kang, S. W. Jpn. J. Appl. Phys. Part 1 1998, 37, 4999.

9) Elam, J. W.; Schuisky, M.; Ferguson, J. D.; George, S. M. Thin Solid Films 2003, 436, 145.

10) Ritala, M.; Leskela, M.; Rauhala, E.; Haussalo, P. J. Electrochem. Soc. 1995, 142, 2731.

11) Leskelä, M. and Ritala, M. (2003), Atomic Layer Deposition Chemistry: Recent Developments and Future Challenges. Angew. Chem. Int. Ed., 42: 5548–5554. doi: 10.1002/anie.200301652.

12) M. Ritala, M. LeskelH in Handbook of Thin Film Materials, Vol. 1 (Ed.: H. S. Nalwa), Academic Press, San Diego, 2001, pp. 103 – 156.

13) M. LeskelH, M. Ritala, J. Phys. IV 1999, 9(8), 837 – 852; M. LeskelH, M. Ritala, Thin Solid Films 2002, 409, 138 – 146.

14) Gregory N. Parsons, George Steven M., Knez Mato., MRS Bulletin 2011, 36, 865.

15) Jin Young Kim *et al* 2005 *Jpn. J. Appl. Phys.* **44** 6148 doi:10.1143/JJAP.44.6148.

16) Tang H, Prasad K, Sanjinès R, Schmid PE, Lévy F. Electrical and optical properties of TiO2 anatase thin films. J Appl Phys. 1994; 75:2042.

Chapter B.2

Deposition of TiO$_2$ thin films

by the thermal ALD

Chapter B.2

Deposition of TiO$_2$ thin films by thermal ALD

This chapter deals with the deposition of TiO$_2$ thin films by thermal ALD on different planes (c, a, m, and r) of sapphire. TiCl$_4$ and deionized (DI) water were used as source precursors. All the films were deposited simultaneously under the same growth conditions at 300 °C and were found to be 100 nm thick. Also, all the films (on c, m, a-plane sapphire) showed up pure anatase phase of TiO$_2$ analysed by X-ray diffraction, Raman, UV-Visible spectroscopy, and XPS. The TiO$_2$ film on c-plane sapphire additionally showed epitaxial orientation with (112) TiO$_2$ ∥ (0001) Al$_2$O$_3$.

B.2.1 Introduction

TiO$_2$ has become a promising material in different applications for its large band gap[1], high refractive index[2, 3], high dielectric constant, and highly active surface. In terms of photochemical properties, TiO$_2$ is used in decomposition of water into hydrogen and oxygen to serve as a photo-catalyst in solar cells. In addition, TiO$_2$, as a semiconducting metal oxide, can be used as oxygen gas sensor to control the air/fuel mixture in car engines. The high dielectric constant broadens the applications of TiO$_2$ in electronics, such as capacitor and memory device. In our daily life, titanium dioxide pigment is almost used in every kind of paint because of its high refractive index[4].

Titanium dioxide (TiO$_2$) is one of the important semiconductor materials used in a wide range of applications. It primarily crystallizes in three different phases, i.e., rutile (tetragonal), anatase (tetragonal), and brookite (orthorhombic), among which the rutile phase is the most stable one. It has a tetragonal lattice with P4$_2$/mnm space group and lattice parameters of a = b = 4.5933 and c = 2.9592 Å[5, 6]. The band gap and refractive index in bulk are about 3.0 eV and 2.9, respectively. Anatase phase is one of the 14 polymorphs of Titania (**See table B.2.1**). The polymorphs marked in the table as occurring under high pressure are pressure transforms of either rutile, anatase, and brookite or the pressure-induced phases.

The crystalline structure of TiO_2 films grown by ALD will be dependent on precursors, growth temperature, and substrates. Epitaxial growth of TiO_2 thin films on the sapphire substrate (Rhombohedral with the R-3c space group, $a = b = 4.7587$ and $c = 12.9929$ Å, $\gamma = 120°$) is important from technological point of view, since it leads to integration of functionalities with improved and novel smart device structures[1]. It is also interesting from scientific viewpoint, because a tetragonal lattice is juxtaposed with a hexagonal lattice in the anatase/sapphire heterostructures. As a consequence, the atomic arrangement across the film/substrate interface and the transition from the 3-fold hexagonal symmetry to the 2-fold tetragonal symmetry are surmised to play a critical role in controlling the properties of the TiO_2/sapphire heterostructures.

There are several methods for deposition of TiO_2 thin films. However, in applications, which require very thin films with uniform thickness on large-area substrates, atomic layer deposition (ALD) method has some clear advantages compared with other deposition techniques. An example of this kind of applications is deposition of gate dielectrics for metal-oxide-semiconductor devices. In these devices, the dielectric layers must be of very uniform thickness and it should be possible to reduce the thickness of oxide down to few nanometres[8].

System	Notation/name	Space group	Isomorph	Occurrence
Monoclinic	$TiO_2(B)$	$C2/m$ (#12)	Na_xTiO_2 bronze	
	M I/Akaogiite	$P2_1/c$ (#14)	Baddeleyite (ZrO_2)	Under high pressure
Orthorhombic	$Pca2_1$-type TiO_2	$Pca2_1$ (#29)		Under high pressure
	$CaCl_2$-typeTiO_2	$Pnnm$ (#58)	$CaCl_2$	Under high pressure
	TiO_2 II	$Pbcn$ (#60)	Scrutinyite (α-PbO_2)	
	Brookite	$Pbca$ (#61)		
	O I	$Pbca$ (#61)		Under high pressure
	O II	$Pnma$ (#62)	Cotunnite ($PbCl_2$)	Under high pressure
	$TiO_2(R)$	$Pbnm$ (#62)	Ramsdellite (MnO_2)	
	$TiO_2(H)$	$I4/m$ (#87)	Hollandite ($BaMn_8O_{16}$)	
Tetragonal	Rutile	$P4_2/mnm$ (136)		
	Anatase	$I4_1/amd$ (#141)		
Cubic	Pyrite TiO_2	$Pa\bar{3}$ (#205)	Pyrite (FeS_2)	Under high pressure
	Fluorite TiO_2	$Fm\bar{3}m$ (#225)	Fluorite (CaF_2)	Under high pressure

Table B.2.1: *TiO_2 Polymorphs reprinted from[7] with permission*
© American Vacuum Society 2013.

In the ALD process, a thin solid film is formed as a result of periodically repeated deposition cycles. Each cycle contains at least two self-limited reaction steps. In one or both of these steps, precursors are adsorbed on a surface and in the complete cycle, a new layer of the

film material is formed. As the adsorption of a properly chosen precursor usually saturates at a monolayer level, the method allows precise thickness control.

Several titanium precursors have been applied to grow TiO_2 by ALD[10-21]. Here in this work, we have deposited titanium dioxide thin films on c, a, m, and r-plane sapphire substrates to study the effect of substrate orientation on various properties of TiO_2. $TiCl_4$ and H_2O were used as liquid source precursors. The deposition was done with reactor temperature of 300 °C and ultra-high pure N_2 was used as carrier and purging gas.

B.2.2 Experimental

Materials and Deposition

The precursors for titanium dioxide deposition were titanium tetrachloride (*98.0%, s d fine-chem ltd*) and ion exchanged water.

The titanium dioxide films were deposited in a TFS-200 ALD reactor (Beneq Oy, Vantaa, Finland). Prior to the film deposition, the different planes of sapphire substrates were cleaned ultrasonically in acetone for 5 min, followed by ultrasonic cleaning in DI water for 5 min. Finally, the substrates were fully dried by nitrogen flushing and loaded into the deposition chamber immediately. Nitrogen (99.9999 %,) was used as a carrier and purging gas. The reactor and chamber were operated at 0.7 and 10 mbar pressure, respectively. The precursors $TiCl_4$ and DI H_2O were kept at 20 °C during the deposition and the deposition temperature was 300 °C. The metal halide precursor delivery, the first purge, the oxygen precursor delivery, and the second purge that enabled the reliable achievement of the ALD-type self-limited growth were set to 0.5, 2, 0.3, and 2 s, respectively (the cycle formula is lettered as x_1-x_2-x_3-x_4). 1500 ALD cycles were applied to obtain TiO_2 film of thickness ~ 100-115 nm at a rate of 0.76 Å per ALD cycle.

The morphology of the films was studied using FESEM, and AFM, structural orientation and phase by Raman spectroscopy and X-ray diffraction. The bandgap of the TiO_2 films were calculated from UV-Vis-NIR transmission measurements using Tauc theory. X-ray photoelectron spectroscopy was done to study bonding characteristics in TiO_2 films.

B.2.3 Results and discussion

Film deposition

The TiO_2 films were deposited on c, a, m, and r-plane sapphire substrates using $TiCl_4$ and DI water. The reactor temperature and the precursor temperature were maintained at 300 °C and 20 °C, respectively. ALD-type self-limited growth was achieved using the cycle formula 0.5, 2, 0.3, 2s corresponding to $TiCl_4$ pulse, purge, DI H_2O pulse, and purge, respectively. In the present growth we have applied 1500 ALD cycles. From the cross section FESEM measurements, the thickness of the films were estimated to be 115 nm with an average growth rate of 0.76 Å/cycle. Schematic below shows a flowchart illustrating the present ALD growth.
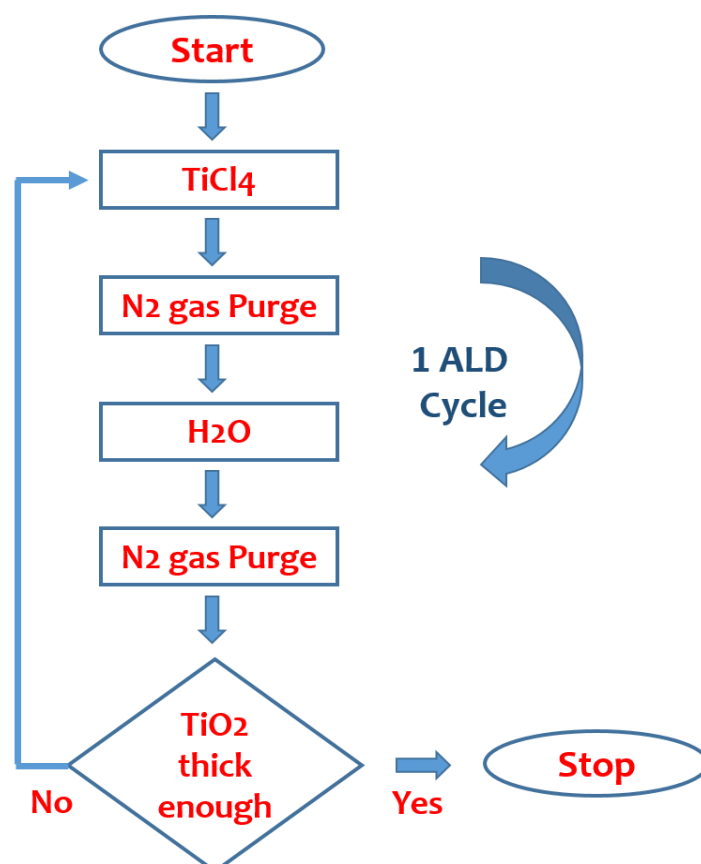
Flow chart briefly describing ALD cycles in present study.

Morphology and the structure of the films

The morphologies of the as-deposited TiO_2 on c, and a-plane sapphire imaged by FESEM, with inset showing corresponding EDS (Energy dispersive X-ray analysis) spectrum, are displayed in **Fig B.2.1**. It can be observed that the TiO_2 grains on c-plane are smaller in comparison to that on a-plane sapphire.
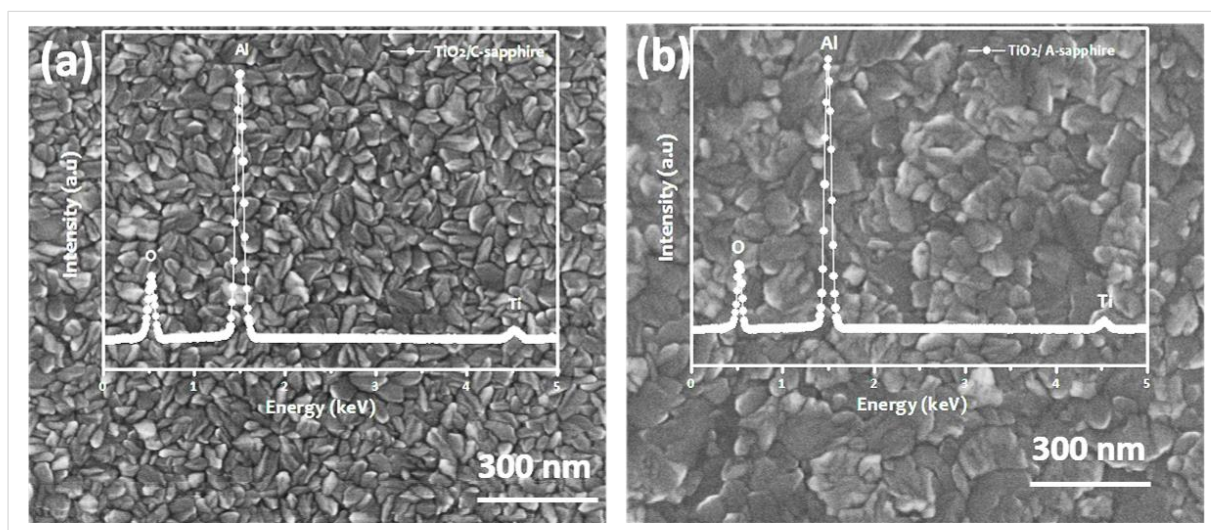
Fig B.2.1: *FESEM images of TiO_2 on (a) c-plane sapphire and (b) a-plane sapphire.*
(Inset shows corresponding EDS spectra).

Tapping-mode atomic force microscopy images were taken in order to study the morphology and roughness. The AFM images of the TiO_2 films grown on c, and a-plane sapphire are displayed in the **Figure B.2.2.** The images were processed using *Bruker, Nanoscope Analysis* Software**.** The surface roughness over an area of 0.1 μm x 0.1 μm was found to be 8 nm for TiO_2 on c-sapphire and 5 nm for r-sapphire. The atomically smooth films show the unique characteristic of ALD to provide atomic level precision and control of thickness in ultra-thin films. The grain size was smaller in case of TiO_2 on c-plane sapphire **(Fig B.2.2 (a, b))** in comparison with its grain size on a-plane sapphire **(Fig B.2.2 (c, d))**. This grain size comparison from AFM imaging was found to match with FESEM imaging shown before.
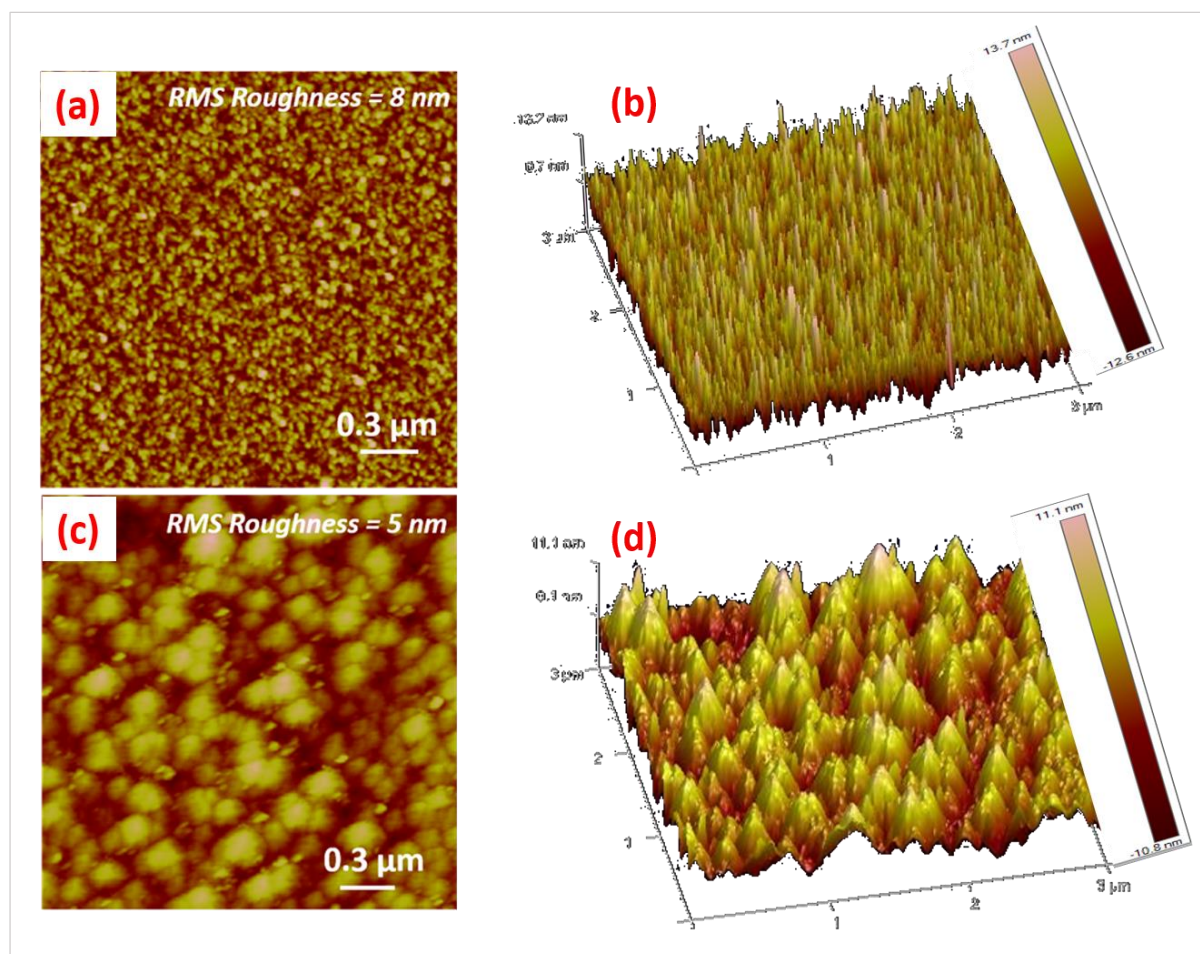
Figure B.2.2: *2D, and 3D AFM images of anatase TiO₂ on c-plane sapphire (a, b) and a-plane sapphire (c, d).*

Raman spectra in **Fig B.2.3** shows peaks corresponding to pure anatase phase of TiO_2 on all (c, a, m, and r-plane) sapphire substrates and also the inset shows that there is no peak shift of E_g peak. The Raman lines at 145, 199, 401, 520, and 640 cm^{-1} can be assigned as the E_g (high-intense), E_g (low-intense), B_{1g}, A_{1g} or B_{1g}, and B_{1g} modes of the anatase phase, respectively.

The dominant E_g mode at low frequency of 145 cm^{-1} arising from the O-Ti-O bending vibration[1] of the anatase structure is well resolved, which indicates that anatase phase was formed in the as-deposited TiO_2 films and long range order was somewhat formed. The high Raman scattering efficiency of this soft mode indicates that the polarizability varies strongly in connection with this vibration. The low growth temperature used for the deposition favoured the anatase phase in the TiO_2 which is well agreed in the literature[9].

The Raman spectrum was similar for TiO$_2$ deposited on c, a, m, and r-plane sapphire showing pure anatase phase without any shift in the observed peaks for different planes of substrates. However, a shoulder appears to the left of B$_{1g}$ peak at 401 cm^{-1}, in case of TiO$_2$ deposited on a, m, and r-plane sapphire substrates (*except on c-plane sapphire*) which is the characteristic Raman peak of a, m, and r-plane sapphire substrates. These observations were consistent with the XRD results (**see Fig B.2.4**).
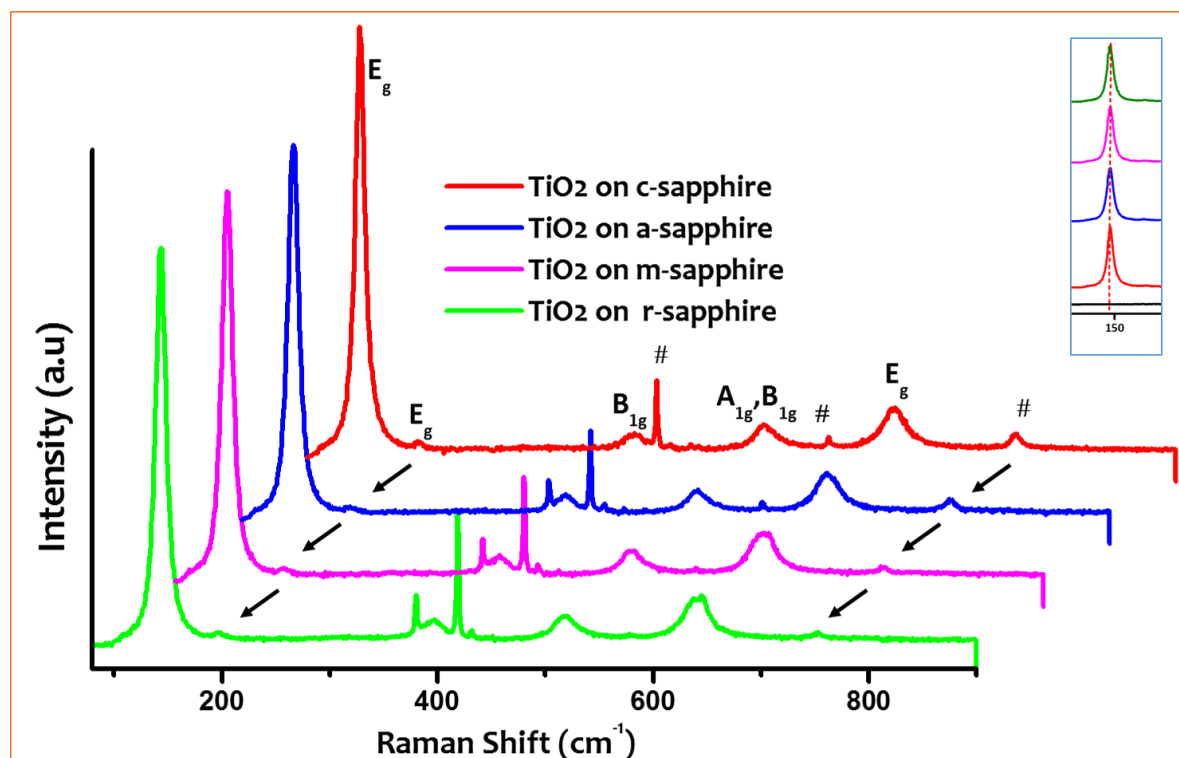
Figure B.2.3: *Raman Spectra of anatase TiO$_2$ on c, a, m, and r-plane sapphire substrates. Inset shows no shift of E$_g$ peak among the films on different substrates.* (**# indicate sapphire peaks**).

As we know, XRD usually reveals the long-range order of materials and gives average structural information within several unit cells. Raman scattering as a local probe is very sensitive to crystallinity and microstructure of materials. Raman lines become weak and broad when the samples have local lattice imperfections.

High-frequency Raman lines of the as-deposited TiO$_2$ films exhibit quite intense and no overlapped feature, which implies that these films are almost perfect and crystalline.

In order to confirm that the TiO_2 films grown have pure anatase crystalline structure, a P-XRD spectrum (see **Fig B.2.4**) of the 115-nm thick TiO_2 films was performed. The **Fig B.2.4** shows the PXRD spectrum of TiO_2 grown on c-plane sapphire, indicating pure anatase phase and it was also found that the film has an epitaxial orientation. The anatase (112) and (224) planes (at $2\theta= 38.6°$ and $82.7°$, respectively) [28] were found to be parallel to c-plane (0006) and (00012) of sapphire. We also estimated the crystallite size (*using Debye Scherer relation*) of the grains to be 18.4 nm and lattice strain to be 0.0030.


$$d = \frac{0.94\lambda}{\beta cos\theta}$$
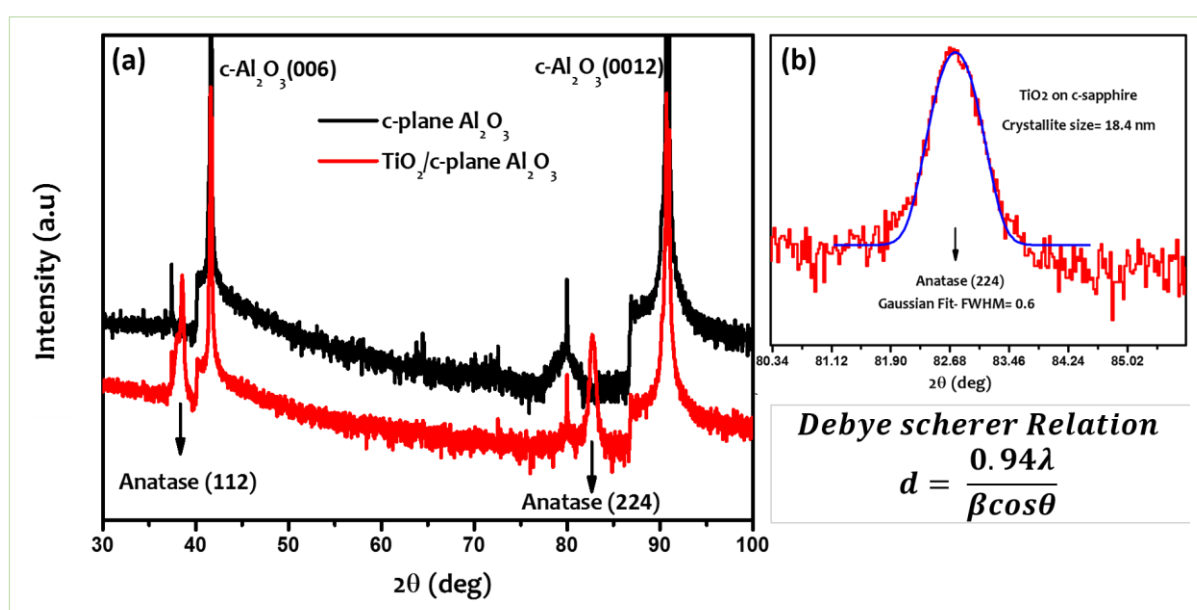
Fig B.2.4: *The PXRD pattern (a) of TiO₂ anatase phase, and (b) Gaussian fitted anatase (224) peak chosen to estimate average crystallite size.*

The **Fig B.2.5** shows the PXRD spectrum of TiO_2 grown on a, and m-plane sapphire, again indicating pure anatase phase. But in this case both the films on a, and m-plane sapphire showed Anatase (101) peak[29] (at $2\theta= 25.58°$) indicating that their crystallites are oriented along [101]. The average crystallite size, lattice strain were estimated to be 38.7 nm, 0.0042 and 38.0 nm, 0.0043 for TiO_2 anatase films on a, and m-plane sapphire, respectively.
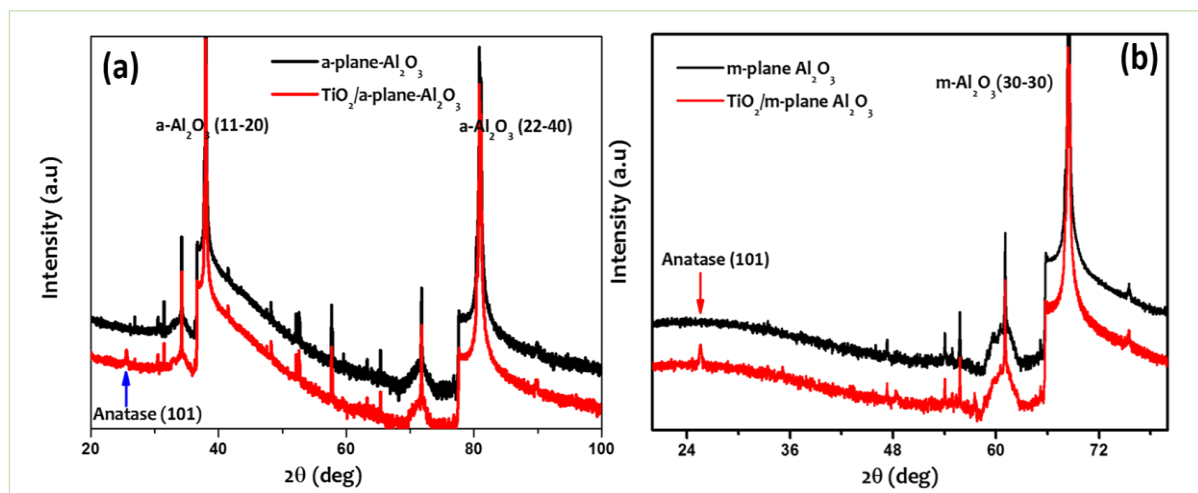
Fig B.2.5*: The PXRD pattern of TiO₂ anatase (a) a-plane sapphire and (b) m-plane sapphire. Gaussian fitted peaks for crystallite size for TiO₂ anatase on (a₁) a-plane sapphire and (b₁) m-plane sapphire. (see Figure below)*
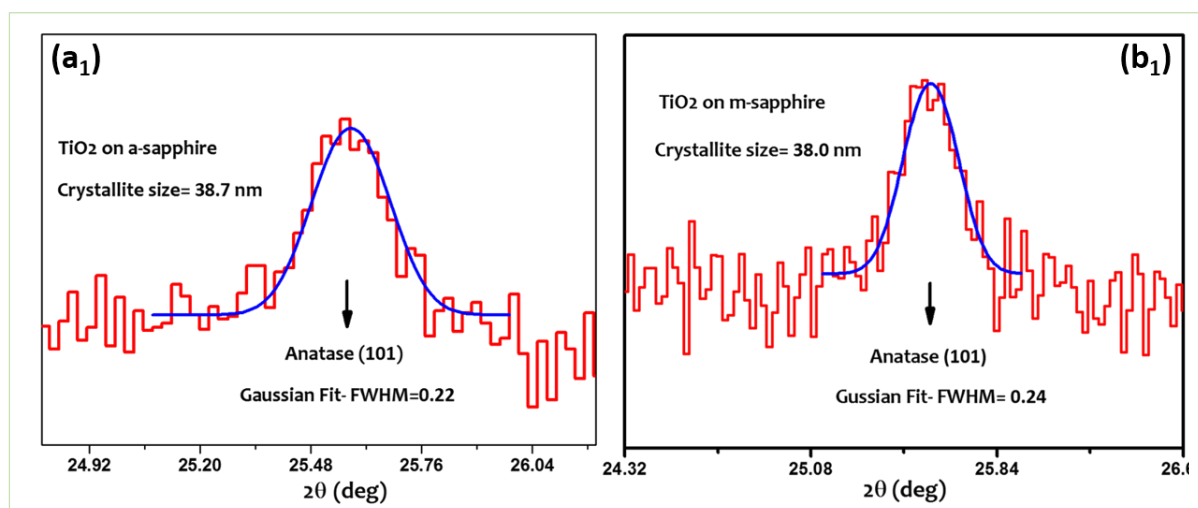

These results regarding average crystallite size matched with the trend seen with FESEM as well as AFM topography images, which showed smaller grains for TiO₂ film on c-plane sapphire compared to grains in TiO₂ film on a-plane sapphire. (FESEM and *AFM images with same scale bar were compared*).

The PXRD pattern of TiO₂ films on r-plane sapphire (**see Fig B.2.6**) did not show any peaks corresponding to anatase phase. This may be due to strong r-plane sapphire substrate (012) peak appearing at 2θ= 26°, which might have shadowed the anatase peaks (including A (101) at 2θ ~ 25.55°). We need to do HR-XRD or grazing angle XRD to visualize these anatase peaks of thin (100 nm) TiO₂ film deposited on r-plane sapphire.
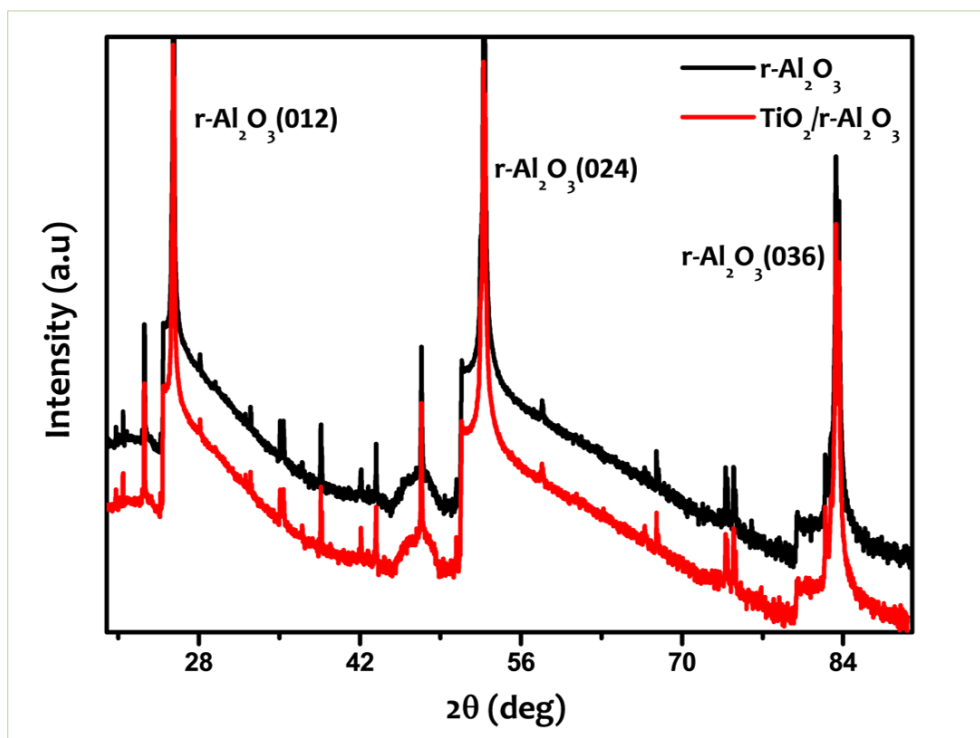
***Fig B.2.6:*** *PXRD spectrum of TiO₂ deposited on r-plane sapphire substrate.*

However, we have confirmed that the TiO_2 film was formed on r-plane sapphire using Energy Dispersive X-ray analysis measurements and FESEM. **Fig B.2.7** shows the FESEM images (with Corresponding EDS spectra as inset) of TiO_2 on r-plane and m-plane sapphire.
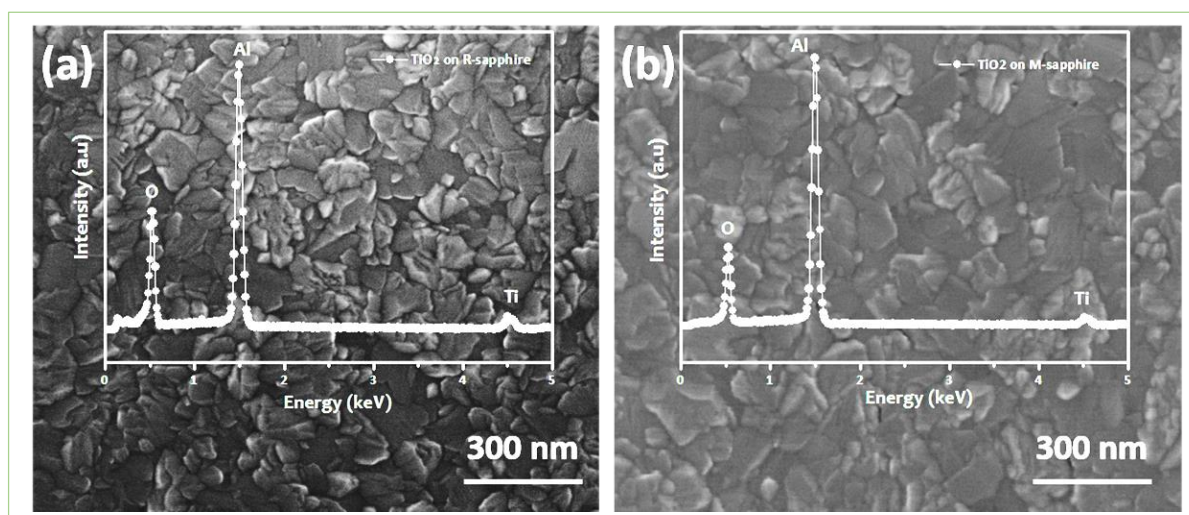
Fig B.2.7: *FESEM images of TiO₂ on (a) r-plane sapphire and (b) m-plane sapphire. (Inset shows corresponding EDS spectra).*

Optical Measurements

The UV-Vis-NIR spectra obtained in transmittance mode (using Perkin Elmer Lambda 750 spectrometer) for anatase TiO_2 on c, a, m, and r-plane sapphire is shown in the **Fig B.2.8.** The transmittances of the films (*Fig B.2.8 (a)*) were measured for a wavelength range of 200-800 nm and the band gaps were evaluated by Tauc's method. The Tauc plot for an indirect band gap was chosen since anatase is found to have indirect band gap, where the term $(\alpha h\nu)^{1/2}$ is plotted as a function of hν (*Fig B.2.8 (b)*). The optical band gap is estimated from the intersection of the linear extrapolated line with the horizontal axis. The bandgaps were estimated to be 3.22, 3.06 eV, 3.17 eV, and 3.22 eV, respectively for TiO_2 on c, a, m, and r-plane sapphire which are in good agreement with literature[22].
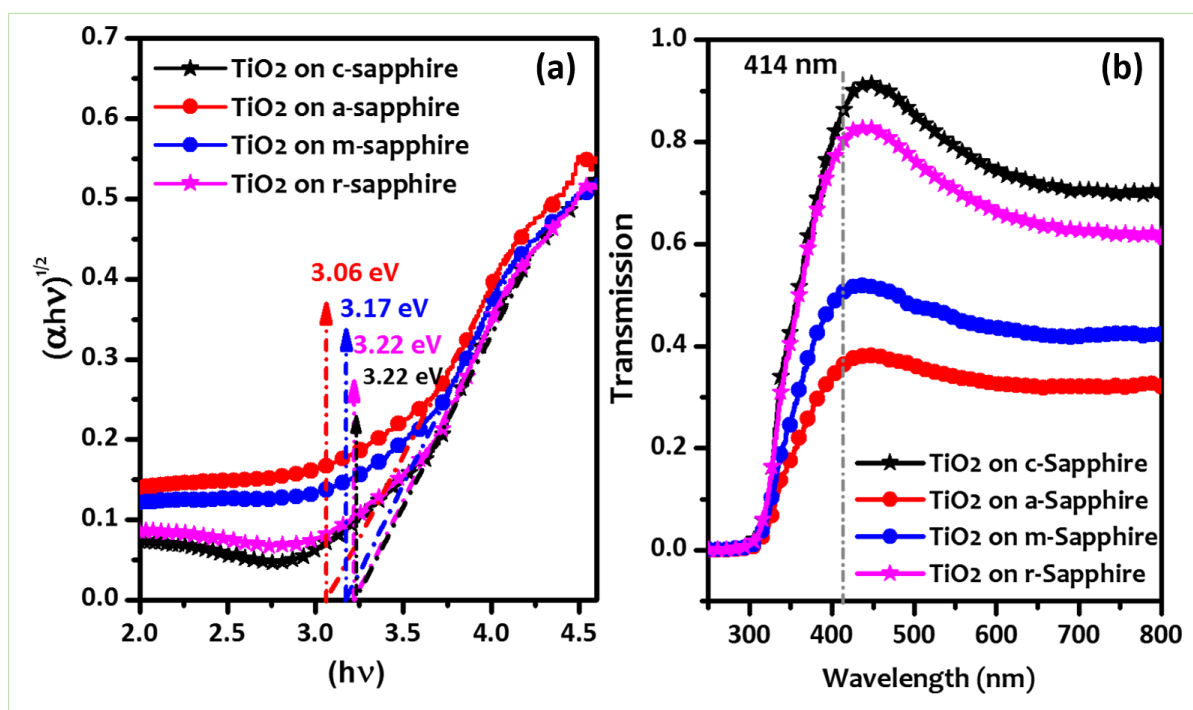

Fig B.2.8: *UV-Visible-NIR (a) Tauc plot and (b) transmission spectra of anatase TiO2 on c, a, m and r-plane sapphire.*

X-ray Photoelectron Spectroscopy Results:

The XPS spectrum for TiO_2 grown on c-plane sapphire was acquired using XPS system, Omicron, Germany. A MgKα radiation (energy of 1253.6 eV) was applied at a pressure of $1x10^{-9}$ Torr. The experimental peaks were fitted by using Fityk Software applying a Shirley background and Voigt peaks.

Fig B.2.9 shows the Ti2p and O1s core level spectra. The Ti2p core level spectrum shows the two $Ti^{4+}2p_{1/2}$ and $Ti^{4+}2p_{3/2}$ peaks at 458.0 eV, and 463.7 eV, respectively due to spin-orbit splitting. The peak separation of 5.7 eV between Ti^{4+} $2p_{3/2}$ and $Ti^{4+}2p_{1/2}$ signals is in excellent match with reported literature[26, 27]. Although the O1s core level spectra did not show a symmetric shape, the major component near a binding energy of 529.2 eV corresponds to bonding with $Ti^{25,26}$ (i.e Lattice oxygen in TiO_2). The other component near the binding energy of 531.5 eV mainly correspond to hydrated Ti-OH bond which has formed resulting from the reaction of chemisorbed water[23] with Ti^{4+} on sample surface (during H_2O pulse after $TiCl_4$). Similar results were obtained for TiO_2 deposited by ALD and various other techniques by many groups[22-26].
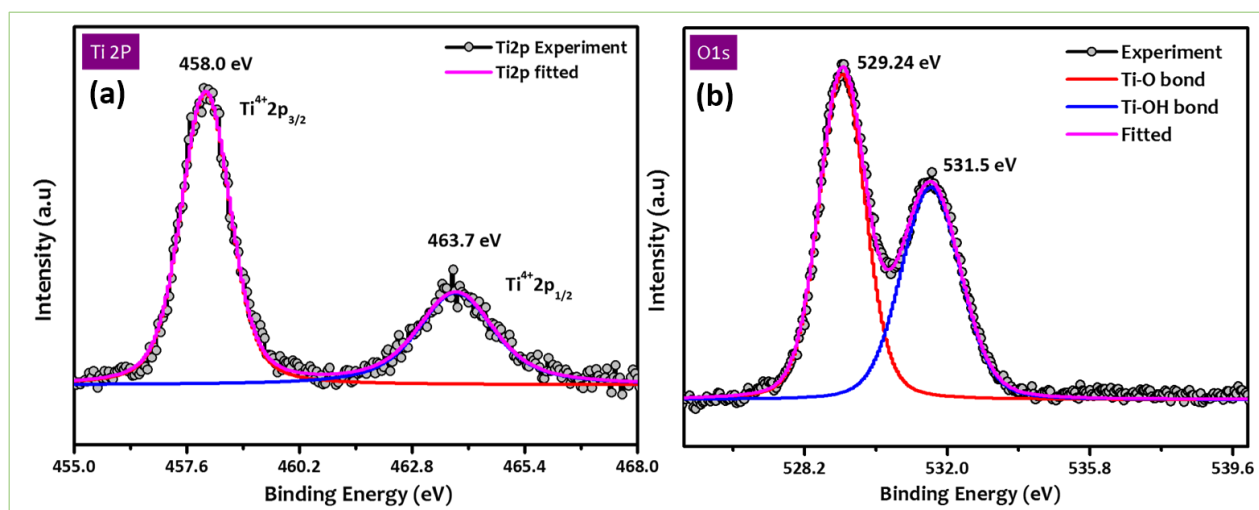
Fig B.2.9: *XPS core level spectra of (a) Ti 2p and (b) O1s of TiO2 on c-plane sapphire.*

Since we have not observed any peaks corresponding to atomic defects, like Ti^{3+}, we can conclude that our films are almost stoichiometric and defect free.

B.2.4 Summary:

In summary, TiO$_2$ thin films on c, a, m, and r-plane sapphire were deposited at 300 °C by thermal ALD. The films were characterised for structure and phase by X-ray diffraction, Raman, and morphology by FE-SEM, AFM, and optical band gap by Transmission measurements followed by bonding and stoichiometry by XPS. The film thickness was found to be around 100nm by cross sectional SEM corresponding to the average growth per cycle (GPC) of 0.76Å. All the films showed up pure tetragonal anatase crystalline phase which is not a usual observation in TiO$_2$ ALD literature[7]. The TiO$_2$ on c-plane sapphire additionally showed epitaxial orientation with (112) TiO$_2$ ‖ (0001) Al$_2$O$_3$.The indirect band gaps of the anatase TiO$_2$ films (~ 3-3.2 eV) were estimated using Tauc theory.

B.2 References

1) Tang H, Prasad K, Sanjinès R, Schmid PE, Lévy F. Electrical and optical properties of TiO_2 anatase thin films. J Appl Phys. 1994; 75:2042.

2) Chao S, Wang WH, Lee CC. Low-loss dielectric mirror with ion-beamsputtered TiO_2-SiO_2 mixed films. Appl Opt. 2001;40: 2117–82.

3) Yokogawa T, Yoshii S, Tsujimura A, Sasai Y, Merz J. Electrically pumped CdZnSe/ZnSe blue-green vertical-cavity surface-emitting lasers. J J Appl Phys, Part 2: Letters. 1995; 34: L751 –3.

4) Jin et al., .Nanoscale Research Letters (2015) 10:95.

5) J. K. Yao, H. L. Huang, J. Y. Ma, Y. X. Jin, Y. A. Zhao, J. D. Shao, H. B. He, K. Yi, Z. X. Fan, F. Zhang, and Z. Y. Wu, Surf. Eng. 25, 257 (2009).

6) A. Fujishima, X. Zhang, and D. A. Tryk, Surf. Sci. Rep. 63, 515 (2008).

7) Atomic layer deposition of epitaxial TiO_2 II on c-sapphire Tarre, Aivar and Möldre, Kristel and Niilisk, Ahti and Mändar, Hugo and Aarik, Jaan and Rosental, Arnold, Journal of Vacuum Science & Technology A, 31, 01A118 (2013), DOI:http://dx.doi.org/10.1116/1.4764892.

8) S.A. Campbell, D.C. Gilmer, X. Wang, M. Hsieh, H. Kim, W.L. Gladfelter, J. Yan, IEEE Trans. Electron. Devices 44 (1997) 104.

9) Seong Keun Kim, Gyu Weon Hwang, Wan-Don Kim, and Cheol Seong Hwang, Electrochemical and Solid-State Letters, 9 (1) F5-F7 (2006).

10) M. Ritala, M. Leskela¨, L.-S. Johansson, L. Niinisto¨, Thin Solid Films 228 (1993) 32.

11) H. Kumagai, M. Matsumoto, K. Toyoda, M. Obara, M. Suzuki, Thin Solid Films 263 (1995) 47.

12) J. Aarik, A. Aidla, H. Ma¨ndar, T. Uustare, Appl. Surf. Sci. 172 (2001) 148.

13) J. Aarik, A. Aidla, H. Ma¨ndar, V. Sammelselg, J. Cryst. Growth 220 (2000) 531.

14) M. Ritala, M. Leskela¨, L. Niinisto¨, P. Haussalo, Chem. Mater.5 (1993) 1174.

15) J. Aarik, A. Aidla, T. Uustare, M. Ritala, M. Leskela¨, Appl. Surf. Sci. 161 (2000) 385.

16) M. Ritala, M. Leskela¨, E. Rauhala, Chem. Mater. 6 (1994) 556.

17) J. Aarik, A. Aidla, V. Sammelselg, T. Uustare, M. Ritala, M. Leskela¨, Thin Solid Films 370 (2000) 163.

18) A. Rahtu, K. Kukli, M. Ritala, Chem. Mater. 13 (2001) 817.

19) K. Kukli, M. Ritala, M. Schuisky, M. Leskela¨, T. Sajavaara, J. Keinonen, T. Uustare, A. Ha˚rsta, Chem. Vapour Deposition 6 (2000) 303.

20) K. Kukli, A. Aidla, J. Aarik, M. Schuisky, A. Ha˚rsta, M. Ritala, M. Leskela¨, Langmuir 16 (2000) 8122.

21) M. Schuisky, J. Aarik, K. Kukli, A. Aidla, A. Ha˚rsta, Langmuir 17 (2001) 5508.

22) Ph.D. thesis of Marja-Leena Kääriäinen., Lappeenranta University of Technology, electronic version- ISBN 9789522654250.

23) W. Zhang, J. Yang, Y. Luo, S. Monti, V. Carravetta, J. Chem. Phys. 129 (2008) 064703.

24) M.-L. Kääriäinen, D.C. Cameron, Nitrogen doping in atomic layer deposition grown titanium dioxide films by using ammonium hydroxide, Thin Solid Films, 526, (2012), 212-217.

25) Kim, S. K., Choi, G.-J., Lee, S. Y., Seo, M., Lee, S. W., Han, J. H., Ahn, H.-S., Han, S. and Hwang, C. S. (2008), Al-Doped TiO_2 Films with Ultralow Leakage Currents for Next Generation DRAM Capacitors. Adv. Mater., 20: 1429-1435. doi:10.1002/adma.200701085.

26) S. Y. Lee et al. In-situ X-ray Photoemission Spectroscopy Study of Atomic Layer Deposition of TiO_2 on Silicon Substrate., Jpn. J. Appl. Phys. 51 (2012) 031102.

27) G. X. Liu, F. K. Shan, W. J. Lee and B. C. Shin., Journal of the Korean Physical Society, Vol. 50, No. 6, June 2007, pp. 1827-1832.

28) Tian, L.; Giusti, G.; Soum-Glaude, A.; Dan, C.Y.; Cagnon, L.; Volpi, F.; Mantoux, A.; Daniele, S.; Blanquet, E.; Bellet, D., "Characterization of nitrogen-doped TiO2 thin films for photovoltaic applications," *Photovoltaic Specialists Conference (PVSC), 2013 IEEE 39th* , vol., no., pp.2479,2482, 16-21 June 2013.

29) Geun-Hyoung Lee, Min-Sung Kim., Crystal Structure of TiO_2 Thin Films grown on Sapphire Substrates by RF Sputtering as a Function of TemperatureElectronic Materials Letters, Vol. 6, No. 2 (2010), pp. 77-80.

Copyright Clearance Center **RightsLink®**

CAMBRIDGE JOURNALS

Title:	Progress and future directions for atomic layer deposition and ALD-based chemistry
Author:	Gregory N. Parsons, Steven M. George, and Mato Knez
Publication:	MRS Bulletin
Publisher:	Cambridge University Press
Date:	Dec 31, 1969
	Copyright © Materials Research Society 2011

Order Completed

Thank you very much for your order.

This is a License Agreement between Shiva Kumar D T ("You") and Cambridge University Press ("Cambridge University Press"). The license consists of your order details, the terms and conditions provided by Cambridge University Press, and the payment terms and conditions.

Get the printable license.

License Number	3599250159154
License date	Mar 31, 2015
Licensed content publisher	Cambridge University Press
Licensed content publication	MRS Bulletin
Licensed content title	Progress and future directions for atomic layer deposition and ALD-based chemistry
Licensed content author	Gregory N. Parsons, Steven M. George, and Mato Knez
Licensed content date	Dec 31, 1969
Volume number	36
Issue number	11
Start page	865
End page	871
Type of Use	Dissertation/Thesis
Requestor type	Author
Portion	Text extract
Number of pages requested	2
Author of this Cambridge University Press article	No
Author / editor of the new work	Yes
Order reference number	None
Territory for reuse	World
Title of your thesis / dissertation	Epitaxial TiO2 thin films on diffrenet planes of sapphire by ALD
Expected completion date	Mar 2015
Estimated size(pages)	80
Billing Type	Invoice
Billing address	Shiva Kumar D T
	JNC Student Residence
	JNCASR
	Bengaluru, INDIA
	Bengaluru, India 560064
	Attn: Shiva Kumar D T
Tax (0.00%)	0.00 USD
Total	0.00 USD

Logged in as:

Shiva Kumar D T

Account #:
3000900217

LOGOUT

Order Completed

Thank you very much for your order.

This is a License Agreement between Shiva Kumar D T ("You") and Royal Society of Chemistry. The license consists of your order details, the terms and conditions provided by Royal Society of Chemistry, and the payment terms and conditions.

Get the printable license.

License Number	3594641148311
License date	Mar 23, 2015
Licensed content publisher	Royal Society of Chemistry
Licensed content publication	Chemical Society Reviews
Licensed content title	Recent advances in semiconductors for photocatalytic and photoelectrochemical water splitting
Licensed content author	Takashi Hisatomi,Jun Kubota,Kazunari Domen
Licensed content date	Jan 13, 2014
Volume number	43
Issue number	22
Type of Use	Thesis/Dissertation
Requestor type	academic/educational
Portion	figures/tables/images
Number of figures/tables /images	1
Distribution quantity	10000
Format	electronic
Will you be translating?	no
Order reference number	None
Title of the thesis/dissertation	Epitaxial TiO2 thin films on diffrenet planes of sapphire by ALD
Expected completion date	Mar 2015
Estimated size	80
Total	0.00 USD

ORDER MORE...   **CLOSE WINDOW**

Copyright Clearance Center

RightsLink®

Home | Account Info | Help | Live Chat

Title: Platinum/porous GaN nanonetwork metal-semiconductor Schottky diode for room temperature hydrogen sensor

Publication: Sensors and Actuators A: Physical

Publisher: Elsevier

Date: 1 March 2014

Copyright © 2014 Elsevier B.V. All rights reserved.

Logged in as:
Shiva Kumar D T
Account #:
3000900217

LOGOUT

Order Completed

Thank you very much for your order.

This is a License Agreement between Shiva Kumar D T ("You") and Elsevier ("Elsevier"). The license consists of your order details, the terms and conditions provided by Elsevier, and the payment terms and conditions.

Get the printable license.

License Number	3595070745082
License date	Mar 23, 2015
Licensed content publisher	Elsevier
Licensed content publication	Sensors and Actuators A: Physical
Licensed content title	Platinum/porous GaN nanonetwork metal-semiconductor Schottky diode for room temperature hydrogen sensor
Licensed content author	None
Licensed content date	1 March 2014
Licensed content volume number	209
Licensed content issue number	n/a
Number of pages	5
Type of Use	reuse in a thesis/dissertation
Portion	excerpt
Number of excerpts	2
Format	electronic
Are you the author of this Elsevier article?	No
Will you be translating?	No
Title of your thesis/dissertation	Growth and characterization of GaN nanostructures by MBE and Epitaxial TiO2 on different planes of sapphire by ALD
Expected completion date	Mar 2015
Estimated size (number of pages)	80
Elsevier VAT number	GB 494 6272 12
Permissions price	0.00 USD
VAT/Local Sales Tax	0.00 USD / 0.00 GBP
Total	0.00 USD

ORDER MORE...   CLOSE WINDOW

Title:	Atomic layer deposition of epitaxial TiO2 II on c-sapphire	Logged in as: Shiva Kumar D T
Author:	Aivar Tarre,Kristel Möldre,Ahti Niilisk, et al.	Account #: 3000900217
Publication:	Journal of Vacuum Science & Technology A	
Volume/Issue	31/1	
Publisher:	AIP Publishing LLC	
Date:	Nov 7, 2012	
Page Count:	5	

LOGOUT

Rights managed by AIP Publishing LLC.

Order Completed

Thank you very much for your order.

Click here for Payment Terms and Conditions.

Get a printable version for your records.

License Number	3595730174733
Order Date	Mar 25, 2015
Publisher	AIP Publishing LLC
Publication	Journal of Vacuum Science & Technology A
Article Title	Atomic layer deposition of epitaxial TiO2 II on c-sapphire
Author	Aivar Tarre,Kristel Möldre,Ahti Niilisk, et al.
Online Publication Date	Nov 7, 2012
Volume number	31
Issue number	1
Type of Use	Thesis/Dissertation
Requestor type	Student
Format	Print and electronic
Portion	Figure/Table
Number of figures/tables	1
Title of your thesis / dissertation	Epitaxial TiO2 thin films on diffrenet planes of sapphire by ALD
Expected completion date	Mar 2015
Estimated size (number of pages)	80
Total	0.00 USD

ORDER MORE...   CLOSE WINDOW